Bubble nucleation and dynamics: surface micro/nanobubbles and plasmonic microbubbles

Xiaolai Li

Bubble nucleation and dynamics: surface micro/nanobubbles and plasmonic microbubbles

Xiaolai Li

Thesis committee members:

Prof. dr. J.L. Herek (chairman)	Universiteit Twente
Prof. dr. rer. nat. Detlef Lohse (promotor)	Universiteit Twente
Prof. dr. ir. Harold J. W. Zandvliet (promotor)	Universiteit Twente
Prof. dr. Yuliang Wang (copromotor)	Beihang University
Prof. dr. Mireille M.A.E. Claessens	Universiteit Twente
Prof. dr. Xuehua Zhang	University of Alberta, Universiteit Twente
Prof. dr. Marjolein Dijkstra	Universiteit Utrecht
Prof. dr. Kerstin Eckert	TU Dresden
Assoc. Prof. dr. Corinna Maass	Universiteit Twente

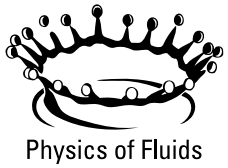

The work in this thesis was carried out at the Physics of Fluids group, Physics of Interfaces and Nanomaterials group of the Faculty of Science and Technology of the University of Twente, and School of Mechanical Engineering and Automation of Beihang University. This thesis was financially supported by the NWO, MCEC, ERC, and CSC, NSFC, and the Beijing Natural Science Foundation.

Publisher: Xiaolai Li, Physics of Fluids, University of Twente, P.O. Box 217, 7500 AE Enschede, The Netherlands

Cover design: Xiaolai Li. Oil microdroplet plume emission around a plasmonic microbubble in ternary liquids consisting of ethanol, water and trans-anethol.

ISBN: 978-90-365-5238-7
DOI: 10.3990/1.9789036552387

Bubble nucleation and dynamics: surface micro/nanobubbles and plasmonic microbubbles

DISSERTATION

to obtain
the degree of doctor at the University of Twente,
on the authority of the rector magnificus,
Prof. dr. ir. A. Veldkamp,
on account of the decision of the graduation committee,
to be publicly defended
on Thursday the 24th of September 2021 at 14:45

by

Xiaolai Li
Born on the 22nd of August 1992
in Henan, China

This dissertation has been approved by the promotors:

Prof. dr. rer. nat. Detlef Lohse

Prof. dr. ir. Harold J. W. Zandvliet

and the copromotor:

Prof. dr. Yuliang Wang

Contents

Chapter 1

Introduction

Bubbles are commonly observed in daily life, and in numerous natural and industrial processes. They exist in various media and range from meters to micro/nanometers in size (Fig. 1.1). Typical examples are soap bubbles with interesting colorful surfaces floating on air; bubble clusters in boiling water, or beverages such as sparkling wine, beer and soft drinks. In nature, examples involving bubbles are numerous and sometimes they can lead to dramatic effects. For instance, volcanic eruptions due to the sudden gas release in high temperature can result in environmental damages even casualties [1, 2]. The volcanic gases converted into sulphuric acid aerosols can affect the global atmosphere, and cause unseasonable weather including cool summers and colder-than-normal winters [2]. Apart from the occurrence of bubbles in nature, bubbles are also found in various industrial technologies, such as mineral flotation with bubbles selectively carrying particulate species [3, 4]; Delivery of drugs by targeted microbubble destruction [5]; Enhanced imaging with microbubbles acting as contrast agents [6, 7]. Conversely, bubble formation are undesirable during material processing, and bubbles have to be removed in molten steel or glass via vacuum degassing. Therefore, it is essential to understand how the bubbles form, why they possess particulate properties and how to create them in desired scale or get rid of them.

1.1 Surface nanobubbles

Interfacial bubbles are gaseous domains on a solid surface (usually hydrophobic) immersed in liquid. The existence of surface nanobubbles was predicted by Parker *et al.* in 1994 as they detected the 'long-ranged interaction' at

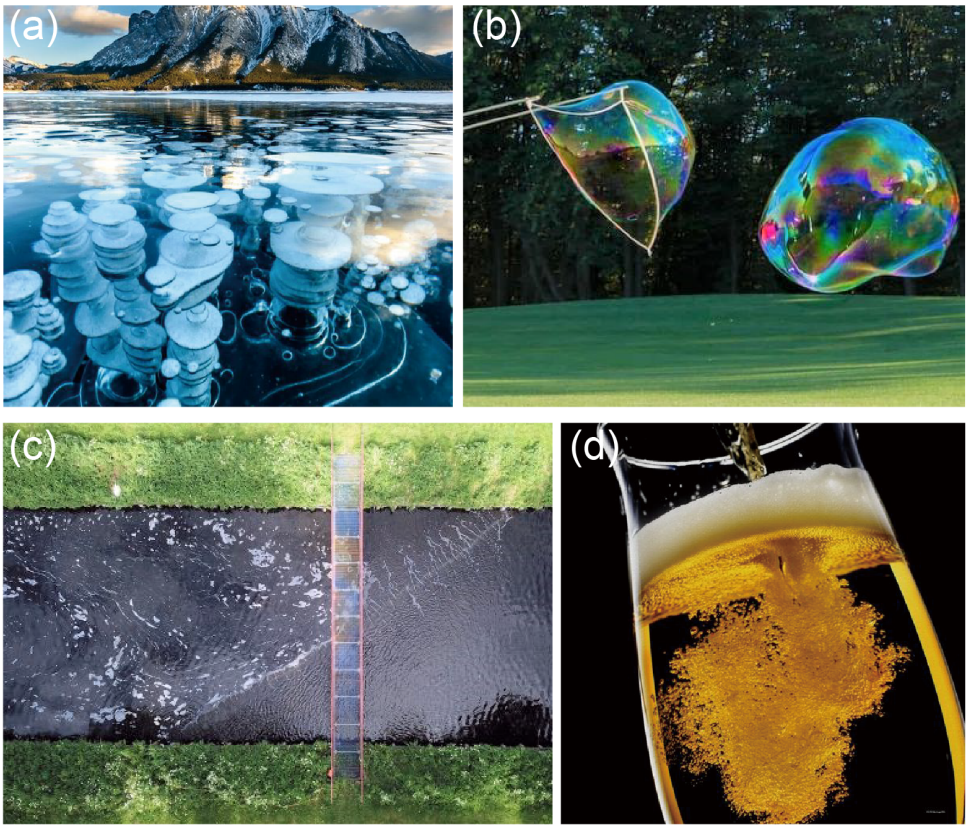

Figure 1.1: Examples of bubbles in nature and life. (a) Bubbles in an iced lake. b) Soap bubbles in air. (c) Bubble carrier for water treatment. (Dutchwatersector website) (d) Bubbles in beer. Images of a, b and d from Pinterest website.

~100 nm length scale [8]. In 2000, Lou *et al.* provided direct evidence for the existence of surface nanobubbles [9]. They reported the first atomic force microscopy (AFM) images of nanobubbles on a mica surface immersed in water. These nanobubbles have a spherical cap shape with a height of 10-100 nm and a footprint of 100-1000 nm (Fig. 1.2), and are often referred to as interfacial or surface nanobubbles (NBs).

Over the past two decades, these NBs have attracted scientific interest and

scepticism due to their special properties [10–13]. They have a contact angle of ∼5-20°, which is much smaller than their macroscopic counterparts. Moreover, the celebrated Epstein-Plesset theory predicts a lifetime of NBs in the order of microseconds [14]. However, experimental results reveal a surprising stability of these bubbles, which can survive for more than several hours and sometimes even weeks [10, 15]. A variety of questions remain to be answered regarding these bubbles: Are they really gaseous? How do they form? Why can they stably survive?

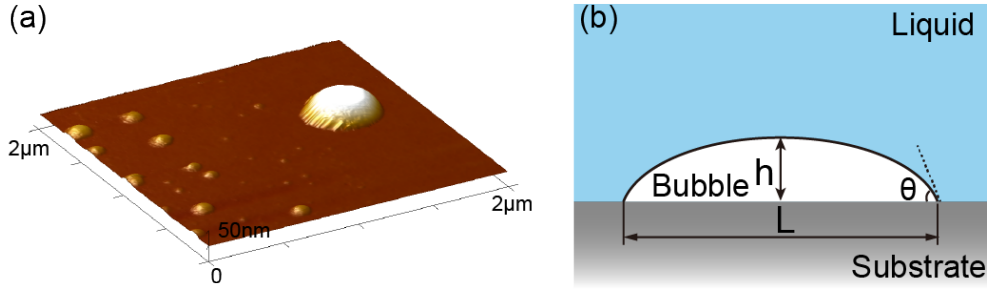

Figure 1.2: (a) Surface nanobubbles on a polystyrene substrate. (Captured in lab) (b) Schematic diagram of a surface nanobubble.

In classical nucleation theory, surface NB formation belongs to heterogeneous nucleation, which originates from the imperfections of the system. Surface defects of a wall (cracks/pits) or impurities in the liquid act as nucleation sites for the bubbles. Heterogeneous nucleation of surface NB requires very high Laplace pressures, which requires highly gas supersaturated liquids. The existence of surface NBs in ambient conditions can be rationalized by the presence of gas pockets entrapped in crevices on surfaces, referred to as Harvey nuclei. Based on the crevice model proposed by Harvey and Atchley *et al*, the trapped gas forms bubble nuclei, and these bubble nuclei can then grow by diffusion of gas from the surrounding oversaturated liquid [16].
Despite the nuclei playing a pivotal role in surface NB formation, less studies have been devoted to the origin and dynamics of nuclei. Several researchers used structured surfaces to probe the nucleation process and the stability of NBs. Using nanopatterned hydrophobic and hydrophilic surfaces, Agrawal *et al.* found that interfacial NBs only nucleate on hydrophobic domains [17]. Checco *et al.* reported the entrapment of air in 20 nm wide

nanoholes on nanopatterned surfaces using transmission small-angle X-ray scattering (SAXS) [18]. However, it remains unclear under what exact conditions air entrapment and bubble nucleation can occur. In this thesis, we will try to unravel NB nucleation mechanism by investigating the entrapment and dynamics of bubbles in micro/nanostructured surfaces.

Governing diffusion equation

In order to explain the aforementioned properties of interfacial bubbles, several theories have been used to study the diffusion problem of a gas bubble in a liquid-gas solution [14]. The most well-known model is the Epstein & Plesset model, which describes the diffusion dynamics of a spherical gas bubble in a liquid. Considering that the transport of dissolved gas between the bubble interface and liquids obeys the diffusion equation $c_t = D\nabla^2 c$, where c is the concentration field, t is time, and D is the diffusion constant, Epstein & Plesset derived the following equation,

$$\frac{dR}{dt} = -\frac{D}{\rho_g}\left(\frac{P_0}{k_H} + \frac{2\gamma}{k_H R} - c_\infty\right)\left(\frac{1}{R} + \frac{1}{\sqrt{\pi D t}}\right) \tag{1.1}$$

where ρ_g is the density of gas, γ is the surface tension, c_∞ is the gas concentration far from the bubble, and k_H is Henry's constant, *i.e.* the ratio of gas solubility c_s and ambient pressure P_0.
The Epstein-Plesset equation shows that the lifetime of nanometer-sized spherical bubbles is in the microsecond range, and spherical gas bubbles can only be diffusively stable in case $c_\infty = c_s$. This finding seems in strong disagreement with the experiments. However, Lohse and Zhang adopted the Epstein-Plesset theory to spherical-cap shaped surface nanobubbles and showed that pinning is essential ingredient to explain the long term stability of the surface nanobubbles [19]. In the quasisteady, diffusion-limited case, the gas concentration field $c(r, z)$ around the bubble satisfies

$$\partial_t c = D\nabla^2 c \approx 0, \tag{1.2}$$

where r and z are the radial and vertical coordinates, respectively. In the far field of the bubble $c(z \to \infty) = c_\infty$, while at the plane surface $z = 0$, the no flux condition $\partial c/\partial z = 0$ applies.
The calculation of the diffusive shrinkage/growth of surface bubble is analogous to Popov's seminal exact solution of the "coffee stain evaporation problem", which is also a diffusion controlled system [20]. The change in mass of

the bubble per unit time, *i.e.* dM/dt, in the case of diffusive shrinkage or growth is given by,

$$\frac{dM}{dt} = -\frac{\pi}{2} LD \left[\left(P_0 + \frac{4\sigma \sin\theta}{L} \right) \frac{c_s}{P_0} - c_\infty \right] f(\theta) \tag{1.3}$$

with

$$f(\theta) = \frac{\sin\theta}{1+\cos\theta} + 4 \int_0^\infty \frac{1+\cosh 2\theta\xi}{\sinh 2\pi\xi} \tanh[(\pi-\theta)\xi] d\xi \tag{1.4}$$

in which the ρ_g is the gas density, M is the mass, L is the footprint diameter and θ is the contact angle from gas side.
The bubble mass M is given by,

$$M = \rho_g \frac{\pi}{8} L^3 \frac{\cos^3\theta - 3\cos\theta + 2}{3\sin^3\theta} \tag{1.5}$$

Accordingly, for pinned surface nanobubbles, the ordinary differential equation for $\theta(t)$ is given by,

$$\frac{d\theta}{dt} = -\frac{4D}{L^2} \frac{c_s}{\rho_g} (1+\cos\theta)^2 f(\theta) \left[\frac{L_c}{L} \sin\theta - \zeta \right], \tag{1.6}$$

where the critical lateral extension $L_c = 4\sigma/P_0$, the oversaturation level $\zeta = 1 - c_\infty/c_s$. Using the above dynamical equations, surface nanobubbles are in stable equilibrium if,

$$\zeta = \frac{2\gamma}{LP_0} \sin\theta_e. \tag{1.7}$$

Pinning effect

It is well known that surface nanobubbles exhibit contact angles that do not agree with what one would expect on the basis of Young's relation. In addition, during bubble growth/shrinkage, the ubiquitous heterogeneities on surfaces can lead to sticking of the contact line, *i.e.* pinning and thus affect the shape of the bubbles. This results in different boundary conditions for the diffusion processes across the interface and thus to mass transfer rates for the shrinkage or growth of bubbles. Figure 1.3 shows two typical modes of bubble shrinkage, the constant-contact-angle mode (unpinned) and the constant-contact-area mode (pinned). In the constant-contact-angle mode, the bubble shrinks with a constant contact angle and decreasing footprint diameter. The Laplace pressure increases with decreasing volume of the bubble. The increase in Laplace pressure results in an increase of the dissolution rate of the bubble.

In contrast, in the case of the constant-contact-area mode, the bubble shrinks with a pinned contact line. The Laplace pressure decreases for decreasing bubble volume resulting in a decrease of the dissolution rate of the bubble.

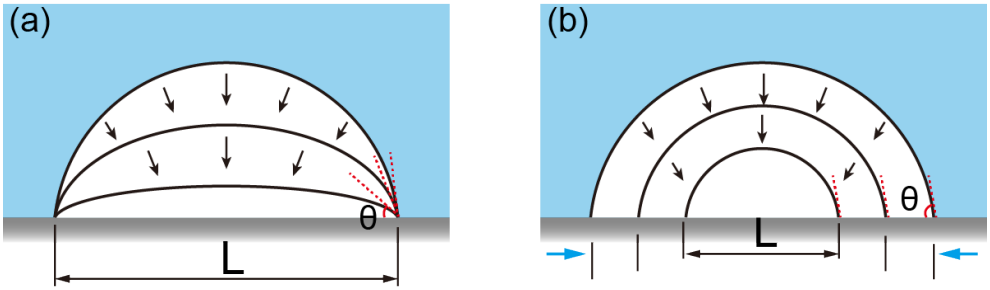

Figure 1.3: Schematic diagram of a shrinking bubble in (a) constant-contact-area mode or (b) constant-contact-angle mode.

1.2 Plasmonic microbubbles

The irradiation of a noble nanoparticle at its plasmon resonance frequency results in a very efficient heating of the nanoparticle due to the plasmonic effect. In contact with a liquid, plasmonic bubbles form due to the liquid vaporization in the vicinity of the nanoparticles [21,22]. The formation of plasmonic bubbles is a complex process and involves heat transfer, phase transitions, long-range hydrodynamic forces *etc.* [23–25]. Plasmonic bubbles are of key importance in many applications, such as biomedical diagnosis and cancer therapy [26–30], material science [31–33], and catalytic reactions [21, 34].

The dynamics of plasmonic bubbles has been extensively investigated for different arrangements of nanoparticles, laser powers, gas concentrations and many others [25, 35–39]. A previous study revealed that plasmonic microbubble nucleation and evolution in water can be divided into four phases: an initial giant vapor bubble (phase 1), oscillating bubbles (phase 2), a vaporization dominated growth phase (phase 3), and finally, a gas diffusion dominated growth phase (phase 4) [25].

In spite of the numerous studies, efforts have been mainly put on plasmonic bubble formation in pure liquids. However, in practical situations plasmonic bubbles nucleate in binary, ternary or even multicomponent liquids. This

introduces additional forces and effects, *e.g.*, Marangoni forces come into play in case of concentration gradients along bubble interfaces, which results in rich physicochemical hydrodynamics and phenomena. In a recent study the effect of the exact composition of a binary liquid on the bubble nucleation dynamics has been investigated [40]. It is found that the amount of dissolved gas in the binary liquid determines the nucleation temperature of the initial giant bubbles. The bubble volume mainly depends on the various physicochemical properties of binary liquids, such as boiling point and latent heat. However, the long-term growth dynamics of plasmonic bubbles in binary liquids and ternary liquids remain unclear.

Marangoni flow

Surface tension plays an important role at the micro/nanoscale. A gradient of surface tension can cause mass transfer along an interface, *i.e.* the so-called Marangoni effect. In the plasmonic bubble system depicted in Fig. 1.4, there exists a temperature gradient in the bubble surrounding liquid due to the heating of metal particles. As the surface tension of the liquid decreases with increasing temperature, a thermal Marangoni flow will develop toward the low-temperature side. For plasmonic bubble formation in multiple component liquids, selective vaporization occurs in the vicinity of the three phase contact line due to different liquid boiling temperatures, resulting in a tangential concentration gradient along the surface. The surface tension gradient due to concentration difference induces a solutal Marangoni flow along the surface.

A guide through the thesis

In this thesis, we investigate the entrapment of interfacial nano/microbubbles on structured surfaces, and the effect of gas and multiple liquid components on plasmonic bubble dynamics. The thesis is organized as follows:
In Chapter 2, we studied the entrapment of nanobubbles at the solid-liquid interface on nanostructured hydrophobic surfaces. We find entrapped protruding nanobubbles at small nanopits, planner nanobubbles at medium nanopits and no gas entrapment on large nanopits. The morphology and density of the trapped surface nanobubbles depends on the type of nanostructures.
In Chapter 3, we investigated the evolution of entrapped microbubbles on a hydrophobic structured surface with microwells. We find that the microbubbles form on the microwells and then dissolve in the constant contact angle

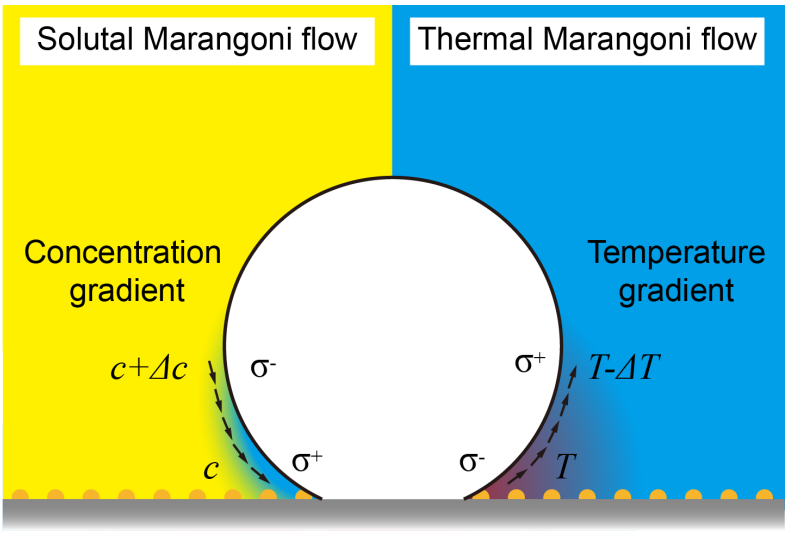

Figure 1.4: Schematic diagram of solutal Marangoni flow (a) and thermal Marangoni flow.

mode. We also quantify how a high gas undersaturation enhances the dissolution process by varying the gas undersaturation level.
In Chapter 4, we studied the effect of gas saturation on plasmonic microbubble nucleation and growth dynamics. We find that the bubble nucleation temperature depends on the gas concentration and the long-term bubble growth is governed by gas diffusion.
In Chapter 5, we studied the plasmonic microbubble formation in binary water/ethanol solutions. We find that plasmonic bubbles exhibit ethanol concentration-dependent behavior. We reveal the mechanism of the formation of the unstable bubbles in binary liquids at low ethanol concentration, and the sudden bubble shrinkage during stable bubble growth in liquids with high ethanol ratios.
In Chapter 6, we investigated plasmonic bubble nucleation in ternary liquids consisting of ethanol, water, and trans-anethole oil. We find that oil (trans-anethole) droplet plumes are produced around the growing plasmonic bubbles. The nucleation and self-organization of droplet plumes depends on the ethanol-water relative weight ratio and hence Ma.
Finally, we conclude and summarize the work presented in this thesis.

Chapter 2

Entrapment of interfacial nanobubbles on nano-structured surfaces[1]

Spherical-cap-shaped interfacial nanobubbles (NBs) forming on hydrophobic surfaces in aqueous solutions have extensively been studied both from a fundamental point of view and due to their relevance for various practical applications. In this study, the nucleation mechanism of spontaneously generated NBs at solid-liquid interfaces of immersed nanostructured hydrophobic surfaces is studied. Depending on the size and density of the surface nanostructures, NBs with different size and density were reproducibly and deterministically obtained. A two-step process can explain the NB nucleation, based on the crevice model, *i.e.*, entrapped air pockets in surface cavities which grow by diffusion. The results show direct evidence for the spontaneous formation of NBs on a surface at its immersion. Next, the influence of size and shape of the nanostructures on the nucleated NBs are revealed. In particular, on non-circular nanopits we obtain NBs with a non-circular footprint, demonstrating the strong pinning forces at the three-phase contact line.

[1]Published as: Yuliang Wang, **Xiaolai Li**, Shuai Ren, Hadush Tedros Alem, and Detlef Lohse, *Entrapment of interfacial nanobubbles on nano-structured surfaces*, Soft Matter. **13**, 5381-5388 (2017). Experiments are done by Li, analysis and writing are done by Li, Wang, and Lohse, supervision by Wang, and Lohse. Proofread by everyone.

2.1 Introduction

When hydrophobic surfaces are immersed into aqueous solutions, spherical-cap-shaped interfacial bubbles can be obtained on these surfaces [10]. These gas nanobubbles, having heights between 5 and 100 nm and diameters between 50 nm and 800 nm, are normally referred to as surface or interfacial nanobubbles (NBs). They have great potential in numerous applications, such as drug delivery and ultrasonic tumor imaging enhancement [41], mineral flotation and separation [4, 42], or nanostructured surface fabrication [43–45]. Though it remains a challenge to distinguish them from nanodroplets and blisters [10, 46], it meanwhile has been proven that they can last for hours and even days [10, 47–49]. This stability is explained by pinning of the contact line which allows for a stable balance between gas oversaturation in the liquid and the Laplace pressure in the NB [10, 19, 49–51]. The stable equilibrium is achieved by gas diffusion through the interface.

By definition, the formation of interfacial NBs is heterogenous nucleation. Its mechanism has been conjectured by Harvey *et al.* [16] and quantified by Atchley *et al* [52]. Basically, it is the entrapment of gas in crevices on surfaces. These bubble nuclei then can grow by diffusion or in case of strongly reduced pressure by gas expansion. Experimentally, for macro-sized bubbles, several experimental techniques have been applied to quantitatively validate this bubble nucleation model, such as a Berthelot tube, centrifugation, shock wave, acoustics, *etc* [53–56]. These techniques mostly focus on the reduction of liquid pressure to a negative value to find the cavitation pressure threshold. However, less studies have been performed on the nature of the crevice which is necessary to lead to NB nucleation, though on the microscale some studies were recently performed [57–59].

On a nanoscale, Checco *et al.* investigated the entrapment of air in 20 nm wide nanoholes on nanopatterned surfaces, employing the transmission small-angle X-ray scattering (SAXS) method [18]. By comparing the scattered X-ray peak intensities from the sample surfaces in contact with air and water, they conjectured that the water only partially enters the nanoholes for about 5-10 nm, with the rest of volume occupied by air, independent of the nanohole depth. However, the authors could not visualize the air entrapment with the SAXS. Therefore, it is not clear how exactly the water-air interface looks like. Moreover, it still remains unclear under what exact conditions air entrapment can happen.

Generally speaking, there are two approaches to make interfacial NBs [10],

namely the solvent exchange method [9] and the spontaneous formation of NBs at immersion of dry samples [60]. Until now, it is still challenging to form NB in a reproducible and controllable way [10]. Among the different factors that influence NB formation [47, 61–63], surface structures must play an important role, due to their role in pinning. With nanopatterned hydrophobic/hydrophilic surfaces, Agrawal *et al.* [17] and Bao *et al.* [64] found that NBs only nucleate on hydrophobic domains. Recently, a similar study was conducted by Wang *et al.* on surfaces covered with nanopores [65]. Also they found that NBs will nucleate on hydrophobic areas. Although numerous efforts have been put on the topic [10], until now there is no method which can achieve fully reproducible and controllable NB formation.

In this study, we are trying to get closer to this goal of reproducible and controllable NB formation on solid-liquid interfaces by studying how NBs form on immersed nanostructured surfaces. The NB nucleation on hydrophobic surfaces with different nanostructures will be investigated. Experimental evidence of spontaneous entrapment of gas in surface nanostructures will be provided. Moreover, the study will reveal the crucial role of pinning and implies that the size, density, and even the morphology of NBs can be controlled through surface nanostructures.

2.2 Methods and Materials

Sample preparation

The polystyrene (PS) surfaces used for nanobubble (NB) nucleation were prepared by spin coating thin films of PS on silicon (100) substrates. Before spin coating, the substrates were sequentially cleaned in sonication bathes of piranha, acetone, and then water. PS particles (molecular weight 350 000, Sigma-Aldrich) were dissolved in toluene (Mallinckrodt Chemical) to make the PS solutions. Three PS surfaces (sample 1, sample 2, and sample 3) were prepared to obtain nanopits with different sizes and shapes. The PS concentrations for the three samples were 0.05%, 0.1%, and 0.05% (all weight), respectively. The selected speeds of spin coating for the three samples were 200 rpm,1000 rpm, and 500 rpm, respectively. Two types of nanostructures, namely nanopits and nanopores, were fabricated on the three samples to study NB nucleation. First, on nanopits: For spin coated PS films, the decreasing thickness will cause inhomogeneous coating of the films [66, 67]. By delicately controlling the PS solution concentration and spin speed during spin coat-

ing, nanopits of different sizes were spontaneously obtained on sample 1 and sample 2.
On sample 3, nanopores were fabricated with assistance of NBs, as first reported in our previous study [43] and later by Janda *et al* [68]. When PS films were immersed in water, small bubbles disappear with time and generate nanopores on sample surfaces [43]. Similar results were also reported on graphene surfaces [69]. Recently, by applying negative pressure, Janda *et al.* obtained nano pinholes and nano protrusions, respectively, on thinner and thicker PS films, respectively. The NB caused generation of nanostructures on PS surfaces is mostly due to the presence of surface forces at the three phase contact line and the high inner pressure of NBs [70].
Through experiments, we found that the type of NB assisted nanostructures is strongly related to two factors, namely the NB size and the thickness of the PS films. Nanostructures tend to form namely on ultrathin PS films (with thickness from 3 nm to 7 nm). This is mostly because the polymer chain entanglement density is greatly reduced with decreasing sample thickness, as motivated theoretically [71, 72] and shown experimentally [73, 74]. This will lead to a much lower elastic modulus and fracture strength of ultrathin PS films as compared to their bulk values. During our experiments, smaller NBs (less than 50 nm in diameter and thus with much higher inner pressure, assuming constant contact angle) mostly disappear and lead to formation of nanopores on ultrathin PS film with thickness around 3 nm. Bigger NBs (larger than 80 nm) last longer and will lead to the formation of nanoindents, even on a relative thick PS film.
Sample 3 was first immersed into DI water and smaller NBs (with width less than 50 nm) were formed on the surface. After that, NBs disappeared and a porous PS surface was obtained. Water was then removed from the sample and the sample was kept in an oven for 4 h at a temperature around 50 °C to remove the remaining water. The experiment in fluid was performed to study NB nucleation.

AFM Measurement

A commercial AFM (Resolve, Bruker) operating in tapping mode was used for imaging the sample in both air and deionized (DI) water. A silicon cantilever (NSC36/ALBS, MikroMasch) with a quoted tip radius of 8 nm and stiffness of 0.6 N/m from the manufacturer was used for the scanning in air and DI water. The measured resonance frequencies of the cantilever in air and water were about 55 kHz and 16 kHz, respectively. While imaging in air and liquid,

the drive frequencies were slightly lower than that of the selected resonance. A scan rate of 2 Hz with a 0° scan angle was used. All experiments were performed at an ambient environment (temperature: 26 ± 1 °C).
In all three experiments, the sample surfaces were first scanned in air by tapping mode AFM (TMAFM). Then they were immersed into DI water to perform liquid imaging. The image scanning began immediately within 10 minutes after immersing the surface into water. For sample 1, the scanning persisting for more than 5 hours. For sample 2, the scanning last for more than 10 hours. The free oscillation amplitude of the cantilever at working frequency was about 290 mV. The larger setpoint oscillation amplitude of about 280 mV (namely 96.5% of free amplitude) was applied for liquid imaging to minimize disturbance of AFM tips to NBs.

2.3 Results and Discussion

2.3.1 Results and Discussion

The spontaneous nucleation of NBs was first studied on nanopits fabricated on spin coated polystyrene (PS) films on silicon substrates (sample 1 and sample 2). On sample 1, the width of the nanopits was in between 50-100 nm. On sample 2, their width varied from about 50 nm to 250 nm. The effect of the nanopit size on the NB entrapment was then investigated on the two samples. The tapping mode AFM (TMAFM) image of sample 1 in air is shown in Fig. 2.1a. On the surface, nanopits with typical diameter of 80 nm and depth of 4 nm are visible. The probability density function (PDF) of the nanopits' depth and width is discussed in the Appendix (see Fig. 2.8). After the sample was immersed into DI water, NBs were generated by spontaneous air entrapment in the nanopits (Fig. 2.1b). The nanopits were covered by NBs, such as at the location selected by the blue dashed box. After that, NB coalescence [75–77] was performed by applying a higher scan load (TMAFM setpoint: 80% of free oscillation amplitude) in the area in DI water. Smaller NBs were moved and coalesced to generate a bigger one, as shown in Fig. 2.1c. Therefore the nanopits become visible again after the coalescence process.
The coalescence of NBs makes it possible to compare the sample surface in air and in DI water with and without NBs. Figure 2.1d shows the 3D mesh plots of the same selected area in air (left), in water with an entrapped NB (middle), and in water after coalescence (right). From the figures, it is obviously that there was a NB entrapped in the nanopit.

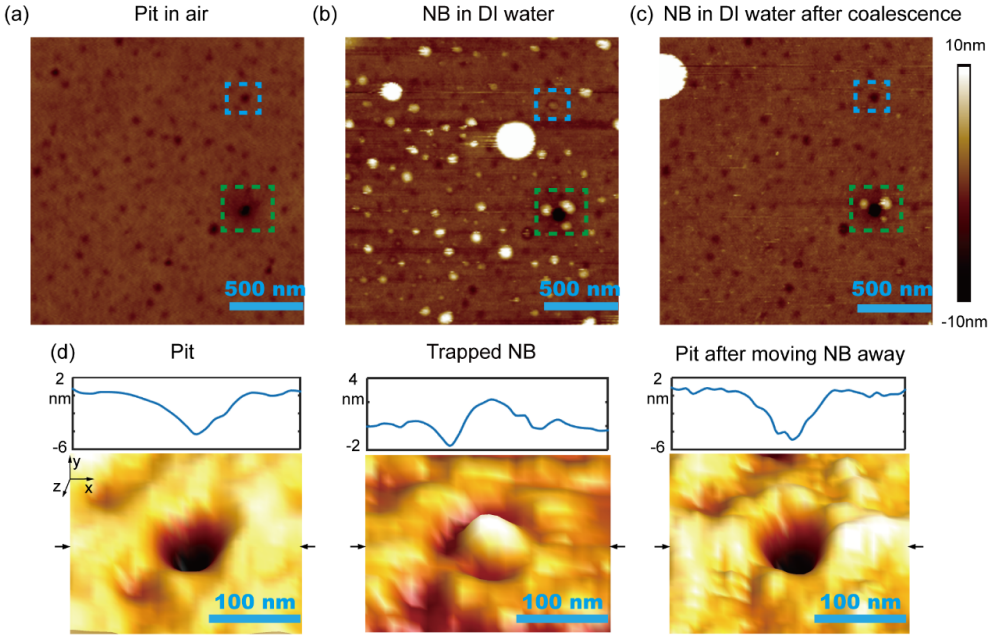

Figure 2.1: Nanobubble nucleation on smaller nanopits. (a) AFM images of nanopits on a PS surface in air. On the surface, nanopits with diameter in between 50-100 nm are visible. (b) AFM image of the same area obtained in DI water. Nanopits can entrap NBs. (c) AFM image of the same area after NB coalescence was performed. Small NBs were coalesced to generate a bigger one (see in upper left corner of image) and the nanopits now filled with water become visible again in DI water. (d) Comparison of 3D mesh plots of the areas with a blue square selected in (a-c). One can clearly see the topography of the nanopit in air (left), an entrapped NB in the nanopit (middle), and again, the water filled nanopit (right). Note that in the area selected by a green dashed square in (a-c), three NBs remained after high load scan, though with reduced size compared to the ones obtained in (b). This is thought to be due to the existence of the large nanopit in the selected area. As reported previously, the concave surface structures help to stabilize NBs, leading to an increased NB immobility [66]. The enlarge 3D plot of the selected area is shown in the Appendix (Fig. 2.9).

On sample 2, nanopits with a larger range of width were obtained. The width of nanopits varies from about 50 nm to 250 nm. The PDFs of width and depth are again shown in the Appendix (Fig. 2.8). The influence of the nanopit size on the NB nucleation process can thus be investigated. The TMAFM image of sample 2 in air is shown in Fig. 2.2a. Figure 2.2b shows the image of the sample after immersion in DI water. The surface was again covered with spontaneously generated NBs. Compared with those obtained on sample 1, the NBs obtained on sample 2 have relatively uniform size. We believe that the uniform distribution of NBs on sample 2 is related to the spin coating speed during sample preparation. Sample 2 was made with a high spin coating speed, which can lead to an uniform roughness, thus resulting in uniform nucleation of NBs.

One can see that there are now three types of air entrapment on sample 2, as marked by 1, 2, and 3 in Fig. 2.2a and b. The mesh plots of the three selected areas are given in Fig. 2.2c, d, e, respectively. The first one is for the nanopits with width larger than 150 nm, as shown in Fig. 2.2c. The width and depth of the nanopit in water are the same as that in air, which means there is no air entrapped in the pit. The second one is for the nanopits with width in between 100 nm and 150 nm, as shown in Fig. 2.2d. On this kind of nanopits, planar NBs can be observed. From the cross section of the top AFM image, the measured depth of the nanopit in air was about 15 nm. However, the cross section of the profile becomes relatively flat in DI water, which is believed to be the entrapped air. The third case is for nanopits of less than 100 nm in width, as demonstrated in Fig. 2.2e. On these nanopits, regular NBs with higher contact angle are generated, similarly as already done on sample 1 above, with similar nanopit extensions. In this study, these NBs are referred to as protruding NBs.

The classification of planar and protruding NBs is based on the value of the contact angle. The contact angles of the nanobubbles were determined from the NB cross sections. Assuming that the NBs are spherical-cap-liked objects, their contact angles can be calculated by measuring their height and footprint diameter. However, it is well known that a topography image obtained from an AFM is actually the convolution of the AFM tip and substrate morphologies [78–80]. Therefore, the measured NB width needs to be corrected due to the finite size of the cantilever tip radius. In this study, the details of AFM tip deconvolution are included in the Appendix (Fig. 2.14a). For the NBs with width of 50-150 nm, the result shows that the apparent (uncorrected) width D of NBs is about 2-4 nm larger than their actual value D'. This results in about

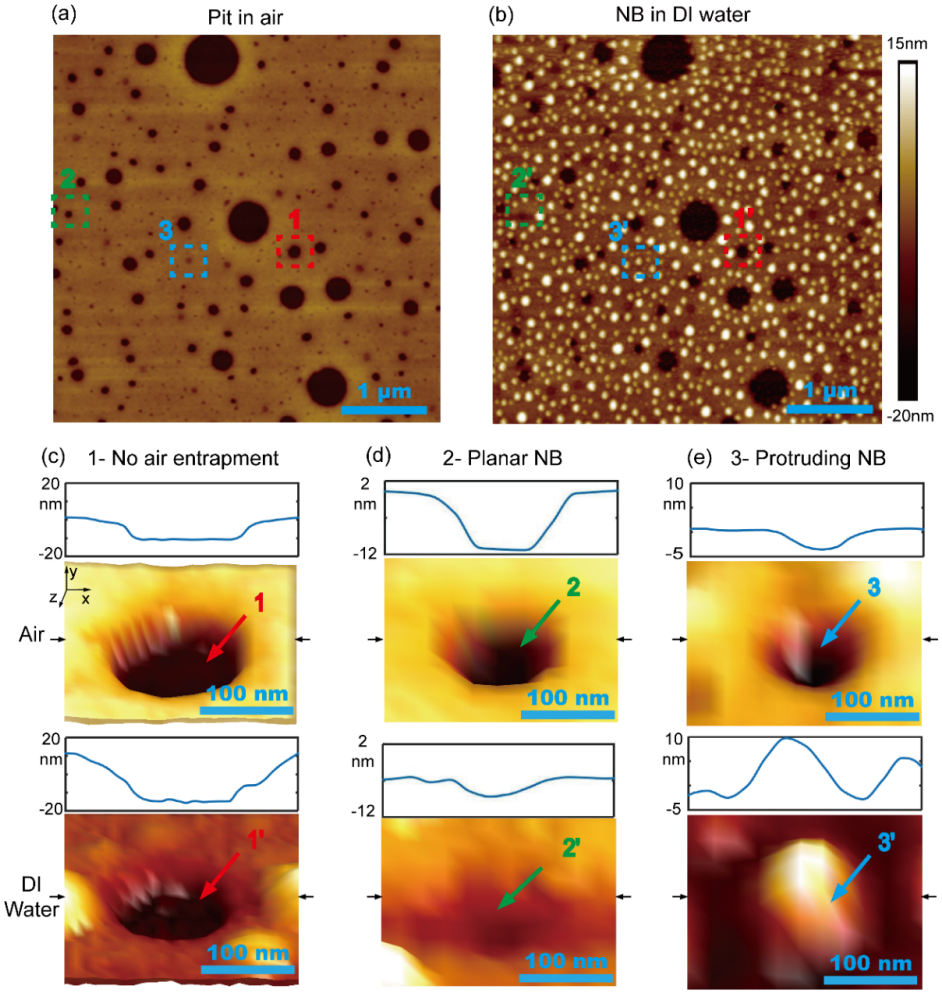

Figure 2.2: Entrapped nanobubbles on larger nanopits. (a) TMAFM image of nanopits with different widths on a PS film in air. (b) AFM image of the same area obtained in DI water. NBs were spontaneously generated in some nanopits on the PS film after the sample was immersed in DI water. (c-e) Comparison of three selected nanopits of different sizes in air (top row) and in DI water (bottom row) with cross section profiles. (c) A wide nanopit with no NB entrapped. (d) A medium nanopit with an entrapped planar NB. (e) A narrow nanopit with an entrapped NB of protruding profile.

2% underestimation of NB contact angle, as shown in a comparison of the corrected and uncorrected contact angles for protruding NBs in the Appendix (Fig. 2.14b).
With the corrected NB contact angles, the trapped NBs are classified into two groups (please refer to Fig. 2.15 (Appendix) for the detailed distribution of contact angles for trapped NBs). In this study, the NBs with contact angles of 0° or even slightly less are referred to as planar NBs. The others are protruding NBs, of which contact angles are normally larger than 10°.

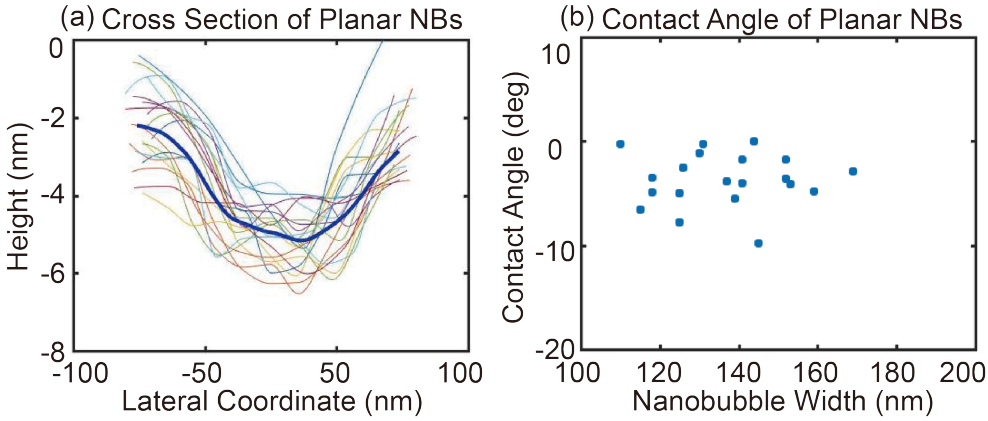

Figure 2.3: Geometric analysis of planar NBs. (a) Cross sections of all planar NBs in Fig. 2.2. Obviously, the real bubble shape corresponds to a minimal surface (spherical-cap) and the wiggles originate from AFM measurement noise. The blue thick curve is the average one of all the cross sections of NBs with the same lateral range from -70 nm to 70 nm in the figure, which indicates slightly concave cross sections of the nearly planar NBs. (b) Contact angle of all the planar NBs with an average value of -3.7° ± 2.5°

To get a better understanding of the profile for the planar NBs, the cross sections for all the planar NBs in Fig. 2.2 are presented in Fig. 2.3a. The profiles are mostly slightly concave. The blue thick curve in Fig. 2.3a is the average one of all the cross sections of the same size, from which it is clear that the cross section is slightly concave. The height H of planar NBs is thus slightly negative, and correspondingly also the contact angle. The measured contact angles for all planar NBs are shown in Fig. 2.3b, with an average value of -3.7° ± 2.5°.

From the above result, one can see that the types of NB nucleation are directly related to nanopit sizes. Air entrapment preferably occurs on nanopits with smaller diameter. Moreover, the nucleation on nanopits can be divided into three categories: no entrapment, planar NBs, and protruding NBs. For all NBs, we counted the numbers of NBs entrapped in nanopits on sample 1 and 2. A histogram of the three nucleation categories as a function of nanopit width is shown in Fig. 2.4a. The histograms of these three kinds of NB entrapment are fitted with normal distributions (dashed lines) in Fig. 2.4a. For all nanopits on the two samples, the results clearly show that the protruding NBs preferably form on smaller nanopits with medium size of 60 nm. For nanopits with width in between 100 nm and 150 nm, planar NBs are likely to be nucleated. For nanopits with width larger than 150 nm, generally no NBs were entrapped.
Moreover, experimental results show that the size of the protruding NBs is directly related to that of nanopits. Figure 2.4b shows the correlation between the width of NBs and that of the nanopits for the protruding NBs. The data were fitted with a linear relation with the least square method. The slope of the fitted line is 0.9246, which is close to 1. This indicates that the size of the entrapped NBs is basically the same as that of nanopits.
Additionally, the contact angle (gas side) of the entrapped NBs is in between 5° and 30° and increases with the NB width, as shown in Fig. 2.4c. We hypothesize that these small NBs are in diffusive equilibrium. For NBs in diffusive equilibrium, the stable equilibrium contact angle θ_e is determined by the air oversaturation ζ through the equilibrium condition [10, 19],

$$\sin\theta_e = \zeta \frac{L}{L_e} \tag{2.1}$$

where L is the pinning length and $L_c = 4\sigma/P_0 = 2.84$ μm, following from surface tension σ and ambient pressure P_0. The relation between $\sin\theta_e$ and the NB width L is given in Fig. 2.4d. Again, the data were fitted with a linear relation with the least square method. From the linear fit, we obtain $\zeta/L_c = 2.9$ μm^{-1}, corresponding to a (local) air oversaturation of $\zeta = 8.2$, which does not seem unrealistic to us.
The process of NB formation on nanopits can be thought of consisting of two steps, as illustrated in Fig. 2.5. The first step is air entrapment in surface cavities. Since PS is hydrophobic, the water will have a large advancing contact angle (Fig. 2.5a) on the PS films. During the immersion, as the fluid advances down to the bottom of the nanopits, by considering the narrow lateral size of the nanopits and high advancing contact angle, air pockets will be entrapped in the nanopits (Fig. 2.5b and c). It is due to air entrapment in

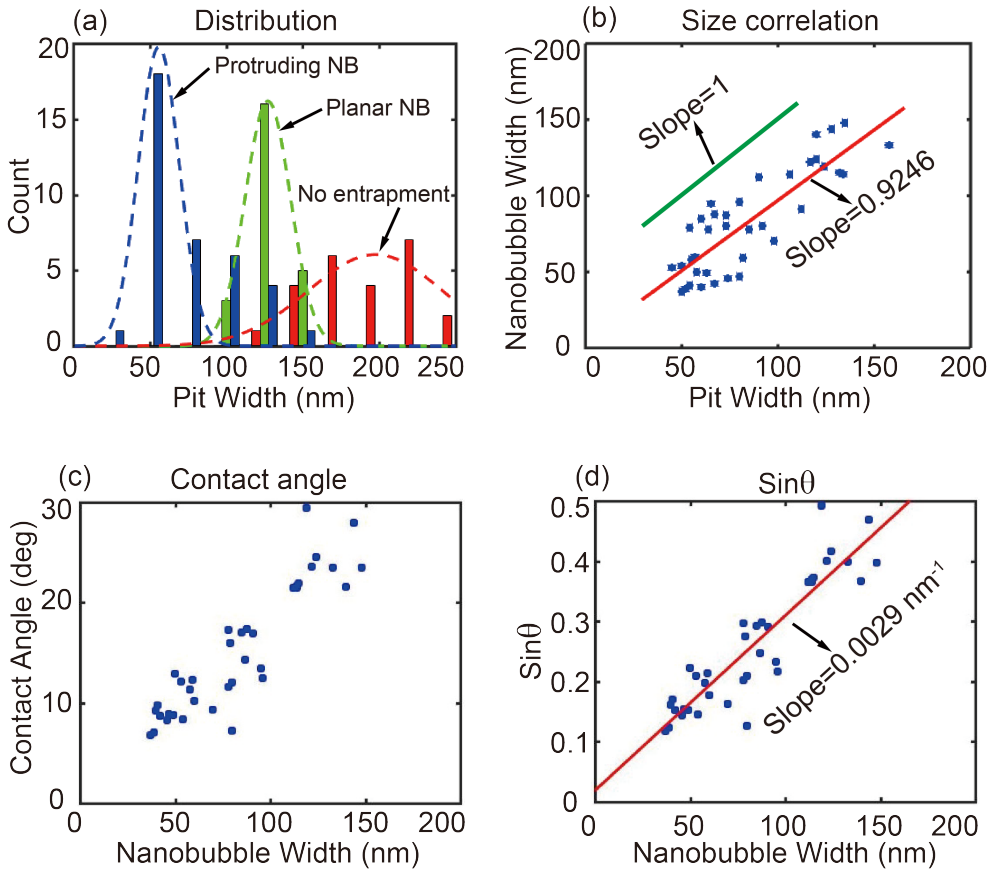

Figure 2.4: Statistic analysis of nanobubble entrapment on nanopits. (a) Histogram of the three different categories of NB nucleation in DI water. The protruding NBs and planar NBs preferably form on nanopits of 50-100 nm and 100-150 nm, respectively. However, when nanopits are larger than 150 nm, there are no bubbles entrapped. (b) Size correlation between the entrapped protruding NBs and nanopits. The size of nanobubbles linearly increases with that of nanopits. (c) Contact angle of NBs as a function of NB width for the protruding NBs. The contact angle increases with increasing NB width. (d) $\sin\theta$ *vs.* nanobubble width L. According to Eq. (2.1), the slope is $\zeta/L_c = 2.9$ μm^{-1}, corresponding to a gas oversaturation of $\zeta = 8.2$.

hydrophobic conical [52,81] and some other shapes of cavities [82], or in micro-protrusions of immersed superhydrophobic surfaces [83–85], *i.e.*, the crevices. During entrapment, the water has to retain its position at the pit mouth until the advancing contact angle of the fluid flow is obtained. As a result, nanopits with narrow lateral length will get air entrapped inside and form an initial gas-liquid interfaces. At this stage, the curvature of the advanced fluid will be towards the entrapped air direction. The process obviously depends on the degree of hydrophobicity, *i.e.*, on the advancing contact angle. This is consistent with the optical observation of the motion of the three-phase contact line on micropillar decorated superhydrophobic surfaces [86].

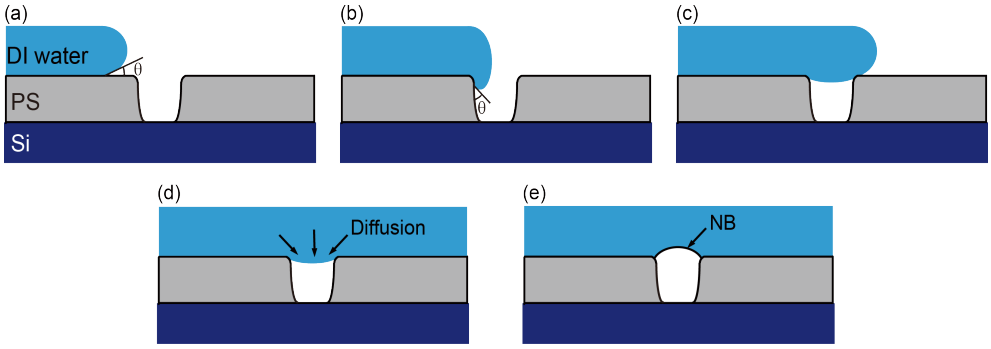

Figure 2.5: Illustration of a two-step formation of NBs. (a-c) Formation of air pockets in surface cavities. (d and e) Air diffusion through liquid-air interfaces.

The second step is the diffusive volume adjustment of NB originating from the entrapped air inside the nanopit. It is well known that the diffusion of gas from bubbles to fluid and vice versa plays an important role in NB dynamics and NB stability [10,19,49]. In this second step, the NB will grow out from the nanopits due to the diffusion of the air out of the locally oversaturated water (Fig. 2.5d), provided of course it is oversaturated. The curvature of the liquid interface inside the nanopit will start changing its direction outwards. Thanks to the diffusive influx, the liquid-air interface will grow out of the cavities until it reaches its equilibrium value determined by the air oversaturation in water. For nanopits with larger width, it might need much higher diffusive influx and the meniscus cannot so quickly appear above the nanopit mouth, *i.e.*, diffusive equilibrium may not be achieved.

This two-step NB nucleation model is consistent with the experimental observation. Based on the experimental results, a schematic is presented to illustrate the air entrapment on nanostructured surfaces (Fig. 2.6). There are three different cases, as shown in Fig. 2.6a, b, and c, respectively. For nanopits with a width of about 50 nm, NBs with protruding profiles can be obtained (Fig. 2.6a). For these NBs, the size linearly increases with the nanopit width and in diffusive equilibrium the contact angle increases with increasing NB width, according to Eq. (2.1).

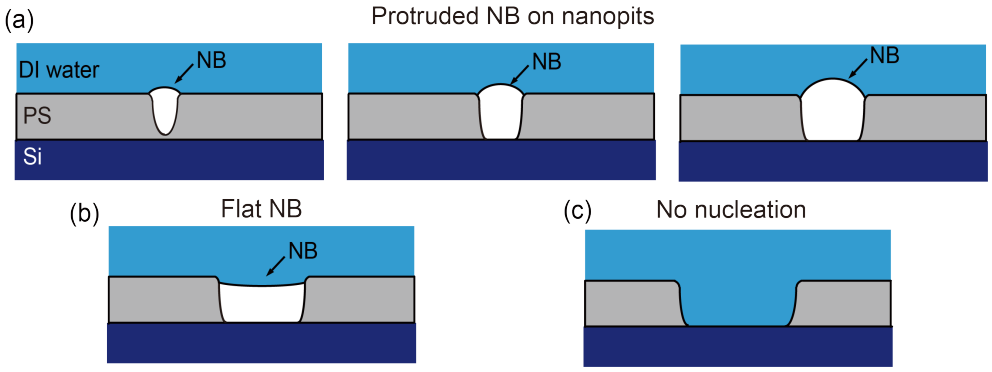

Figure 2.6: Illustration of three categories of air entrapment on nanopits. (a) Protruding NBs on smaller nanopits. The size of the entrapped NBs linearly depends on that of the nanopits and NB contact angle increases with increasing NB size. (b) Planar NBs with a concave gas-liquid interfaces formed in medium sized nanopits. (c) No entrapment. For larger nanopits, gas cannot be entrapped and there are no NBs observed.

When the nanopit width is in the range of 100-150 nm, entrapped air with flat liquid-gas interface can be obtained (Fig. 2.6b). Although these nanopits also entrapped air, the liquid-gas interface does not grow out of the nanopits. Regarding the reason to the formation of planar NBs, one reason could be that they are not in diffusive equilibrium yet. The diffusive timescale1 is $\tau_D \sim L^2\rho/Dc_s\zeta$, *i.e.*, $\propto L^2$, *i.e.*, for larger pits it takes much longer to equilibrate. In addition, for these medium sized nanopits, it requires more oversaturated air to make the gas-liquid interfaces grow out of the nanopits and depletion effects may occur. For even larger nanopit size beyond 150 nm, based on the crevice model, the nanopits do not favor air entrapment and no NB nucleate

(Fig. 2.6c).

2.3.2 Are nanobubbles always spherical-cap-shaped?

The experimental results obtained from sample 1 and sample 2 reveals that the size and position of the formed NBs could be tuned by modifying the nanostructures. NBs are normally believed to be of spherical-cap-shaped, as that shape is energetically the most effective one. However, stable NBs also require pinning and thus their shape may also be tuned by that of the surface nanostructures. Indeed, by surface energy minimization, Dević *et al.* showed how chemical heterogeneities determine the shape of nanodroplets [87]. For a non-circular chemical or geometric surface pattern, it may indeed be energetically advantageous for a NB or nanodrop (ND) to have a non-circular footprint.

In this study, an ultrathin PS film (sample 3) was used to generate a porous surface with irregular shapes of pores. The nanopores were fabricated with assistance of NBs. As previous revealed [43], when an ultrathin PS film is immersed in DI water, small NBs first disappear and leave nanopores on the surface. The formation of nanopores is due to surface forces along the three-phase contact line of the NBs and high inner pressure. With the decreased PS film thickness (ultrathin one, in this case), its elastic modulus and fracture strength will be reduced as compared to the bulk values. The interaction between the film and the NBs will disentangle the PS chain and lead to the formation of irregular shapes of nanopores.

A TMAFM image of the porous surface fabricated with assistance of NBs is shown in Fig. 2.7a. Unlike the circular shapes of the nanopits shown on sample 1 and sample 2, here the nanopores on sample 3 have irregular shapes. After sample 3 was immersed into DI water, NBs were formed on the surface. The height image is shown in Fig. 2.7b. From the figure, we can see that the shape of the NBs is very different as compared to the regular NBs on the circular pits. This can be better seen in the phase image (Fig. 2.7c), which clearly shows that the shape of NBs is no longer circular. Figures 2.7d and e show 3D mesh plot of selected areas in Fig. 2.7a and b, respectively. In the 3D images, the nanohole is no longer circular and the NB is not spherical-cap-shaped any more, but shows an irregular shape.

The existence of stable non-spherical-cap-shaped NBs highlights the relevance of pinning for NB formation, namely here at the edge of the irregular surface cavities on sample 3. On regular smooth sample surfaces with rms (root mean square) roughness about 0.2 nm [77] or on the circular nanopits shown on

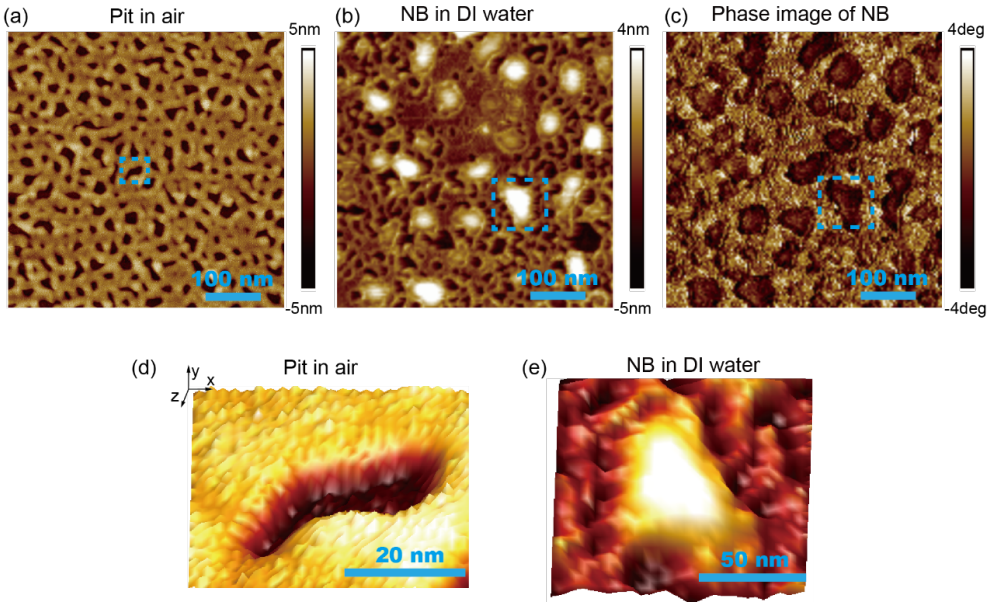

Figure 2.7: Illustration of three categories of air entrapment on nanopits. (a) Protruding NBs on smaller nanopits. The size of the entrapped NBs linearly depends on that of the nanopits and NB contact angle increases with increasing NB size. (b) Planar NBs with a concave gas-liquid interfaces formed in medium sized nanopits. (c) No entrapment. For larger nanopits, gas cannot be entrapped and there are no NBs observed.

sample 1 and 2, NBs are spherical-cap-shaped. Indeed, the shape of the NBs is determined by two factors. One is the interfacial free energy of the NB, the other is the constraint from the pinning of the three-phase contact line of the NB. The pinning forces can be considerable. Tan *et al.* [88] found that a pinning force up to 0.1 μN is required to unpin bubbles of several micrometers, which corresponding to 5 mN/m unpinning force to detach bubbles. Similarly, as in above mentioned numerical study of NBs and NDs on chemically heterogenous surfaces [87], also here the surface geometrical heterogeneity plus the minimized interfacial free energy determine the shape of the NBs. On sample 3, the three-phase contact line of NBs can only lie on the ridge area of PS (see Fig. 2.7a). In other words, the pinning sites provided by the ridge area, together with the minimized free interfacial energy, determine the shape

of the NBs.
The non-spherical-cap-shaped NBs indicate that the NB footprint is directly related to the corresponding surface nanostructure to which it is pinned. NBs can change their shape to adapt to that of the surface nanostructures on substrates and they do not necessarily be spherical-cap-shaped. This implies that not only the size and locations of the NBs, but also the shape of NBs can be tuned by nanostructures.

2.4 Conclusions

In summary, the spontaneous nucleation of NBs on nanostructured surfaces was investigated. Three categories of air entrapment were observed, namely protruding NBs on nanopits with widths in between 50-100 nm, planar NBs on nanopits with widths of 100-150 nm, and no air entrapment on nanopits with diameter larger than 150 nm. The size of the entrapped NBs linearly increases with that of nanopits. A two-step nucleation process was used to explain the entrapment of NBs on surface nanocavities. Air is first entrapped by surface cavities during immersion with the formed liquid-air interfaces. After that, air dissolved in the locally over-saturated liquid diffuses into the air pockets. Then the air pockets grow out of the cavities, determining the final volume of the NBs. Moreover, air entrapment experiments on a porous PS surface covered with irregular nanopores show that the shape of NBs can also be tuned by surface nanostructures, due to their pinning effect. It is thus feasible to tune NB size, position, and even morphology by varying surface nanostructures.

2.5 Appendix

2.5.1 Distributions of the width and depth of the nanopits on samples

As mentioned above, nanopits of different sizes were obtained on PS films. For sample 1, the distributions of the nanopits' width and depth are shown in Fig. 2.8a and 2.8b, respectively. The nanopit width distributed from 50 nm to 100 nm. The nanopit depth mostly changed in between 1 to 6 nm. There was one nanopit with a depth of 12 nm, which reached down to the silicon substrate. Figure 2.8c shows the correlation between width and depth.
In the analysis of Fig. 2.1, we found that three NBs remained on their initial locations around a large nanopits after NB coalescence. In the area selected

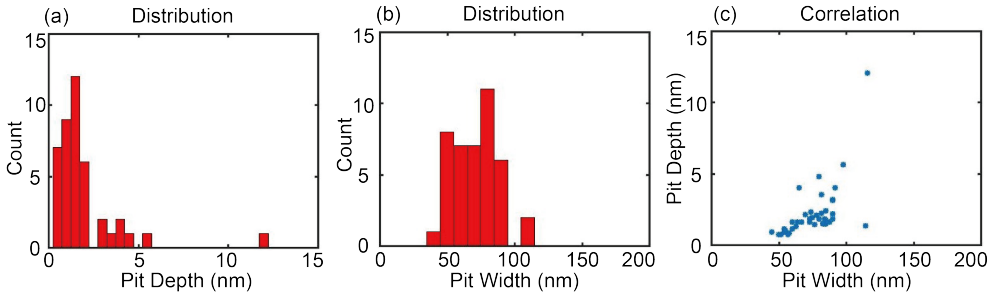

Figure 2.8: Width and depth distribution of nanopits on sample 1. (a) Histogram of nanopit widths on sample 1. The nanopit width changed from 40 nm to 110 nm. (b) Histogram of nanopit depths on sample 1. The nanopit depths distributed from 1 nm to 6 nm. The correlation between width and depth is shown in (c).

by a green dashed box in Fig. 2.1c, one can see that the three NBs remained after NB coalescence. Figure 2.9 shows the zoom-in mesh plots of the selected area in Fig. 2.1a-c. As mentioned in the main manuscript, this is thought to be due to the existence of the large nanopit in the selected area, providing strong pinning sites. For sample 2, the distributions of nanopits' width and

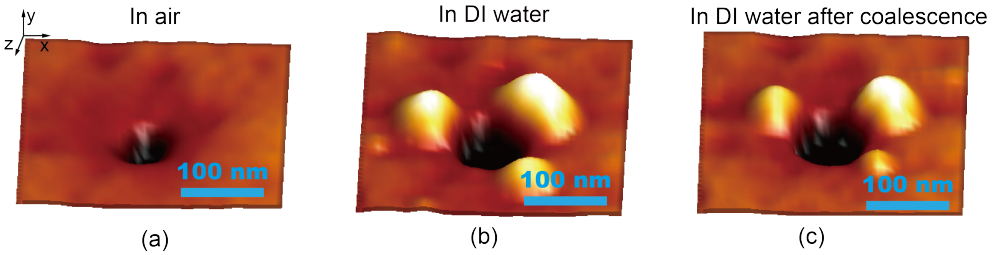

Figure 2.9: A deep and large nanopit on sample 1. 3D mesh plots of the same areas selected in Fig. 2.1. One can clearly see the topography of the nanopit in air (a), in DI water (b), and after coalescence (c).

depth are shown in Fig. 2.10a and 2.10b, respectively. On the sample, one can see that the nanopit widths mainly distributed from 50 nm to 250 nm.

The nanopit depths distributed in two sections, 3-4 nm, and 10-13 nm. For the nanopits of which depth located in the section section (10-13 nm), they reached down to the bottom of the silicon substrate.

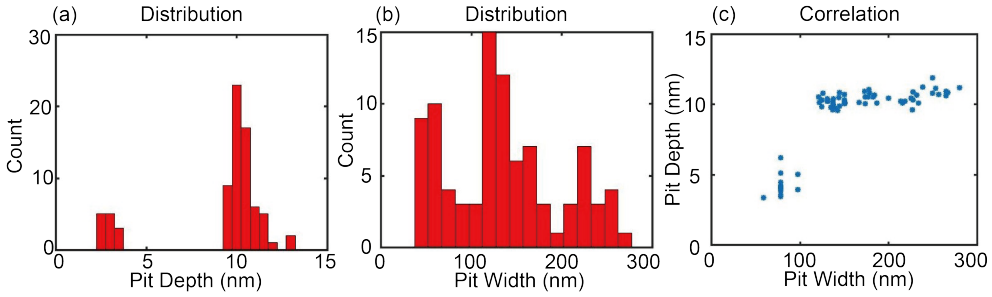

Figure 2.10: Width and depth distribution of nanopits on sample 2. (a) Histogram of nanopit widths on sample 2. The nanopit widths mainly changed from 50 nm to 250 nm. (b) Histogram of nanopit depths on sample 2. The nanopit depths distributed in two sections, 3-4 nm, and 10-13 nm. (c) Corrrelation of width and depth.

2.5.2 Nanobubble Verification Experiment

Studies on surface NBs have been suffering from artifacts for years as explained in [10, 46]. For the samples used in this study, there are potentially three kinds of artifacts, namely solid particles, liquid objects [46], and blisters [89]. To value out such artifacts, several experiments were designed and conducted to verify that the spherical objects we observed were indeed NBs. In this Appendix, we report the result of several verification experiment.

Nanobubble Coalescence Experiment

The nanobubble coalescence experiment was performed to distinguish nanobubbles from solid particles and blisters. It is well known that nanobubbles can move and coalesce to generate larger ones under higher scan load [66, 75, 76]. However, blisters and solid objects cannot coalesce. In this study, we performed NB coalescence experiment on PS samples. The result for one of these experiments is show in Fig. 2.11. Figure 2.11a is a height image of the sample surface obtained with 96% setpoint value in TMAFM after the sample was

immersed into DI water. One can see that nanobubbles with width about 100 nm were obtained on the sample surface. To conduct coalescence experiment, we first apply 80% setpoint to scan the area. After that, the area was re-scanned with 96% setpoint. The resulting image is shown in Fig. 2.11b. One can see that nanobubbles with much larger size were obtained with reduced density. If the spherical objects were solid particles or blisters, they could not be coalesced in this way. Therefore, one can conclude that the spherical-cap like objects were neither solid particles, nor blisters.
Moreover, the NB volumes before and after the coalescence were measured with a home-made NB image segmentation algorithm [76]. To do so, the AFM images of the NBs were first segmented. The results are shown in Fig. 2.11c and 2.11d for NB images shown in Fig. 2.11a and 2.11b, respectively. With the segmented NB images, the NB volumes were calculated. The total volumes of NBs in Fig. 2.11a and 2.11b are about 3.7×10^6 nm^3 and 7.1×10^6 nm^3, respectively. The obtained result is in a good agreement with what we reported recently [76]. The increased NB volume after NB coalescence may partly be explained by the reduced Laplace pressure in the larger NBs, and partly be by diffusion of dissolved gas into the merging process. A quantitative analysis of these two effects is beyond the scope of the present paper.

Tip-Sample Interaction Experiments

The second approach to distinguish NBs from solid particles and blisters is an amplitude-distance curve measurement above the spherical-cap-like objects. During extension or retraction motion of an oscillating tip relative to a NB, the amplitude of the tip shows gradually decreases with reducing tip-sample separation distance [75, 77]. However, the oscillating amplitude of AFM tips rapidly decreases once they get into contact with surfaces of solid particles or blisters, very different from the behavior of nanobubbles. One example of the amplitude-distance curve of AFM obtained on a spherical-cap like object is given in Fig. 2.12. Figure 2.12a is an AFM height image of the PS sample surface (sample 1). In the center area, there is a big spherical-cap-like object. We measured amplitude-distance curves on the object and obtained two kinds of curves. Here we took amplitude-distance curves obtained at two selected points (marked as 1 and 2). The results are shown in Fig. 2.12b.
One kind of curve is the one obtained above the substrate (point 1 in Fig. 2.12a). Once the tip contacts the substrate, the amplitude rapidly decreases with decreasing tip-sample separation distance. The other kind of curve is the one obtained above the spherical-cap like domains (point 2 in Fig. 2.12a).

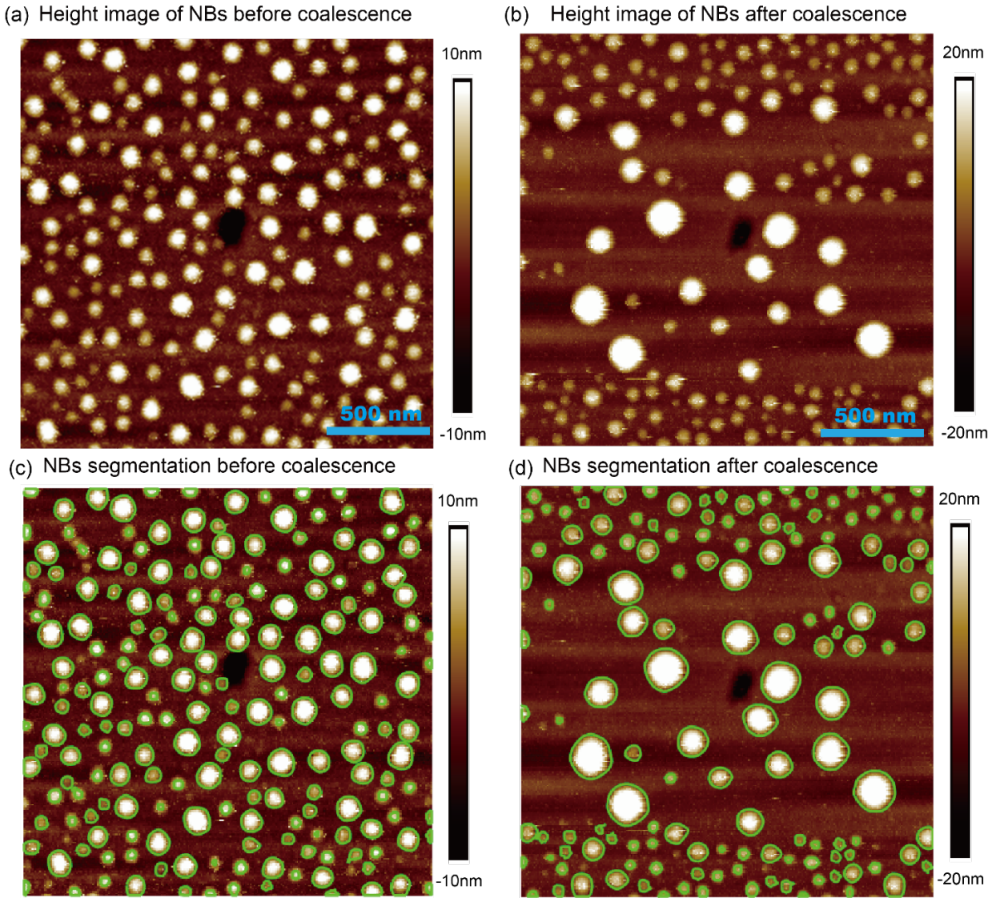

Figure 2.11: Nanobubble coalescence performed on a PS surface. (a) AFM height image of the sample surface after immersed into DI water. (b) AFM height image of the same area after a higher scan load was applied. Nanobubbles at lower number density, but much larger size were obtained, indicating nanobubble coalescence. (c-d) NB image segmentation for NB height images in (a) and (b), respectively. The green contours are detected NB boundaries with a homemade NB segmentation algorithm.

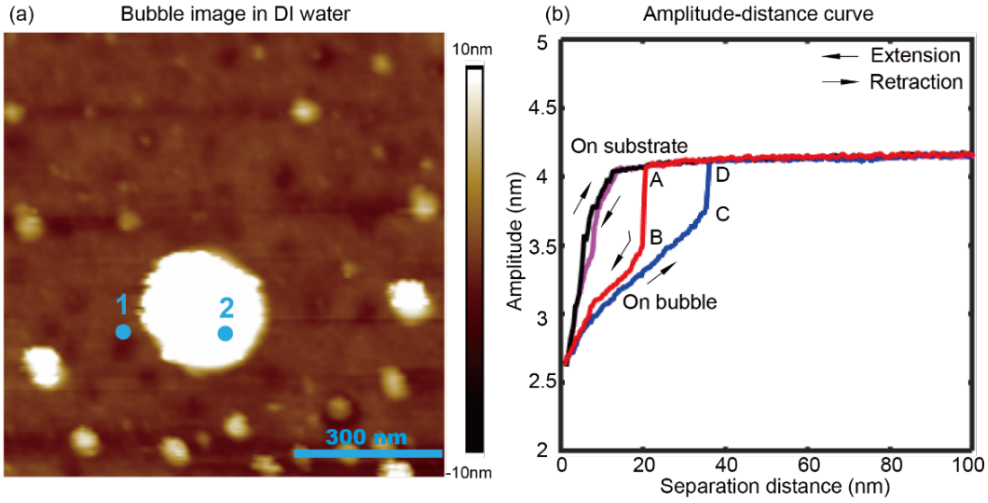

Figure 2.12: Amplitude-distance curve measurement on a spherical-cap like object and sample substrate. (a) AFM height image of the sample surface in DI water, showing a big spherical-cap like object in the center. (b) Two typical amplitude-distance curves measured at point 1 and 2, respectively.

One can see that the obtained result is consistent with the one of our recent investigation [77]. As described there [77], there are typical snap-in period A $\rightarrow$ B and detached period C $\rightarrow$ D, which corresponds to the position where the AFM tip gets and loses contact with the object, respectively. The tip-sample interaction further confirms that the obtained spherical-cap like objects were not solid ones, neither blisters.

Degassing Experiments

To distinguish NBs from liquid contamination (PDMS droplets, for example), we applied degassing experiments [15,46,64]. For a PS sample, we first imaged the sample surface in air. The image is shown in Fig. 2.13a. One can see that the surface is flat without any spherical-cap like objects. After that, the sample was immersed into DI water. We first obtained spherical-cap like objects on the sample surface, as shown in Fig. 2.13b. Then, the AFM liquid cell with the sample immersed in water was transferred into a vacuum chamber to degas the water for over 4 hours. After that, the liquid cell was brought back to

AFM and was re-scanned. The result is shown in Fig. 2.13c. One can see that the spherical-cap like objects had all disappeared. This implies that the observed spherical-cap like objects were actually gas bubbles and not droplets of a poorly solvable liquid.

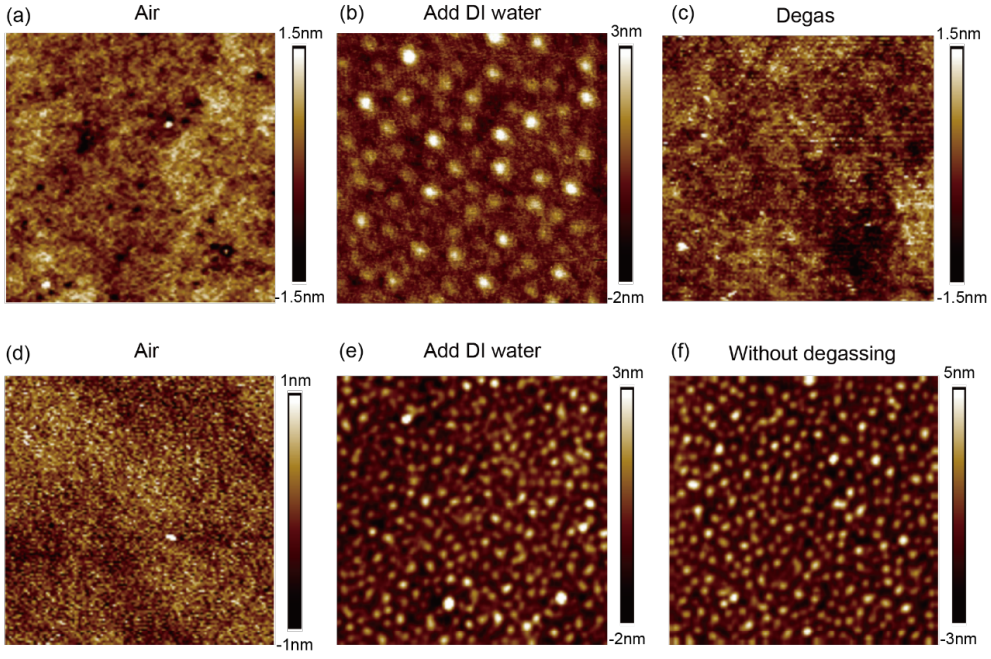

Figure 2.13: Degassing experiment. (a) A PS sample surface obtained with tapping mode AFM in air. (b) Spherical-cap like objects obtained on the sample surface after it was immersed into DI water. (c) AFM height image of the same sample after the liquid cell (the sample remained in water during degassing) was kept for 4 hours in a vacuum chamber for degassing. The NBs have dissolved.

2.5.3 Deconvolution of Tip Radius and Correction of NB Contact Angles

It is well known that a topography image obtained from an AFM is actually the convolution of the AFM tip and substrate morphologies. Therefore, the measured NB width needs to be corrected due to the finite size of the cantilever

tip radius. In the case of the spherical-cap-liked NBs, the influence of the AFM tip on the contact angles of the protruding NBs is illustrated in Fig. 2.14a. In the figure, the dashed cross section is the directly measured one from AFM

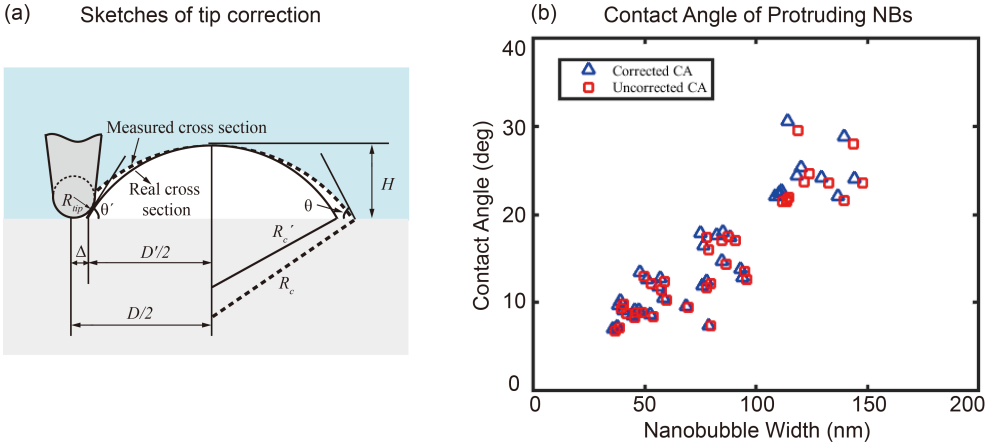

Figure 2.14: (a) Schematic sketch of the NB size correction through deconvolution of the tip radius. (b) Comparison of the corrected and uncorrected contact angle (CA) for protruding NBs. The difference between the corrected contact angle and uncorrected ones is slight.

images, while the solid one is the NB's actual cross section. From the figure, one can see that the tip radius causes overestimation of the NB width. The deconvolution of the AFM tip gives a corrected expression of the NB radius, width, and contact angle, namely

$$R'_{\mathrm{c}} = \frac{(D)^2+4H^2}{8H} - R_{\mathrm{tip}}\,, \tag{2.2}$$

$$D' = \sqrt{D^2 - 8HR_{\mathrm{tip}}}\,, \tag{2.3}$$

$$\theta' = 2\arctan\left(2H/D'\right), \tag{2.4}$$

where D' and D, θ' and θ, R'_c and R_c, H' and H ($H' = H$) are the actual and apparent (uncorrected) values of width, contact angles, radius of curvature, and height of the NB, respectively, and R_{tip} is the tip radius (about 8 nm in this case).

With Eq. (2.4), NB contact angle can be corrected. For the NBs with width of 50-150 nm, we found that D is about 2-4 nm larger than D'. A comparison of the corrected and uncorrected contact angle of NBs is conducted to evaluate the effect of finite size of tip radius on contact angle measurement, as shown in Fig. 2.14b. From the result, one can see that the uncorrected CA is slightly lower (about 2%) than that of the corrected one. The classification of planar and protruding NBs is based on the value of their contact angles. The distribution of contact angles for all trapped NBs is shown in Fig. 2.15. In this study, the NBs with contact angles of 0° or even slightly less are referred to as planar NBs. The others are protruding NBs, of which contact angles are normally larger than 10°.

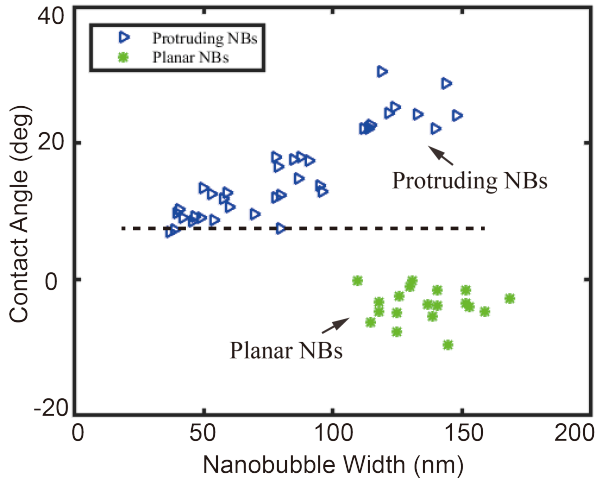

Figure 2.15: Corrected contact angles for all trapped NBs (planar and protruding). The contact angle for planar NBs is mostly less than 0°. The dashed horizontal line in the figure divides the trapped NBs into two categories: protruding and planar NBs.

Chapter 3

Entrapment and dissolution of microbubbles inside microwells[1]

The formation and evolution of immersed surface micro- and nanobubbles are essential in various practical applications, such as the usage of superhydrophobic materials, drug delivery and mineral flotation. In this work, we investigate the entrapment of microbubbles on a hydrophobic surface, structured with microwells, when water flow passes along, and the subsequent microbubble dissolution. At entrapment, the microbubble is initially pinned at the edge of the microwell. At some point, the three phase contact line detaches from one side of the edge and separates from the wall, after which it is further receding. We systematically investigate the evolution of the footprint diameter and the contact angle of the entrapped microbubbles, which reveals that the dissolution process is in the constant contact angle mode. By varying the gas undersaturation level, we quantify how a high gas undersaturation enhances the dissolution process, and compare with simplified theoretical predictions for dissolving bubbles on a plane surface. We find that geometric partial blockage effects of the diffusive flux out of the microbubble trapped in the microwell lead to reduced dissolution rates.

[1]Published as: **Xiaolai Li**, Yuliang Wang, Binglin Zeng, Yanshen Li, Huanshu Tan, Harold J. W. Zandvliet, Xuehua Zhang, and Detlef Lohse, *Entrapment and dissolution of microbubbles inside microwells*, Langmuir. **34**, 10659-10667 (2018). Experiments and writing are done by Li, supervision by Wang, Zandvliet and Lohse.

3.1 Introduction

Submicron surface bubbles, namely nanobubbles at solid-liquid interfaces with heights between 5 and 100 nm and footprint diameters between 50 and 800 nm, have extensively been studied over the last two decades [10]. The surface bubbles play an important role in various chemical and physical processes and have numerous potential applications [41], such as mineral flotation and separation [4], transport in nanofluidics devices [90], nanostructured surface fabrication [45,91] or application in the context of catalysis and electrolysis [92, 93]. So far various theoretical and experimental studies have been performed to investigate surface nanobubbles [9, 60] and their intriguing properties, such as their stability, their small contact angle and collective effects [10, 46, 77, 88, 94]. Surface nanobubbles can be obtained by several methods [10], such as solvent exchange [9], spontaneous generation at immersion [60], and electrochemical or catalytic production [95], *etc.* However, it is still challenging to achieve full control over the formation of surface nanobubbles.

To achieve such controllable generation of nanobubbles, it is essential to understand the formation mechanism. The so-called crevice model has been proposed to explain the formation mechanism of nucleating surface micro and nanobubbles, *e.g.* under pressure reduction [96, 97]. According to this model, gas is entrapped in crevices on surfaces and forms bubble nuclei. These bubbles nuclei can then grow by diffusion of gas from the surrounding oversaturated liquid or due to expansion upon a reduction of the liquid pressure. Numerous experimental studies have been conducted at microscale to validate this nucleation model. For example, techniques such as centrifugation, shock wave, and acoustics were applied to drastically reduce the liquid pressure to a negative value to find the cavitation pressure threshold [53–56]. These studies mostly focused on controlling the liquid condition after gas entrapment. However, the detailed entrapment process, namely the entrapment dynamics, in which surface structures play an important role because they affect liquid flows and provide pinning sites, was less studied.

Several previous studies have used structured surfaces to explore the nucleation mechanism and controllable interfacial nanobubble formation [18, 57, 98, 99]. With nanopatterned hydrophobic/hydrophilic surfaces, Agrawal *et al.* [17] found that interfacial nanobubbles only nucleate on hydrophobic domains. In our previous work [99], the in-situ entrapment of nanobubbles was observed with an atomic force microscope (AFM). The size of the nucleated surface nanobubbles is linearly correlated with that of the surface nanopores

on hydrophobic surfaces, which supports that the nanobubbles form from gas entrapment on the nanoscopic cavities. Although the entrapped nanobubbles have been observed in these works, further investigation on the entrapment dynamics is extremely challenging due to the limited temporal resolution of the measurement equipments at nanosacle, e.g. AFM. Essentially, the entrapments of surface microbubbles and surface nanobubbles share the same mechanism. Therefore, the investigation of nucleation dynamics of surface microbubbles, which is experimentally feasible to be visualized, will lead us to a better understanding of the nanobubble entrapment dynamics.

Recently, Langley *et al* [100] demonstated the entrapment based microbubble formation and observed the dynamical process in their work. They studied air entrapment by performing drop impacts experiment on nanoparticle decorated surfaces. As the drops approach the solid surfaces, a central air disc is entrapped due to deformation of the drop by the intervening air layer. After the drops touch the sample surface, the liquid blocks the escape path for the gas, leading to the entrapment of micro-bubbles in surface structures. The size of the microbubbles depends on the lateral roughness variation. These results confirm that bubble nucleation is mediated by gas entrapment and shed light on the dynamics of the nucleation.

In this study, we aim to reveal entrapment and diffusive dynamics of surface microbubbles. Our work can provide (i) a better understanding of the surface bubble nucleation mechanism and (ii) a potential method of reproducible micro- and nanobubbles formation. Here we investigate the temporal evolution of the surface microbubbles entrapped by microwells on hydrophobic surfaces using a confocal microscope. In order to study the effect of the microwell diameter on entrapment and dissolution effectivetly, we prepared wells with different sizes on one sample. We will show that the microwells can be used to trap surface microbubbles. After that, the trapped surface microbubbles will dissolve. The detailed process of microbubble dissolution, as well as factors such as gas concentration and lateral size of surface microstructures on the microbubble dissolution will be investigated in detail.

3.2 Experimental section

3.2.1 Preparation of sample and its characterization

Two solutions, PS-toluene and water-acetone, were prepared to fabricate the structured polystyrene (PS) surface on a glass substrate. The PS-toluene

solution was prepared by dissolving PS particles (molecular weigh 350 000, Sigma-Aldrich) into toluene (Mallinckrodt Chemical) with a concentration of 1.0% (weight). The water-acetone solution was made by mixing water and acetone with water concentration of 5.0%. The two solutions were first mixed with a ratio of 1:3 (volume, PS toluene to water acetone). About 200 μL of the mixed solution was then dropped on a piece of glass substrate (20mm$\times$20mm). The deposited droplet solution will rapidly spread over the glass substrate. Due to the lower solubility in the acetone - water mixture as compared to in toluene, PS precipitates from the mixed solution and deposits on the glass substrate to form a film. Among the three different liquids (acetone, toluene, and water), acetone has the highest evaporation rate, followed by toluene. As a result, the water droplets remain on the PS film after acetone and toluene have evaporated within several seconds. Eventually, the remaining water droplets will also evaporate within about ten minutes and the PS film with microwells (at the locations where the droplets were) remains.
The morphology of the surface was measured with an AFM (Resolve, Bruker) in tapping mode, as shown in Fig. 3.1a. The width of the microwells is in between 10 μm and 80 μm. We confirm that the bottom of the microwells is also coated by PS film by scratching it with an AFM tip (NSC36/ALBS, MicroMasch). The thickness of the film at the bottom of the microwell is about 30 nm, whereas the film itself is in between 0.8 μm and 1.2 μm. It is noteworthy to point out that there are other surface preparation techniques available that are able to produce more mono-disperse distributions of microwells. In this work it is of key importance to have mircowells with different diameters as we want to study the effect of the bubble diameter on the entrapment and the dissolution dynamics of the bubble.
To estimate the surface hydrophobicity, a water drop of 5 μL was put on the surface. The static contact angle of about 109° (on the droplet side) was obtained using a video-based optical contact angle measuring system (Data-Physics OCA15 Pro), see Fig. 3.1b. This contact angle is slightly larger than that of around 95° obtained on continuous PS films [76]. Such surface microwells can be applied in many applications [101–103], including serving as cell containers or scaffolds for cell growth [104, 105], micro-reactors for chemical reactions [106], and nucleation sites for photonic crystals [107, 108].

3.2.2 Water deposition and gas concentration control

During the experiment, the prepared micro-structured PS sample was clamped in a home designed microfluidic chamber. Then 3 mL deionized water (Milli-Q

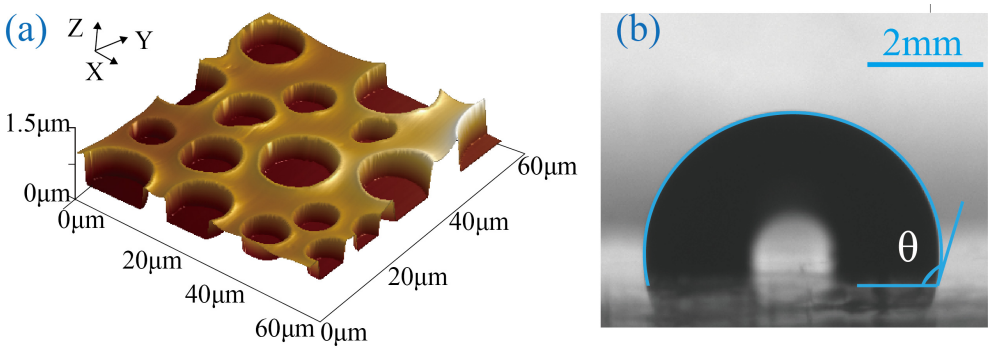

Figure 3.1: (a) Characterization of the structured PS surface. Three dimensional morphology of the sample surface obtained with AFM. Microwells with different sizes were obtained on the surface. (b) A side view image of a sessile drop on the sample surface, indicating a water contact angle of $\theta = 109° \pm 0.2°$ degree.

Advantage A10 System, Germany) was deposited on the surface. This leads to air bubble entrapment in the pits. The flow rates were controlled by a motorized syringe pump (Harvard; PHD 2000). The temporal evolution of the entrapped micro-sized surface bubbles was observed using a laser scanning confocal microscope (LSCM, Nikon Confocal Microscopes A1 system) with a 60× water immersion objective (CFI Apochromat 60XW NIR, NA = 1, WD = 2.8 mm). To obtain the actual morphology of the structured surface, the sample was first immersed into fully degassed water (the gas concentration is 0.2 measured by an oxygen meter (Fibox 3 Trace, PreSens)), and subsequently was scanned with the confocal microscope.

To test the effect of the gas concentration on the microbubble dynamics, the experiment was conducted in both (nearly) air equilibrated water (AEW) and in partially degassed water (PDW). In the AEW experiment, a sample bottle containing water was kept open in air for 10 hours. The measured gas concentration in the nearly air saturated water is 96.0%. For the PDW, the milli-Q water was degassed for 3 mins in a home-made vacuum chamber. After partial degassing, the measured air concentration was 63.0%. For visualization, water was labelled in yellow color with fluorescein isothiocynate-dextran (Sigma-

Aldrich, molecular weight, 70000). During experiments, water flow rates from 0.5 mL/min to 3.0 mL/min were applied. All images were captured with the confocal microscope.

3.3 Results and Discussion

3.3.1 Entrapment of surface microbubbles

When the flow front passes over the structured hydrophobic surface, air pockets are entrapped in the microwells [52, 82, 109]. The air entrapment happens due to the large advancing contact angle in combination with the surface structure size, as explained by the crevice model [52]. The entrapped air then first remains in the micropits, as surface microbubbles are pinned to the edge of the surface cavities.

We subsequently observed the diffusive evolution of the entrapped surface microbubbles in the microwells. To get the actual topography of the structured surface before air entrapment, the sample was first immersed into fully degassed water. The bottom view of the microwell is shown in Fig. 3.2(a). The circular areas with a green color indicate that no microbubble entrapment occurred in the fully degassed water (or the entrapped microbubbles dissolved immediately, see below). After that, the fully degassed water was removed.

The AEW was then injected into the microfluidic chamber. Subsequently the sample was fully immersed in AEW, and we immediately captured the image of the entrapped microbubbles. At this stage the microwells were fully filled with gas. After a certain time, part of the three phase contact line detached from the edges of the microwells and the initially trapped microbubbles rapidly shrank, reducing their lateral sizes. Figure 3.2b depicts the area captured right after the sample was immersed into water. Due to the limited frame rate of the LSCM (4 fps was applied to achieve an optimized imaging), the initial shrinkage for some of microbubbles was not captured. As a result, some of the initially entrapped microbubbles shrank within the first frame. The areas marked by yellow circles correspond to the initially entrapped microbubbles, while the ones marked by yellow rectangles are the shrinking microbubbles.

Figures 3.2c-e show sequential images of the dissolving surface microbubbles. Noticeably, in Fig. 3.2c the appeared bubbles in the bottom left quadrant are formed from depinning of the previous entrapped bubbles, which are marked with yellow circles in Fig. 3.2b. In additon, we observed that a bubble appears between two microwells (top left quarter). According to the sequential images

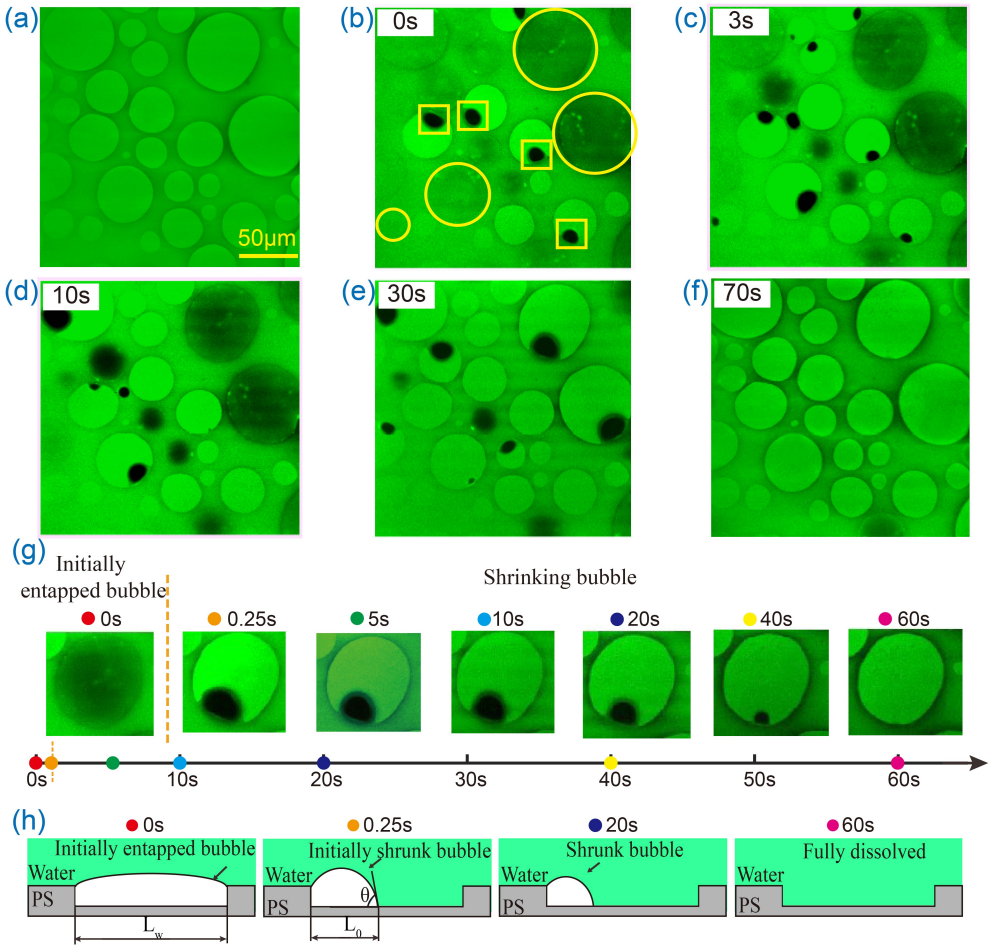

Figure 3.2: Evolution of the entrapped microbubbles in air equilibrated water. (a) The structured polystyrene surface captured in degassed water, showing the distribution of microwells on the surface. (b)-(f) Confocal microscopy images of the selected surface area at different times. The dark circular areas marked by yellow circles are the microwells covered by the initially entrapped microbubbles. The areas marked by yellow rectangles are the shrinking microbubbles. During shrinkage, the three phase contact line keeps receding towards a pinned spot until the microbubble disappears completely. (g) The sequential images of an entrapped microbubble on a microwell. Initially, the microwell was completely filled by the entrapped microbubble. Then part of contact line detaches from the edge of the microwell and the formed microbubble gradually shrank and eventually disappeared. (h) Schematic of the three phases of air entrapment in a microwell, fully entrapped, shrinking, and fully dissolved.

between Fig. 3.2b and c, we confirm that it jumps out of the well from its right side. In Fig. 3.2f, all entrapped microbubbles have disappeared.
In Fig. 3.2g, the sequential images of an initially entrapped microbubble and the corresponding shrinking microbubble in the microwell are presented. Initially, the three phase contact line was pinned at the edge of the microwell and the complete well was covered by the air-water interface, as illustrated in Fig. 3.2h (left). After a certain period, the three phase contact line detached from the edge of the well from one side and the microbubble rapidly shrank in size. The microbubbles right after the initial shrinking are referred to as initially shrunk microbubbles, as illustrated in Fig. 3.2h (middle). Subsequently, the microbubble will gradually further shrink and eventually disappear (Fig. 3.2h (right)). The time required for the transition from the initially entrapped microbubbles to the initially shrunk microbubbles is much shorter than the following shrinkage period. Here the frame which was taken right after the initial shrinkage is taken as the first frame for the analysis of the diffusive microbubble shrinkage dynamics.
Our results show that the lateral width L_0 of the initially shrunk microbubbles are related to the size of the microwells. Figure 3.3a depicts the correlation between L_0 and the microwell diameters L_w. One can see that L_0 linearly increases with L_w, with a slope of 0.34. This linear dependence is independent of the flow rates, at least for the applied flow rates of 0.5, 1.0 and 3.0 mL/min. This implies that larger microwells are able to trap more gas. The contact angles always measured on the gas side of the initially shrunk microbubbles are also size dependent. As shown in Fig. 3.3b, the contact angles of the initially shrunk microbubbles changes from 30° to 80°, and slightly decrease with L_0.

3.3.2 Dissolution of entrapped microbubbles

From the above experimental observations, it is clear that the initially entrapped microbubbles will shrink and eventually completely disappear. However, the dynamics of the shrinking microbubbles still remains unknown. One example of microbubble shrinkage is shown in Fig. 3.4a, in which the top and bottom row show the side and bottom view of the confocal microscopy images, respectively. From the side view images, one can see that both height and width of the microbubble gradually decrease with time until the microbubble eventually completely disappears. Moreover, images from both views indicate that one side of the three phase contact line is pinned at the edge of the well

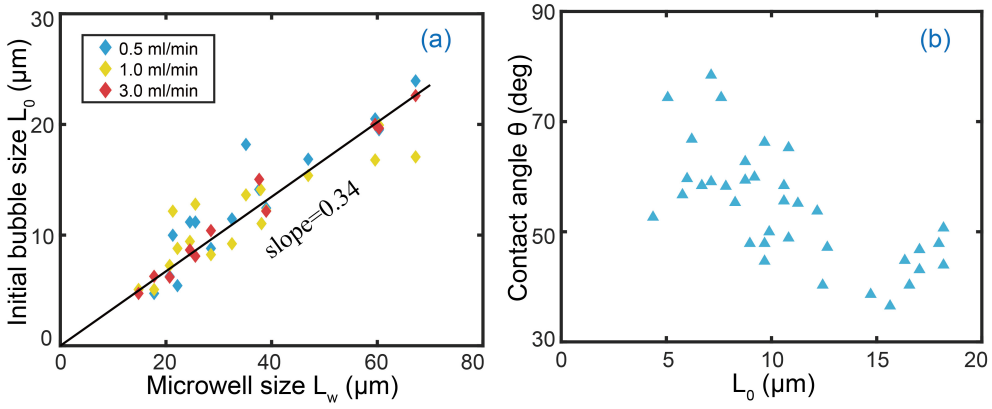

Figure 3.3: (a) Correlation of the lateral size L_0 of the initially shrunk microbubbles and the width L_w of the microwells. The value L_0 approximately linearly increases with L_w. This implies that the larger well contains more entrapped gas. (b) Contact angle θ of the entrapped microbubbles as a function of L_0. The contact angle decreases with increasing L_0.

and the other side keeps receding during the shrinking process. As an example, a schematic diagram of the microbubble shrinkage is shown in Fig. 3.4b. The phenomenon that one side is pinned and the other side is detached is due to the heterogeneity of the pinning site and thus the pinning strength. The reason for such symmetry breaking is that the substrates in the experiments are never perfectly homogeneous. Slight differences in the surface properties are sufficient to lead to pinning or depinning on one side only [110, 111].

To investigate how the contact angle changes during microbubble shrinkage, several individual entrapped microbubbles were tracked in time, using the 3D confocal microscope. As an example we consider here three entrapped microbubbles, as shown in Fig. 3.5. Figures 3.5a-c are the side view images of the shrinking microbubble at different times. All the three microbubbles exhibit similar dissolving behavior, with one side being pinned at the edge of the wall and the other side retracting with time. During the process, one can clearly see that the contact angles of the individual microbubbles remain almost constant, as shown in Fig. 3.5d, which implies that the microbubbles dissolve in the constant contact angle mode.

Under the condition of constant contact angle shrinkage, on a plane sur-

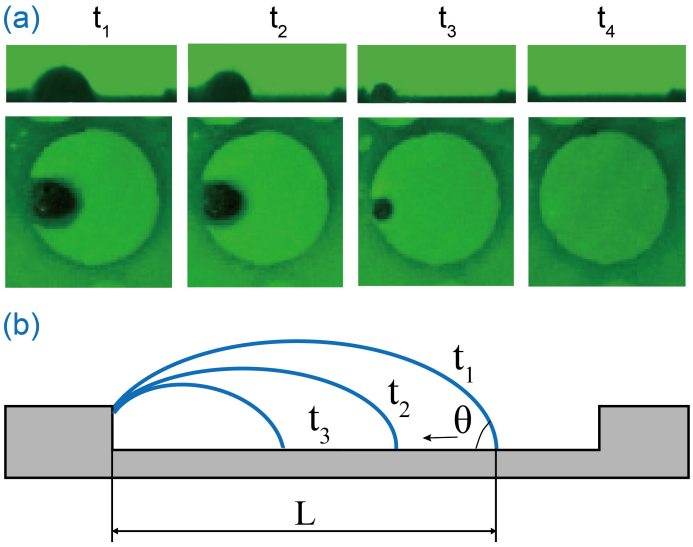

Figure 3.4: The shrinkage process of the entrapped microbubbles, in the CA-mode. (a) The side and bottom views of a shrinking microbubble. One side of the three phase contact line of the microbubbles is pinned to the edge of the microwell. The other side recedes while the microbubble dissolves. (b) Cartoon of the microbubbles dissolving. During microbubble shrinking, it is pinned at one side, and both height and lateral diameter decrease with time.

face spherical-cap-shaped microbubbles dissolve through air diffusion from microbubble to liquid, governed by: [110]

$$L^2(t) = L_0^2 - \kappa(\zeta)t. \tag{3.1}$$

In the equation, κ is the dissolution rate and is given by

$$\kappa = \frac{8Dc_s\zeta}{\rho}\frac{f(\theta)}{3g(\theta)}, \tag{3.2}$$

where D is the diffusion coefficient, c_s is the solubility of air in water, ρ is the gas density in the microbubble, θ again is the contact angle of microbubble from the gas side, ζ the air undersaturation of water defined as ζ=1-c_∞/c_s, and

$$f(\theta) = \frac{\sin\theta}{1+\cos\theta} + 4\int_0^{+\infty} \frac{1+\cosh 2\theta\zeta}{\sin 2\pi\zeta}\tanh((\pi-\theta)\zeta)d\zeta, \tag{3.3}$$

and

$$g(\theta) = \frac{\cos^3\theta - 3\cos\theta + 2}{3\sin^3\theta}. \tag{3.4}$$

For an air-water solution with a certain undersaturation value, the dissolution rate κ only depends on the contact angle θ. Therefore, a constant contact angle leads to constant κ. As a result, L^2 is expected to linearly decrease with t, see Eq. (3.1). To verify the linear dependence, the lateral diameter $L(t)$ of the entrapped microbubbles was first tracked in air equilibrated water, as shown in Fig. 3.6a. The value of $L^2(t)$ is plotted in Fig. 3.6b. Indeed, $L^2(t)$ linearly decreases with time, which is consistent with the constant contact angle mode, and a spherical-cap bubble on a plane surface. Note that this latter assumption is not given, as the bubbles in our experiments are not sitting on a plane surface, but in a microwell, where the diffusive gas flux is partially blocked. Therefore, quantitatively the dissolution rate should be slightly slower than that for a bubble on a plane surface.

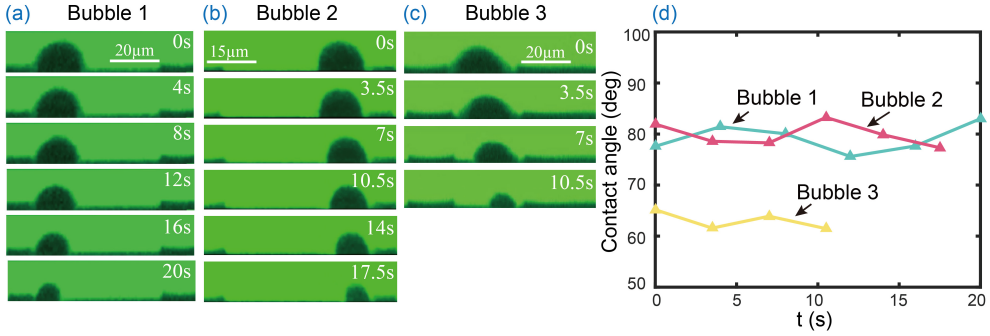

Figure 3.5: (a)-(c) The side view images of an individual dissolving microbubble at different time. The three microbubbles behave the same, with one side of the three phase contact line pinned at the edge of the wall while the other side keeps receding with time. (d) Change of the contact angle of the three microbubbles with time. During shrinkage, the contact angles remain almost constant.

The constant contact angle dissolution mode, as well as the linear dependence of L^2 on t holds for all gas concentrations. To verify this, we conducted further experiment in partially degassed water. The results are shown in Fig. 3.6c and d, showing that L^2 still linearly decreases with time.

We now become more quantitative: From Eq. (3.2), which holds for spherical-cap bubble on a plane surface, one can see how the value of the dissolution rate κ depends on the undersaturation level ζ of the water. This implies that the dissolution time t_{diss} (defined by $L(t)$=0) of the microbubbles also depends on ζ. The value of t_{diss} can be obtained by rewritting Eq. (3.1) as

$$\frac{L^2(t)}{L_0^2} = 1 - \frac{t}{t_{diss}}, \tag{3.5}$$

where

$$t_{diss} = \frac{L_0^2}{\kappa} = \frac{L_0^2 \rho}{8 D c_s \zeta} \frac{3g(\theta)}{f(\theta)}. \tag{3.6}$$

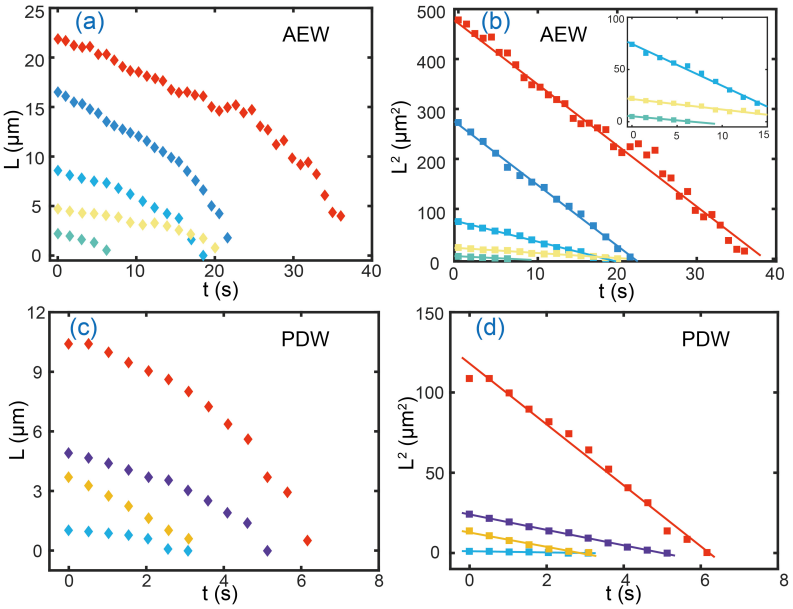

Figure 3.6: Change of the microbubble lateral diameter L (a, c) and its square L^2 (b, d) as a function of time during microbubble shrinkage in air equilibrated water (a, b) and partially degassed water (c, d), respectively. In the both cases, L^2 decreases linearly with time .

We can see that in this purely diffusive regime and for a spherical-cap bubble on a plane surface the dissolution time t_{diss} quadratically depends on the

initial lateral microbubble diameter L_0, and is inversely proportional to the undersaturation. The relative gas concentration in AEW and PDW used in this study was 0.96 and 0.63, respectively. The corresponding undersaturation ζ is 0.04 and 0.37. Two different flow rates Q were applied in the experiment for both AEW and PDW cases. In Fig. 3.7, the dissolution rate κ and the dissolution time t_{diss} are compared for microbubbles with various initial lateral diameter for the two undersaturation levels. The results in Fig. 3.7a show that κ in PDW is higher than that in AEW, which is consistent with Eq. (3.1). It means that the microbubbles dissolve faster in water with a higher ζ. In addition, we observed that κ varies even for the same lateral diameter and slightly increases with increasing L_0. This is believed to be due to different contact angle values even for microbubbles with similar sizes, due to difference in pinning. In Fig. 3.7b, we can see that the measured t_{diss} in AEW is larger than that in PDW, which agrees with Eq. (3.5). From the results shown in Fig. 3.7, we conclude that neither the dissolution rate nor the lifetime is affected by the flow rates.

Moreover, according to Eq. (3.6), the theoretical dissolution time for a sherical-cap-shaped bubble on a plane surface t_{diss} can be obtained with the measured contact angles by taking $D = 2 \times 10^{-9}\mathrm{m}^2/\mathrm{s}$, c_s=0.023 kg/m^3, and ρ=1.169 kg/m^3 [112]. A comparison of the experimental and theoretical results of t_{diss} is shown in Fig. 3.7c. One can see that the experimental value of t_{diss} in both AEW and PDW is obviously larger than that calculated with Eq. (3.6). This means that the actual lifetime of microbubbles is longer than that expected from the diffusion theory for a bubble on a plane surface.

There are three possible factors which can be responsible for the discrepancy: the partial blockage of the gas outflux by the well walls, collective effects of neighbouring microbubbles, and addition partial blockage of diffusion by absorbing dye [111–114]. Since the bubble is not spherical-cap-shaped, sitting on a plane surface, but trapped in a microwell, the presence of the microwell side wall will lead to partial blockage of the diffusive gas outflux. On one hand, the edge of the microwell serves as anchors where the contact line is pinned. At this pinned portion of the microbubble, the side wall of the microwell blocks the diffusive outflux. Compared to microbubbles at flat sample surfaces, the gas cannot escape from the side wall of the microwell. This helps to slow down the bubble dissolution. On the other hand, even for the portion of the detached three phase contact line from the openings of the microwell, the gas still cannot escape freely because the side wall of the microwell and the deepening partially block the gas diffusion. Both geometric effects of the microwell on the diffusive

flux contribute to the increased t_{diss}.
We now roughly estimate how large this diffusive blockage effect can be. We assume that the bubble is partially blocked with the well wall of $h = 1$ μm (the well depth on our sample is $0.8 \sim 1.2$ μm), as depicted in Fig. 3.7d, where the lower part of the bubble is completely blocked by the side wall. The initial lateral diameter L_0, the height H (with the bottom side of the well as reference), and the contact angle θ of the partially blocked bubble are obtained from experiment. The corresponding parameters L_0' and θ' for the unblocked part of the bubble are given as (see Fig. 3.7d)

$$\theta' = \arccos \frac{L_0^2 - 4H^2 - 8Hh}{L_0^2 + 4H^2}, \tag{3.7}$$

$$L_0' = \frac{L_0^2 + 4H^2}{4H} \sin\theta'. \tag{3.8}$$

The mass loss dM/dt of the partially blocked bubble then is [20, 110]

$$dM(L', \theta')/dt = -\frac{\pi}{2} L' D c_s \zeta f(\theta'). \tag{3.9}$$

The mass M of the bubble is

$$M(L, \theta) = \rho \frac{\pi}{8} L^3 g(\theta). \tag{3.10}$$

According to Eq. (3.9) and (3.10), and the geometric relationships in Eq. (3.7) and (3.8), we can numerically determine the time when $M(L, \theta) = 0$ for constant contact angle θ. In this way the theoretical dissolution time t_{diss} in the partially blocked case is acquired, as shown in Fig. 3.7c (open triangles). It is clear from the comparison that the effect of partial blocking is substantial. Note that theoretical dissolution time t_{diss} in the blocked case is slightly larger than the experimentally measured ones.
We expect that the real blockage effect should be smaller than what we have estimated here, because the bubbles are only partially pinned at the wall. In addition, the specific pinning portion along the three-phase contact line varies for different bubbles and changes during the dynamic process. As a result, it is difficult to get a completely quantitative evaluation of the partial blockage effects.
Regarding the effect of the neighbouring microbubbles on the dissolution process, the distance between neighboring is crucial. On our sample the shortest distance between neighboring bubbles is about 16 μm, which for most bubbles

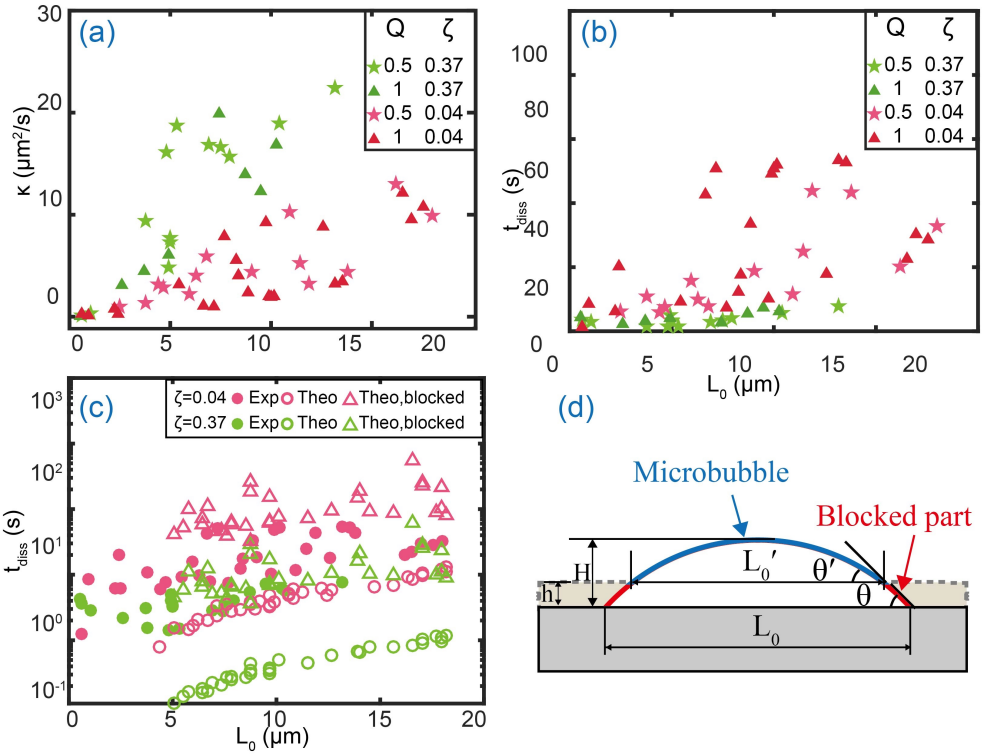

Figure 3.7: Comparison of the dissolution rate κ and dissolution time t_{diss} for microbubbles in AEW and PDW for two different flow rate Q (value given in mL/min). (a) The value of κ in PDW is higher than that in AEW. (b) The dissolution time t_{diss} in AEW is larger than that in PDW. Clearly, the microbubbles dissolve faster in the water with higher undersaturation value, independent of the flow rates. (c) The experimental dissolution time t_{diss} is larger than the theoretical one for a spherical-cap-shaped bubble on a plane surface, both in AEW and PDW. The dissolution of microbubbles in the experiments is delayed, due to the wall blockage effect of the gas diffusion out of the entrapped bubble. This was supported by an quantitative estimation of the dissolution time (Eq. (3.9) and (3.10)) when the bottom part of the bubbles is blocked (data points corresponds to the upper open triangles). (d) The geometry and notation for the microbubble with the bottom part blocked by the side wall of the microwell.

is larger than their diameter, see Fig. 3.7. In one of our recent works [111], we have calculated the effect of neighboring droplets (which have the same diffusive dynamics) on the dissolution time. The closest packaging of droplets there is with a distance of 5 μm, on a footprint diameter of 10 μm. This is much closer than what we have here. Nonetheless, the dissolution time only increases by 60% when increasing the microwell distance from 5 micrometers (where there are collective effects) to 20 μm (hardly any collective effects). This is much less than the above blockage effect.
Finally, we discuss the effect of the addition of dye, which indeed will result in a slight increase of the dissolution time. The reasons are two-fold: (i) The dye as surfactant will slightly lower the surface tension and (ii) more importantly, the dye attachment to the interface will lead to a partial blockage of the diffusion through the interface. These two effects in principle would contribute to the larger measured dissolution time, as compared to the theoretical prediction. However, to minimize these dye effects, we used a relatively low dye concentration of 2 mg/mL. For such low concentrations, the dye effect on the surface tension is minimal: It decreases from 72.1 mJ/m^2 to 71.3 mJ/m^2 with concentration of the dye from 0.1 mg/mL to 20 mg/mL [115]. In summary, it is clear that the partial blockage of the gas outflux through the air-water interface is the main effect for the delayed dissolution, due to geometric constrains by the walls of the well and to some degree also due to partial coverage of the interface by the dye.

3.4 Conclusions

In this study, the temporal evolution of microbubbles at solid-liquid interfaces of immersed structured PS surfaces was systematically investigated. The results clearly show that the microwells on hydrophobic surfaces are able to trap gas and form microbubbles. The microwells were initially fully covered by the entrapped microbubbles that are pinned at the edges of microwells. Then part of three phase contact line detaches from the microwell edges and the microbubbles rapidly shrink to a smaller size. Subsequently, the microbubbles undergo shrinkage in a constant contact angle mode due to gas diffusion into the liquid. Experimental results show that the square of footprint area of the microbubbles decreases linearly with time, which further confirms the constant contact angle dissolution mode. In addition, our results show that a higher understaturation enhances microbubble dissolution, while the flow rates remarkably have no influence on the dynamics of microbubble entrap-

ment and dissolution. We also see that geometric blockage effects due to the microwell lead to reduced dissolution rates as compared to free bubbles on plane surfaces.

In general, we have shown that the position and size of interfacial microbubbles can be controlled. It is clear that the surface microstructures lead to gas entrapment. The amount of the entrapped gas directly depends on the size of the surface structures. In addition, the quantitative studies under various undersaturation and flow rate conditions give a rough estimation on the microbubbles lifetime and stability. We believe this work will lead to a better understanding of the mechanism of interfacial nanobubble formation and provide an effective way to more stable and reproducible interfacial micro- and nanobubbles formation.

Chapter 4

Plasmonic Bubble Nucleation and Growth in Water: The Effect of Dissolved Air[1]

Under continuous laser irradiation, noble metal nanoparticles immersed in water can quickly heat up, leading to the nucleation of so-called plasmonic bubbles. In this work we want to further understand the bubble nucleation and growth mechanism. In particular, we quantitatively study the effect of the amount of the dissolved air on the bubble nucleation and growth dynamics, both for the initial giant bubble, which forms shortly after switching on the laser and which is mainly composed of vapor, and for the final life phase of the bubble, during which it mainly contains air expelled from the water. We found that the bubble nucleation temperature depends on the gas concentration: the higher the gas concentration, the lower the bubble nucleation temperature. Also the long-term diffusion dominated bubble growth is governed by the gas concentration. The radius of the bubbles grows as $R(t) \propto t^{1/3}$ for air equilibrated and for air oversaturated water. In contrast, in partially degassed water, the growth is much slower, since even for the highest temperature we achieve, the water remains under-saturated.

[1]Published as: **Xiaolai Li**, Yuliang Wang, Mikhail E. Zaytsev, Guillaume Lajoinie, Hai Le The, Johan G. Bomer, Jan C. T. Eijkel, Harold J. W. Zandvliet, Xuehua Zhang, and Detlef Lohse, *Plasmonic Bubble Nucleation and Growth in Water: The Effect of Dissolved Air*, J. Phys. Chem. C **123**, 23586-23593 (2019). Experiments and writing are done by Li, supervision by Wang, Zandvliet and Lohse.

4.1 Introduction

When noble nanoparticles immersed in water are irradiated by a continuous wave laser at their resonance frequency, a huge amount of heat is explosively produced. This leads to a rapid temperature increase and hence to the vaporization of the surrounding water, resulting in the formation of microsized bubbles. These bubbles are referred to as plasmonic bubbles [21,22,116]. The plasmonic bubbles are relevant to various applications, such as biomedical diagnosis and cancer therapy [26,28,117], solar energy harvesting [22,118–120], micromanipulation of nano-objects [31,33,121,122] and locally enhanced chemical reactions [21, 34]. To exploit their potential applications, it is of key importance to understand the nucleation mechanism and explore the growth dynamics of these bubbles.

The formation of plasmonic bubbles involves complex physical processes, including optothermal conversion, heat transfer, phase transitions, gas diffusion, and many others [22–25, 116, 123]. In these processes, many factors are relevant, such as particle arrangement [33], laser power [124], liquid type [39], and gas concentration [24,116]. Among these factors, gas concentration plays a crucial role in the formation and growth of plasmonic bubbles, like in the formation of other types of micro/nanoscale surface bubbles [10,99,125]. This has been addressed in several studies [24,116,126], but ignored by many others [127–129]. By investigating the shrinkage dynamics of plasmonic bubbles, Baffou and co-workers found that the plasmonic bubbles could survive for several hundreds of seconds after the irradiation laser was switched off [24]. This is due to the fact that the bubbles are actually not vapor bubbles, but mainly contain gas which was originally dissolved in the liquid [123]. Later, Liu *et al.* generated microbubbles at highly ordered plasmonic nanopillar arrays, and observed a larger growth rate in air-equilibrated water than that in partially degassed water, which underlines the important role that the dissolved gas plays in the bubble formation [116].

Recently, we conducted a systematic study of the plasmonic bubble nucleation mechanism [25] and growth dynamics [123]. We found that plasmonic microbubble nucleation and evolution in water can be divided into four phases: an initial giant vapor bubble (phase 1), oscillating bubbles (phase 2), a vaporization dominated growth phase (phase 3), and finally a gas diffusion dominated growth phase (phase 4) [25, 123]. Dissolved gas governs the bubble dynamics, especially for phase 1 and phase 4. In phase 1, water surrounding the laser irradiated gold nanoparticles becomes superheated, *i.e.*,

reaching a temperature that substantially exceeds the boiling temperature [23, 24, 35, 130–132]. Consequently, vapor bubbles nucleate, grow, and then become microsized bubbles. In partially degassed water, the lower gas concentration leads to less nuclei, and thus to the suppressing the nucleation of bubbles. As a result, the superheat temperature in partially degassed water is higher than in air-equilibrated water and it requires a longer illumination time in partially degassed water before the nucleation of the bubbles sets in. In phase 4, bubbles enter the long-term growth regime. This phase is dominated by the influx of dissolved gas from the surrounding water. Experimental results show that the bubble radius roughly scales as $R(t) \propto t^{1/3}$ in air-equilibrated water, which is distinctly different from the scaling in partially degassed water [123], where the bubbles in the long-term hardly grow at all. For both kinds of behavior, $R(t) \propto t^{1/3}$ for the gaseous case and $R(t) \approx$ const for the strongly degassed case, a theoretical explanation was given [25].
In spite of the above-mentioned studies of the dissolved gas effect on bubble nucleation and growth dynamics, a quantitative understanding and investigation for systematically varying gas saturation is still lacking. In this work, such a systematic investigation is performed at six different relative concentrations c_∞/c_s of dissolved gas, ranging from highly degassed to over-saturated water. Here, c_∞ is the actual gas concentration, and c_s is saturation concentration. This allows us to establish the detailed dependence of the dynamic parameters of bubble formation on the gas concentration. The understanding from this work facilitates the control of plasmonic bubble formation in related applications.

4.2 Methods

Sample Preparation

A fused silica surface patterned with an array of gold nanoparticles was used to produce plasmonic bubbles. A gold layer of approximately 45 nm was first deposited on an amorphous fused-silica wafer by using an ion-beam sputtering system (home-built T′COathy machine, MESA$^+$ NanoLab, Twente University). A bottom anti-reflection coating (BARC) layer (∼186 nm) and a photoresist (PR) layer (∼200 nm) were subsequently coated on the wafer. Periodic nanocolumns with diameters of approximately 110 nm were patterned in the PR layer using displacement Talbot lithography (PhableR 100C, EULITHA) [133]. These periodic PR nanocolumns were subsequently trans-

ferred at wafer level to the underlying BARC layer, forming 110 nm BARC nanocolumns by using nitrogen plasma etching (home-built TEtske machine, NanoLab) at 10 mTorr and 25 W for 8 min. Using these BARC nanocolumns as a mask, the Au layer was subsequently etched by ion beam etching (Oxford i300, Oxford Instruments, United Kingdom) with 5 sccm Ar and 50-55 mA at an inclined angle of 5°. The etching for 9 min resulted in periodic Au nanodots supported on cone-shaped fused-silica features. The remaining BARC was stripped using oxygen plasma for 10 min (TePla 300E, PVA TePla AG, Germany). The fabricated array of Au nanodots was heated to 1100°C in 90 min and subsequently cooled passively to room temperature. During the annealing process, these Au nanodots re-formed into spherical-shaped Au nanoparticles. Fig. 4.1a shows the schematic of a gold nanoparticle sitting on a SiO_2 island on a fused-silica. The energy-selective backscatter (ESB) and scanning electron microscope (SEM) images of the patterned gold nanoparticle sample surface are shown in Fig. 4.1b (left) and Fig. 4.1b (right), respectively.

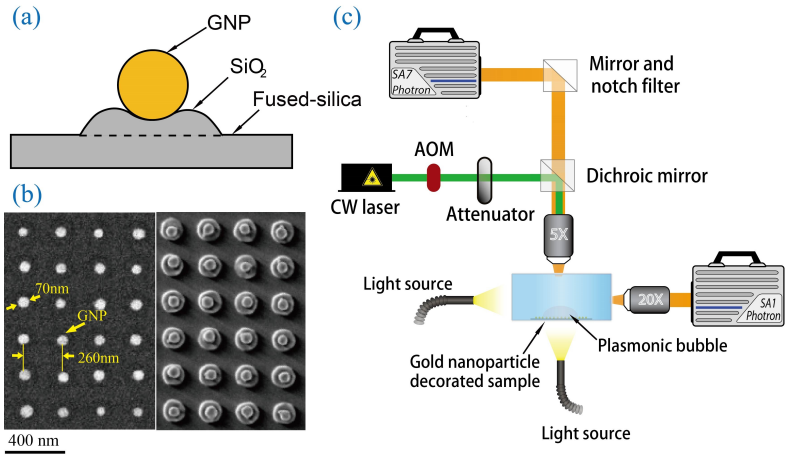

Figure 4.1: (a) Schematic of a gold nanoparticle sitting on a SiO_2 island on a fused-silica substrate, (b) A energy-selective backscatter (left) and scanning electron microscope (right) image of the patterned gold nanoparticle sample surface, (c) Schematic diagram of the optical setup for plasmonic microbubble imaging.

Gas concentration control

During experiments, the nanoparticle decorated sample surface was immersed into deionized (DI) water (Milli-Q Advantage A10 System, Germany). Experiments were separately executed to explore the effect of gas concentration both on the nucleation dynamics of the initial giant bubbles and on the long-term diffusive growth dynamics of the plasmonic bubbles. For the latter, six different gas concentration levels of c_∞/c_s=0.55, 0.65, 0.75, 0.85, 0.96, and 1.20 were used. For the initial giant bubbles, the nucleation dynamics only depends weakly on the gas concentration and therefore we have only considered three different gas concentrations of c_∞/c_s=0.10, 0.80, and 1.20. All experiments were conducted at 25 °C and 1 atmosphere.
The oversaturated water was prepared by keeping the water at 4°C for 12 h and then warming up to the room temperature of 25°C. After that, the measured gas concentration c_∞/c_s was 1.2 (by oxygen meter, Fibox 3 Trace, PreSens). For the air-equilibrated water, a sample bottle containing DI water was kept open in air for 10 hours, the measured gas concentration is 1.0. Similarly, the nearly air-equilibrated water with c_∞/c_s=0.96 was obtained by keeping the water in air for 8 hours. To prepare partially degassed water with different gas concentration values, the water was first degassed for 30 mins in a vacuum chamber, then the concentration of 0.1 was obtained. Subsequently, we kept the bottle of the highly degassed water open in air, with the probe of oxygen meter immersed in the water. The gas concentration in the water was adjusted by varying the air exposure time.

Setup description

The experimental setup for plasmonic microbubble imaging is shown in Fig. 4.1c. The gold nanoparticle decorated sample was placed in a quartz glass cuvette and filled with water. A continuous-wave laser (Cobolt Samba) of 532 nm wavelength with a maximum power of 300 mW was used for sample irradiation. An acousto-optic modulator (Opto-Electronic, AOTFncVIS) was used as a shutter to control the laser irradiation on the sample surface. A pulse/delay generator (BNC model 565) was used to generate two different laser pulses of 400 μs and 4 s in order to study the short-term and the long-term dynamics of microbubbles, respectively. The laser power was controlled by using a half-wave plate and a polarizer and measured by a photodiode power sensor (S130C, ThorLabs). Two high-speed cameras were installed in the setup. One (Photron SA7) was equipped with a 5x long working distance

objective (LMPLFLN, Olympus) and the other (Photron SA1) is equipped with various long working distance objectives: 10× (LMPLFLN, Olympus) and 20× (SLMPLN, Olympus) and operated at various frame rates from 5 kfps up to 540 kfps. The first camera was used for top-view imaging and the second one was for side-view imaging. Two light sources, Olympus ILP-1 and Schott ACE I were applied to provide illumination for the two high-speed cameras. The optical images are processed with a home designed image segmentation algorithm for the optimized extraction of the bubble radius in MATLAB [76, 134, 135].

4.3 Results and Discussion

4.3.1 Giant bubble nucleation

The influence of gas concentration on the nucleation of plasmonic bubbles was investigated with a high speed camera at a frame rate of 540 kfps. Figure 4.2 shows the nucleation and evolution of giant bubbles for three different gas concentration levels of c_∞/c_s = 0.1, 0.8, and 1.2, respectively, at the same laser power P_l =130 mW. The moment the laser is switched on is taken as the origin of time, *i.e.* t = 0 s. One can see that upon laser irradiation the vapor microbubbles nucleate after a delay time τ_d. Subsequently, the bubbles rapidly grow and reach a maximum size in several microseconds (∼5 μs after nucleation), followed by a sudden collapse. As can be seen from Fig. 4.2, the maximum volume V_{max} of the plasmonic bubbles, counter-intuitively, decrease with increasing c_∞/c_s, as discussed in ref. [25]. This can be explained by the increase in delay time τ_d [25]. A longer delay time results in a larger amount of energy dumped into the system (before nucleation) and thus to a larger initial giant bubble.

The dependence of the delay time τ_d on the laser power P_l at each gas concentration was also investigated, as shown in Fig. 4.3a. Due to the limited spatial resolution (∼1 μm) of the optical imaging system and the limited temporal resolution (frame rate 540 kfps) of the high speed camera, the estimated error in the determination of the delay time is about 2 μs. Since the delay time is in the order of a few hundreds of microseconds, the relative error is less than 1%. It is clear that at each gas concentration c_∞/c_s, the delay time decreases with increasing laser power P_l. For a given laser power value, the delay time decreases with an increasing gas concentration in water.

To determine the nucleation temperature for each combination of laser power

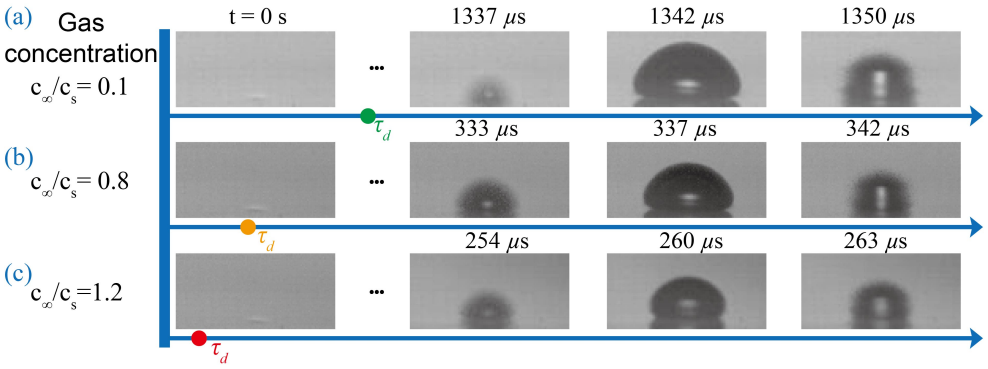

Figure 4.2: The initial giant bubble nucleation at different gas concentration levels of c_∞/c_s=0.1 (a), c_∞/c_s=0.8 (b), and c_∞/c_s=1.2 (c) at the same laser power P_l = 130 mW. The giant bubbles nucleate after a delay τ_d, which decreases with the increasing gas concentration, namely $\tau_d(c_\infty/c_s = 1.2) < \tau_d(c_\infty/c_s = 0.8) < \tau_d(c_\infty/c_s = 0.1)$, while the maximum bubble sizes are smaller at higher gas concentrations.

P_l and gas concentration c_∞/c_s, we have solved a simple heat diffusion model (see ref. [25]). By assuming a spherical geometry and constant thermal properties, from that model the temperature evolution around a nanoparticle can be computed by solving the thermal diffusion equation through a Fourier transformation. The thermal field generated by the nanoparticle array is estimated through a linear superposition of the temperature field generated by the individual nanoparticles within the Gaussian laser beam [25]. The numerical results from this approach were used to fit the measured delay time τ_d with a root-mean-square-minimization method. The fitted curves for the three concentration cases are shown in the double logarithmic plot of Fig. 4.3b. In Fig. 4.3b, the liquid-vapor line (*i.e.*, the boiling temperature curve) and the spinodal line (T_s = 305°C for ambient pressure of 1 atm) were determined by numerically calculating how long it takes to heat the liquid up to 100 °C and 305 °C, respectively, for given laser power P_l. The estimated nucleation temperatures from the fitting process are T_1 = 190°C (c_∞/c_s = 0.1), T_2 = 212°C (c_∞/c_s = 0.8), and T_3 = 245°C (c_∞/c_s = 1.2). Figure 4.3c shows the decreasing nucleation temperature with increasing gas concentration level of c_∞/c_s from 0.1 to 1.2. This quantifies how the gas dissolved in water facilitates

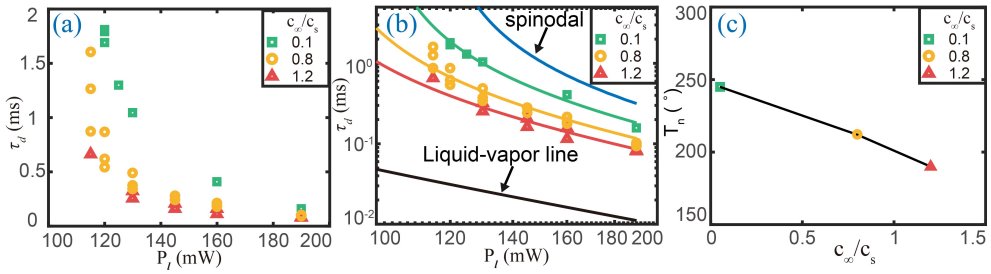

Figure 4.3: The dependence of the delay time τ_d on gas concentration for giant bubble nucleation. (a) Measured delay time τ_d as a function of laser power P_l at different gas concentration. At a given laser power, the higher the gas concentration, the shorter the delay time. (b) Double logarithmic plot of τ_d versus P_l. The measured τ_d is fitted using a heat diffusion model, whose results are displayed with solid lines. The three curves are all located in between the boiling temperature curve and the spinodal curve. (c) The obtained nucleation temperature T_n by fitting τ_d for gas concentration $c_\infty/c_s = 0.1$, 0.8 and 1.2. The higher gas concentration results in a lower nucleation temperature, which indicates that the dissolved gas facilitates the bubble nucleation.

the bubble nucleation.

The dependence of the vapor bubble nucleation on dissolved gas has been pointed out in several other studies. Indeed, the presence of tiny cracks, cavities or pits filled with gas, impurities or aggregations of gas molecules can act as nuclei for bubble nucleation [23, 24, 35, 130–132]. These impurities in water reduce the nucleation temperature, T_n, to a value substantially lower than the liquid spinodal temperature [136–138], and thus enhance the nucleation of bubbles. When the gas concentration is lower, the probability of forming gas nuclei is statistically reduced [55], resulting in a higher T_n. Accordingly, the delay time τ_d will increase with decreasing gas concentration, as demonstrated in Fig. 4.3.

In Fig. 4.4 the maximum bubble size, V_{max}, is plotted versus the total dumped energy $E = P_l\tau_d$, which is defined as the accumulated laser energy in the illumination spot on the substrate from the moment the laser is switched on till the moment of bubble nucleation. Here the laser energy input during the period of bubble growth to its maximum volume is neglected. The reason that this can be done is that, once a giant bubble is formed on the substrate, it iso-

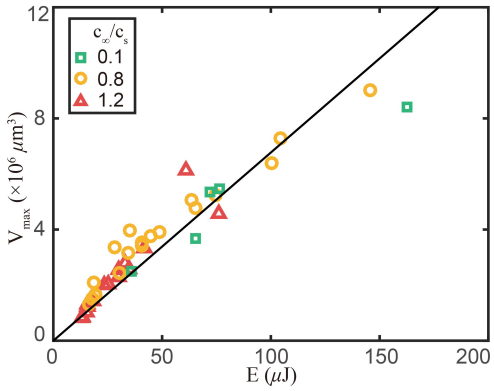

Figure 4.4: Maximum bubble volume V_{max} versus deposited energy $E = \tau_d P_l$ at different gas concentration levels. For all gas concentrations the same linear relation between V_{max} and E is found, regardless of the actual value of τ_d and P_l.

lates the water from the gold nanoparticles, resulting in a strongly suppressed energy transfer to the water. Moreover, it normally only takes about 5 μs for the initial giant bubble to grow to its maximum value right after it appears. This period of time (5 μs) is much smaller compared to the bubble nucleation delay time τ_d of a few hundreds of microseconds to milliseconds. As a result, the contribution of the energy transfer after bubble nucleation is very small and can safely be ignored.
We find an universal linear relation between V_{max} and E for all gas concentrations. This universal linear relation $V_{max} = kE$ reflects that the energy stored in the vicinity of the nuclei determines how many water molecules can be vaporized. The maximum volume of the giant bubble only depends on the amount of energy dumped into the system before nucleation and not on the relative gas concentration. The latter confirms that the giant bubbles mainly consist of vapor.

4.3.2 Long-term growth dynamics

From the above analysis, we have obtained a better understanding of the gas dependence of the bubble nucleation dynamics. After the initial giant bubble collapses, it sequentially enters phase 2 (oscillating bubble phase), and phase 3 (vaporization dominated growth phase), followed by the diffusive growth in

phase 4 [25]. Normally, the final phase begins at $t > 0.5s$. We now focus on this long-term growth dynamics of the bubbles to investigate the role of the dissolved gas also on this terminal growth phase, again by varying the gas concentration levels from undersaturation to oversaturation (now $c_\infty/c_s = 0.55 - 1.2$).

Figure 4.5 shows the long-term growth dynamics of plasmonic bubbles at six concentration levels of $c_\infty/c_s = 1.2$, 0.95, 0.85, 0.75, 0.65, and 0.55. For the oversaturated water ($c_\infty/c_s = 1.2$), the bubble volume V as a function of time is shown for several laser powers in Fig. 4.5a. The bubble volume V increases linearly with time t for all laser powers. The corresponding bubble radius $R(t) \propto V(t)^{1/3}$ is shown in Fig. 4.5b, but now as double-logarithmic plot. After about 0.5 s, R roughly follows an effective $R(t) \sim t^{1/3}$ scaling law. Figures 4.5c and d show the corresponding results in nearly gas equilibrated case with $c_\infty/c_s = 0.95$. The bubble growth has a similar behavior with that in the oversaturated water. The linear relationship of bubble volume versus time (Fig. 4.5c) and the 1/3 effective power scaling law of $R(t)$ (Fig. 4.5d) are both observed again.

The results for partially degassed water are displayed in Fig. 4.5e-l. In the partially degassed water with $c_\infty/c_s = 0.85$ (Fig. 4.5e and f), we again observe a similar bubble growth dynamics as in the overstaturated water and air-equilibrated water, *i.e.* a linear relationship of bubble volume versus time (Fig. 4.5e), and an effective 1/3 power scaling law of $R(t)$ (Fig. 4.5f). However, when the gas concentration in partially degassed water is even lower, the growth dynamics is distinctly different. Figure 4.5g shows the bubble volume versus time in water with $c_\infty/c_s = 0.75$. In this case the volume no longer linearly increases with t. The radius scales as $R(t) \propto t^\alpha$, with an effective exponent $\alpha \approx 0.27$ (Fig. 4.5h). For even lower gas concentraions, namely, $c_\infty/c_s = 0.65$ and 0.55, α reduces to 0.22 and 0.07, respectively.

In plasmonic bubble related applications, the maximal bubble size (volume) is an important parameter. Figures 4.5a, c and e indicate that besides laser power, the growth rate of the bubble volume $\kappa = dV/dt$ is related to the gas concentration. Figure 4.6 shows the growth rate κ as a function of the laser power P_l for the three different gas concentrations (c_∞/c_s=1.2, 0.95 and 0.85). Since V is not proportional to t when c_∞/c_s is lower than 0.75, we only extracted κ for these three cases. We can see that κ increases roughly linearly with the laser power for all gas concentrations, $\kappa = k_{P_l} \cdot P_l$. We find that for higher gas concentrations, the slope k_{P_l} increases, as seen in the inset of Fig. 4.6.

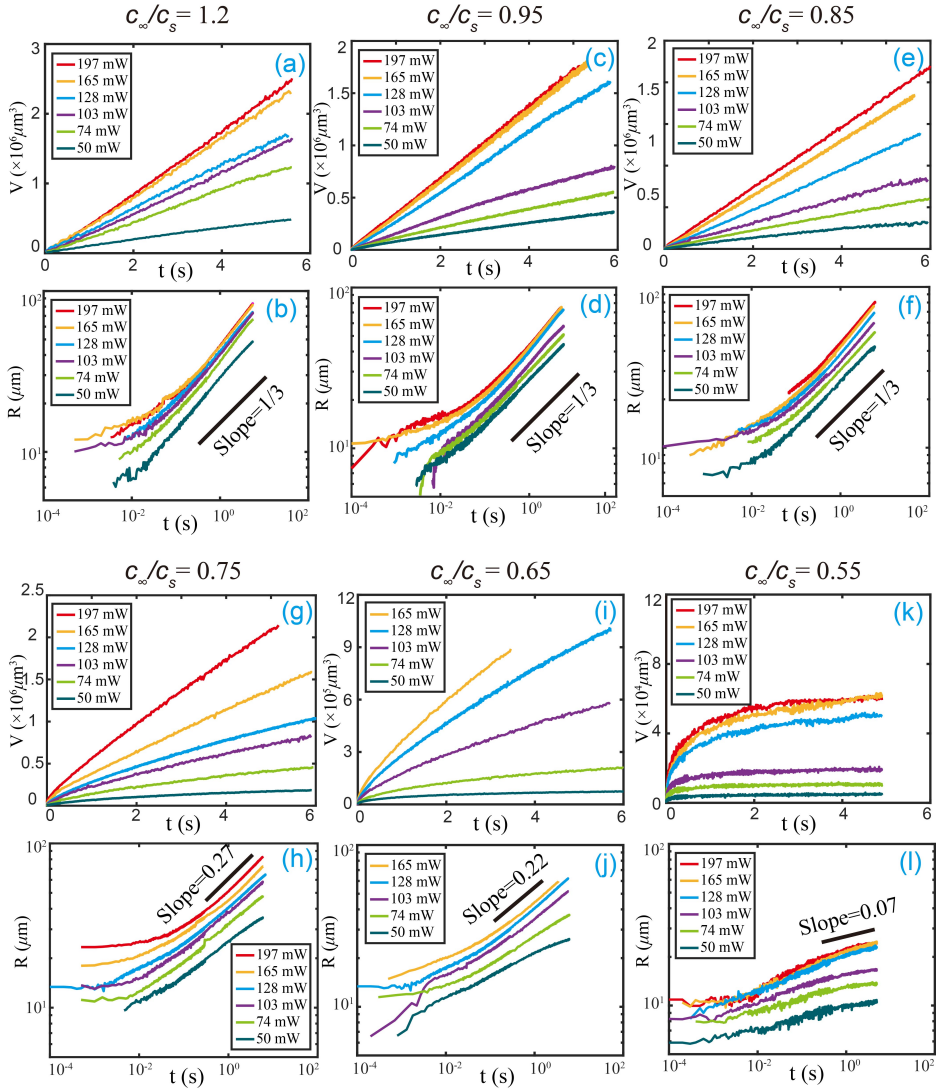

Figure 4.5: Long-term bubble growth dynamics at different gas concentrations and laser powers. c_∞/c_s=1.2 (a, b), c_∞/c_s=0.95 (c, d), c_∞/c_s=0.85 (e, f), c_∞/c_s=0.75 (g, h), c_∞/c_s=0.65 (i, j), c_∞/c_s=0.55 (k, l). Linear plots of bubble volume V (a, c, e, g, i, and k) and double logarithmic plots of bubble radius R (b, d, f, h, j, and l) as functions of time t for gas concentrations c_∞/c_s=1.2, 0.95, 0.85, 0.75, 0.65, and 0.55, respectively. At c_∞/c_s=1.2 (oversaturated water), 0.95 (nearly air-equilibrated water) and 0.85 (partially degassed water), V linearly increases with time for different laser powers. Accordingly, $R(t)$ follows the $t^{1/3}$ scaling law. At lower gas concentrations, the volume no longer linearly increases with t, but exhibits a reduced power law dependence of $R(t) \propto t^\alpha$ with α = 0.27, 0.22, and 0.07 for c_∞/c_s=0.75, 0.65 and 0.55, respectively, as shown in (h, j, l).

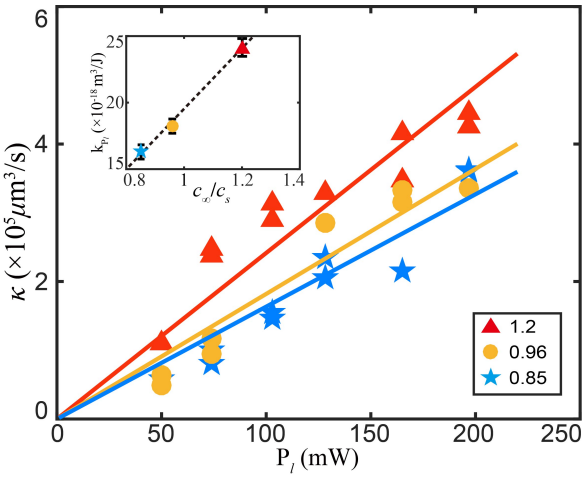

Figure 4.6: Bubble volume growth rates κ in the relation $V = \kappa t$ as function of laser power P_l, for different gas concentrations (from c_∞/c_s=0.85 to 1.2). κ linearly increases with increasing laser powers $\kappa = k_{P_l} P_l$. The prefactor k_{P_l} is found to linearly increase with gas concentration levels c_∞/c_s, $k_{P_l} \propto c_\infty/c_s$, as shown in the inset figure.

The above results quantitatively demonstrate the importance of the dissolved gas on bubble growth. Previously, it was shown that for gas saturation $c_\infty/c_s \approx 1$ the long-term bubble growth (phase 4) is dominated by the influx of gas, which is locally produced around the plasmonic nanoparticles due to heating, [123] as the solubility c_s decreases with increasing temperature. All the expelled gas by oversaturation is taken up by the bubble. For such a production-limited growth process the growth rate is constant, $dV/dt = \kappa$ and consequently $V(t) \propto t$ or $R(t) \propto t^{1/3}$. Considering the heating transfer originated from gold nanoparticles and mass influx, the bubble volume growth rate κ is given by [123]

$$\kappa = -\frac{R_g T}{M_g(P_\infty + \frac{2\sigma}{R})} \frac{c_\infty}{c_s} \frac{dc_s}{dT} \frac{f P_l}{C_w \rho_w} = k_{P_l} \cdot P_l, \tag{4.1}$$

where M_g is the molecular mass of the gas, R_g the gas constant, P_∞ is the ambient pressure and σ the surface tension, ρ_w is water density, and C_w is the specific heat capacity of water, dT is the increase of water temperature. Equation (4.1) shows that for large $R >> 2\sigma/P_\infty$, κ is proportional to both

the relative gas concentration c_∞/c_s and the laser power P_l. Again, these linear dependences ($\kappa \propto P_l$ and $k_{P_l} \propto c_\infty/c_s$) are consistent with the results shown in Fig. 4.6.

The effective power law exponent α in the time dependence $R(t) \propto t^\alpha$ of the bubble radius $R(t)$ is used to further investigate the role of the dissolved gas on the bubble growth dynamics (Fig. 4.7). As shown in Fig. 4.7a, the effective exponent α is approximately 1/3 for all laser powers if c_∞/c_s exceeds 0.85. For lower gas concentrations, $c_\infty/c_s = 0.55 - 0.75$, the effective exponents are smaller than 1/3 and slightly increases with increasing laser power P_l. These results are consistent with our previous findings, where $R(t) \propto t^{1/3}$ and $R(t) \propto t^{0.07}$ for experiments in air equilibrated water and degassed water, respectively. [123] Figure 4.7b shows the effective exponent as a function of c_∞/c_s. As seen before, for given laser power, the exponent increases with increasing gas concentration. The dependence of α on both c_∞/c_s and P_l is summarized in the three-dimensional Fig. 4.7c.

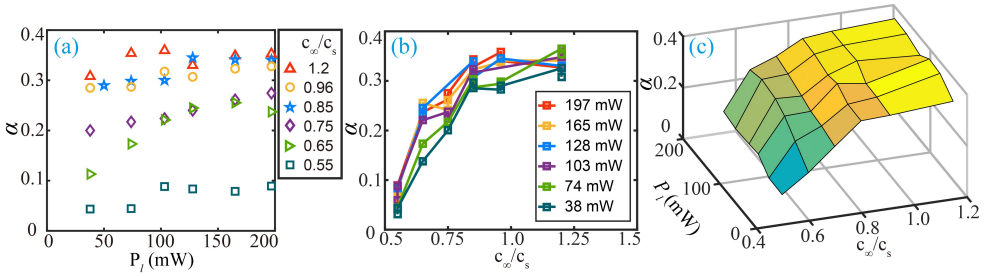

Figure 4.7: Effective power law exponent α in $R(t) \propto t^\alpha$ as function of laser power P_l and gas concentration c_∞/c_s. (a) Effective exponent α as a function of laser power for six different gas concentrations c_∞/c_s. (b) Effective exponent α as a function of gas concentration for different laser powers P_l. (c) 3D plot of α as a function of c_∞/c_s and P_l. Approximately, α monotonously increases with both P_l and c_∞/c_s.

The above results reveal how the dissolved gas controls the long-term bubble growth dynamics. For large gas concentrations there is a constant influx of gas into the bubble, leading to a linear growth of bubble volume. The transfer of heat per unit area to the bubble/water interface becomes so small that there is insufficient energy available to overcome the large latent heat of the vaporization barrier. As a result, gradually the bubble is thermally decoupled

from the nanoparticles. The amount of vapor molecules inside the bubble stabilizes. Thus the bubble growth will be dominated by expelled gas due to the local gas oversaturation.
For large enough initial gas concentration $c_\infty/c_s \geq 0.85$, the effective exponent α in the dependence $R(t) \propto t^\alpha$ saturates at an exponent of 1/3, which is the limit of value for the diffusive growth. In addition, for strongly undersaturated water, the exponent is smaller than 1/3. The latter can easily be understood since the solubility of gas in water decreases with increasing temperature. This means that the water first has to be heated up to a temperature where it becomes supersaturated. Once the water has reached this supersaturated regime, the bubble grows by gas that is expelled from the supersaturated water. With increasing bubble size, the thermal energy transferred per unit area of the bubble/water interface will rapidly decrease. As a result, the amount of over-saturated gas per unit volume near the bubble/water interface will decrease too. At some point the energy transferred to the bubble/water interface becomes so low that no further gas is expelled and the bubble growth terminates.
Notably, at higher laser powers, the effective scaling exponent α for c_∞/c_s=0.65 and 0.75 in Fig. 4.7a becomes approximately equal. The reason is that the relative oversaturation of gas, which dominates the long-term growth of plasmonic bubble, depends on the original amount of dissolved gas (at room temperature) as well as on the temperature (and thus the laser power). If the laser power is larger, the water will be heated up to higher temperatures, leading to a larger gas oversaturation (the solubility of air in water decreases with increasing temperature). As a result, the effect of the initial gas concentration will become weaker at higher laser power. We found a similar behavior for c_∞/c_s=0.85, 0.96, and 1.2. The effective scaling exponent α for these three different but relatively large gas concentrations is very comparable at higher laser powers.

4.4 Conclusions

In summary, the effect of the dissolved gas on the dynamics of plasmonic bubble nucleation in the early phase and in the long-term growth regime has been systematically studied. In the early phase, lower gas concentrations lead to a longer delay times τ_d, larger maximum volume, and higher nucleation temperature, which indicates that the dissolved gas facilitates bubble nucleation. We have found a linear relation between the bubble volume and the total energy.

The prefactor of this linear relation is the same for all gas concentrations reflecting that the bubbles that form in the first stage of the irradiation process are vapor bubbles. Regarding the long-term growth dynamics, we have shown that the growth rate κ of the bubble volume monotonically increases with gas concentration c_∞/c_s and laser power P_l. Moreover, the experimental results show a linear dependence of $\kappa = k_{P_l} P_l$, where k_{P_l} linearly increases with c_∞/c_s. The radius $R(t)$ of the plasmonic bubbles follows the power law dependence $R(t) \propto t^\alpha$. For all laser powers, the effective exponent α for all laser powers is approximately 1/3 when c_∞/c_s is larger than 0.85. However, for lower c_∞/c_s values, the effective exponent is smaller than 1/3 and monotonously decreases with decreasing P_l and c_∞/c_s. For strongly degassed water the exponent α is smaller than 1/3 because the water first has to be heated up to a temperature where it becomes super-saturated and gas can be expelled.

Chapter 5

Plasmonic microbubble dynamics in binary liquids[1]

The growth of surface plasmonic microbubbles in binary water-ethanol solutions is experimentally studied. The microbubbles are generated by illuminating a gold nanoparticle array with a continuous wave laser. Plasmonic bubbles exhibit ethanol concentration dependent behaviors. For small ethanol concentration $f_e \lesssim 67.5\%$, bubbles do not exist at the solid-liquid interface. For large $f_e \gtrsim 80\%$, the bubbles behave as in pure ethanol. Only in an intermediate window $67.5\% \lesssim f_e \lesssim 80\%$, we find sessile plasmonic bubbles with a highly non-trivial temporal evolution, in which as function of time three phases can be discerned: (1) In the first phase the microbubbles grow, while wiggling, (2) as soon as the wiggling stops the microbubbles enter the second phase in which they suddenly shrink, followed by (3) a steady reentrant growth phase. Our experiments reveal that the sudden shrinkage of the microbubbles in the second regime is caused by a depinning event of the three-phase contact line. We systematically varied the ethanol concentration, the laser power, and the laser spot size to unravel water recondensation as the underlying mechanism of the sudden bubble shrinkage in phase (2).

[1]Published as: **Xiaolai Li**, Yuliang Wang, Binglin Zeng, Marvin Detert, Andrea Prosperetti, Harold J. W. Zandvliet, and Detlef Lohse, *Plasmonic microbubble dynamics in binary liquids*, : J. Phys. Chem. Lett. **11**, 8631-8637 (2020). Experiments and writing are done by Li, supervision by Wang, Zandvliet and Lohse.

5.1 Introduction

Plasmonic microbubbles formed around metal nanoparticles immersed in liquid and irradiated by a resonant light source have numerous applications ranging from biomedical diagnosis and cancer therapy [26, 28–30], micromanipulation of micro/nano-objects [31–33], to locally enhanced chemical reactions [21,34]. A proper understanding of the plasmonic microbubble dynamics is crucial for the optimal usage of these bubbles in the aforementioned applications.

In a previous study, we have shown that plasmonic microbubbles in pure (mono-component) liquids undergo four different phases: the initial giant vapor bubble (phase I), the oscillating bubble (phase II), the water vaporization dominated growth (phase III), and the air diffusion dominated growth (phase IV) [25]. The bubble dynamics in these different phases depends on several factors, such as particle arrangement [33], laser power, gas concentration [25, 123, 139], and types of liquid [39, 140]. The nucleation of a giant bubble is initiated by locally heating the liquid around the plasmonic particle up to the spinodal temperature [25]. The heating process is limited by thermal diffusion and can theoretically be well described [35,37,38]. Moreover, the dissolved gas plays a major role in bubble nucleation: an increase of the relative gas concentration leads to a lower bubble nucleation temperature [25,139]. The radius of the bubble in the air diffusion dominated phase IV is $R(t) \propto t^{1/3}$ for air equilibrated or air-oversaturated water [123,139]. Furthermore, several studies on the shrinkage of bubbles have revealed that the shrinkage depends on the illumination history of the bubble as well as the gas concentration level of the liquid [24, 141].

Most of these studies were conducted in water or other pure liquids [140], such as n-alkanes [39]. However, it is known that many plasmonic assisted processes also take place in binary liquids [34]. However, the dynamics of plasmonic bubbles in binary liquids has not yet been investigated in detail. Only in a recent study, we started to investigate the formation of the initial giant plasmonic bubbles in binary liquids [40]. It was shown that the dynamics of bubble nucleation depends on the exact composition of the binary liquid, which could be rationalized based on the constituents of the binary liquid exhibiting different physicochemical properties, such as boiling point and latent heat. In the aforementioned study the focus was only on phase I of the plasmonic bubble formation process, namely, bubble nucleation. A thorough and complete understanding of the full long-term growth dynamics of plasmonic

bubbles in binary liquids is still lacking. In this study, we investigate the growth dynamics of plasmonic bubbles in ethanol/water mixtures over a large range of parameters and over the full bubble lifetime cycle.

5.2 Methods and Materials

The preparation of sample with gold nanoparticle, and the experimental setup for plasmonic microbubbles imaging are shown in Fig. 4.1b and c in Chapter 4.2. During experiments, the nanoparticle decorated sample surface was immersed into binary liquids of ethanol (Sigma-Aldrich; $\geq$ 99.8%) and deionized (DI) water (Milli-Q Advantage A10 System, Germany). The ethanol and water were kept open in air for 8 hours to make them air saturated. After that, they were mixed to prepare binary liquids with ethanol ratios of 20%, 40%, 60%, 65%, 67.5% - 80% with a step of 2.5%, 85%, and 90%. The obtained binary liquids were then immediately transferred into a sealed cuvette for experiments. Since the air solubility in ethanol is much higher than that in water, the prepared binary liquids must be air saturated as well.

5.3 Results and Discussion

We first report the plasmonic bubble behavior as a function of the ethanol concentration f_e, see Fig. 5.1. First, in binary liquids with ethanol concentrations $0 < f_e \lesssim 67.5\%$ (weight), the bubbles are unstable and not pinned at the substrate. As an example, in Fig. 5.1a (left column) we show the bubble dynamics for an ethanol concentration of 40%. In this regime, after nucleation, the bubble detaches from the substrate. Subsequently, a new bubble is generated and then also detaches.
Next, at ethanol concentrations $67.5\% \lesssim f_e \lesssim 80\%$, we find that the plasmonic bubble does not detach from the substrate. As an example for this regime, the dynamics for $f_e = 70\%$ is shown in Fig. 5.1a (right column). Instead, after an initial growth phase, the plasmonic bubble starts to wiggle in this regime, with gradually increasing radius R (Fig. 5.1b (I)), considerably varying contact angle θ (Fig. 5.1b (II)) and horizontal center position X_c (Fig. 5.1b (III)). During the first few seconds after nucleation, the radius, contact angle and horizontal center position exhibit an erratic behavior. At $t = 4.07$ s after bubble nucleation at $t = 0$ s, the bubble abruptly stops wiggling and simultaneously starts to shrink for a short time. Afterwards, the bubble continues to steadily grow without exhibiting any wiggling. The abrupt stop of

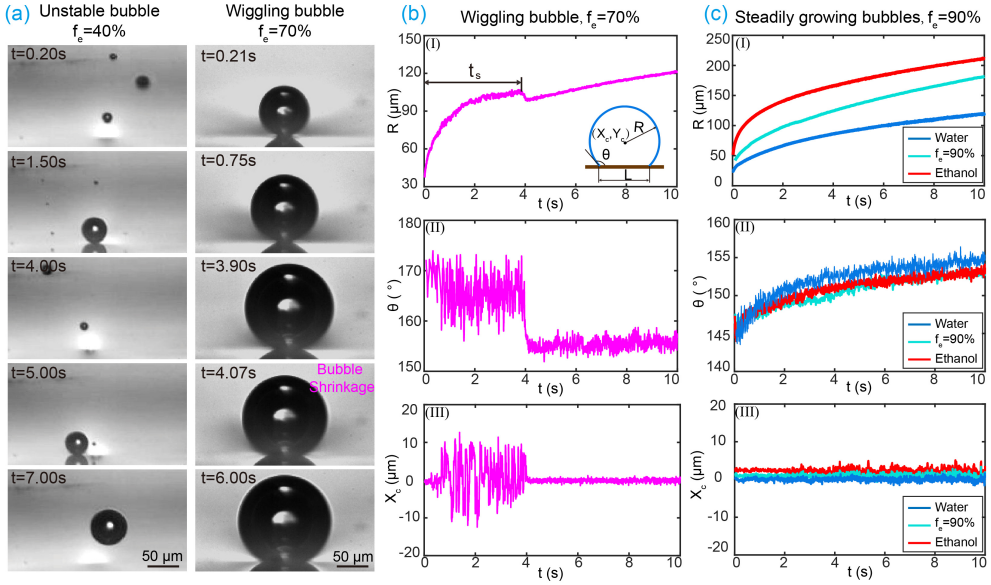

Figure 5.1: (a) Dynamics of plasmonic bubble growth in ethanol-water mixtures with ethanol concentrations of $f_e = 40\%$ (left) and $f_e = 70\%$ (right). In the binary liquid with $f_e = 40\%$, the bubble detaches from the substrate after nucleation, whereas in the binary liquid with $f_e = 70\%$, the bubble remains pinned on the substrate and gradually grows. A sudden shrinkage is observed at time $t_s = 4.07$ s. (b) The radius $R(t)$ (I), contact angle $\theta(t)$ (II), and horizontal center position $X_c(t)$ (III) of the bubble in the binary liquid with $f_e = 70\%$. The inset in (I) shows a sketch, which defines the radius R, the contact angle θ, the horizontal center position X_c, and the footprint diameter L of the bubbles. (c) $R(t)$, $\theta(t)$ and $X_c(t)$ for a bubble in a binary mixture with $f_e = 90\%$, compared to the cases for pure water and pure ethanol. The laser power is $P_l = 100$ mW in all cases of Fig. 5.1a, b, c.

wiggling and the simultaneous starting sudden shrinkage always occur in the regime $67.5\% \lesssim f_e \lesssim 80\%$. We define the moment when this occurs as time of shrinkage t_s.

Finally, when the ethanol concentration f_e of the binary liquids is higher than 80%, we observed stable bubble growth, like in pure water and pure ethanol. Figure 5.1c shows the bubble dynamics in pure water, in pure ethanol and in a binary liquid with $f_e = 90\%$. The laser power P_l was maintained at 100 mW for these three measurements. In these three cases, the bubbles grow monotonously, with gradually increasing R (Fig. 5.1c (I)). No visible intermediate shrinkage and wiggling (Fig. 5.1c (II) and (III)) were observed. Moreover, the radii of the bubbles increase with increasing ethanol concentration. As known from ref. [123] , for air saturated water, the observed long-term growth is dominated by gas-diffusion. However, for the binary liquids in the regime of $f_e \gtrsim 80\%$, bubble growth is dominated by the vaporization. Since the gas solubility in ethanol increases with temperature, the gas expelled from the liquid evaporation can be dissolved into liquids again, which has been shown in a recent study in n-alkane [39].

The above results demonstrate that the ethanol concentration in water-ethanol mixtures plays a pivotal role in the bubble growth. Our interpretation of the observed phenomenon is as follows: in binary liquids with small ethanol ratios $f_e \lesssim 67.5\%$, the detachment of bubbles from the substrate is caused by solutal Marangoni flow [142]. Because ethanol has a lower boiling temperature than water, at the hot substrate it evaporates much faster than water, leading to an ethanol depleted region near the three-phase contact line (triple-line) of the bubbles. The liquid at the top of the bubble is ethanol rich and thus has a smaller surface tension than the ethanol depleted region at the bottom of the bubble, resulting in a downward Marangoni flow. This solutal Marangoni flow pushes the bubble upwards, similarly to what has been observed for a jumping droplet in an ethanol-water concentration gradient [143]. As a result, the bubble detaches when the Marangoni flow is strong enough to overcome the pinning of the bubble at the surface.

The proposed mechanism for bubble detachment can be quantitatively validated. Here we consider an unstable bubble in binary liquids with an ethanol concentration $f_e \approx 40\% - 50\%$ as an example. The surface tension difference $\triangle\sigma$ between the bubble top ($f_e \approx 40\% - 50\%$) and bubble bottom (providing $f_e = 0\% - 20\%$) is $\triangle\sigma \approx 20 - 40$ mN/m. For a bubble with a radius $R \approx 50$ μm, the magnitude of the upward Marangoni force is $F_M \approx \triangle\sigma R = 1 \times 10^{-6} - 2 \times 10^{-6}$N. The Marangoni force competes with

the vertical capillary force F_p. Since the measured contact angle of water $\alpha = 29.1°$ (Fig. 5.9a in the Appendix) on our substrate is in the same ballpark as that on a smooth glass surface ($\alpha = 24°$) [144] , the influence of the gold nanoparticles on the pinning/capillary force of the substrate is very limited. As a result, it is reasonable to estimate the vertical capillary force by $F_p \approx \sigma\pi L sin\alpha \approx 1.4 \times 10^{-6}$ N, assuming that the substrate is homogeneous [145, 146]. In this expression, the surface tension $\sigma = 50$ mN/m, the medium value of measured contact angle (gas side) $\theta = 160°$, and the perimeter of the three-phase contact line $\pi L = 85$ μm.

Notably, the surface tension of the ethanol-water mixtures changes rapidly for small ethanol fractions but remains almost constant for large ethanol fractions [147, 148] (see Fig. 5.6 in the Appendix). This feature explains the observed peculiar behavior: For pure water, the bubble remains pinned because there is no downward solutal Marangoni flow, but an upward thermal Marangoni flow. For low ethanol concentration $f_e \lesssim 67.5\%$, due to the strong dependence of the surface tension on f_e in this regime, a large gradient in surface tension can be created and the resulting Marangoni flow is strong enough to depin the bubbles. With increasing ethanol fraction, the surface tension gradient across the bubble and thereby the Marangoni flow become weaker until finally, at $f_e \approx 67.5\%$, it is unable to overcome the pinning. Therefore, for that ethanol concentration a transition from detaching bubbles to pinned bubbles with stable growth takes place.

However, this mechanism still does not explain the observed wiggling and sudden shrinkage of the stable bubbles in the regime $67.5\% \lesssim f_e \lesssim 80\%$. In order to find out the physical mechanism for the sudden bubble shrinkage, from the bottom view we tracked the changes of the triple-line of a bubble during the growth. Figure 5.2a shows the sequential side view images (first row) and bottom view images (second row) of a bubble in a binary liquid with $f_e = 70\%$. The bubble shrinks in Fig. 5.2a (IV). In the bottom view images, a dry region (the light grey center area) can be observed within the triple-line. The dry area becomes circular and increases after the sudden shrinkage (IV→V). Figure 5.2b shows the profile of the triple-line as extracted from the bottom view as well as the spot profile of the laser.

It is found that the triple-line is first pinned at the edge of the laser spot (the first column of Fig. 5.2a (I)), and then partially depins (Fig. 5.2a (II) and (III)). This explains the wiggling behavior of the bubble shown in Fig. 5.1b. When the contact line depins completely from the laser spot region (Fig. 5.2b (IV)), the bubble shrinks. Afterwards, the triple-line remains circular and

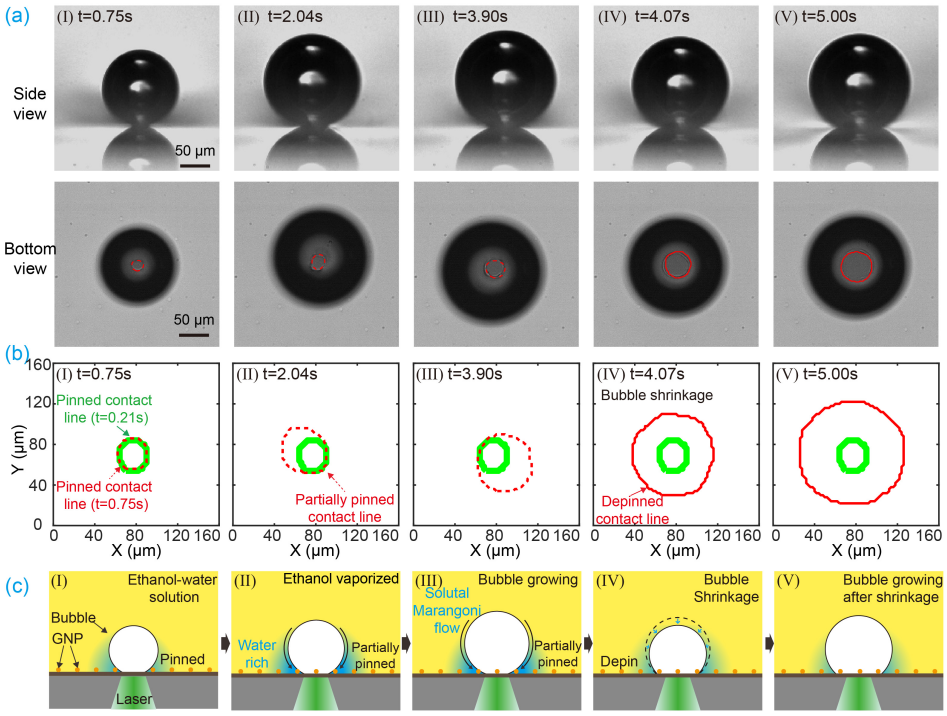

Figure 5.2: Dynamics of the bubble shrinkage. (a) Sequential side and bottom view images of a stable bubble in binary liquids with $f_e = 70\%$. The bubble shrinkage occurs in Fig. 5.2a (IV). (b) The three-phase contact line of bubbles extracted from the bottom view images of Fig. 5.2a. The three-phase contact line is initially pinned, and later partially pinned, at the edge of the laser spot (green line). At the moment t_s of sudden shrinkage at IV, the bubble completely depins. After that, the contact area remains circular with increasing radius. (c) Schematics of bubble growth and shrinkage in a binary liquid.

gradually expands, as shown in Fig. 5.2b (V).

The whole process of bubble growth and shrinkage is schematically shown in Fig. 5.2c. In the early stage of bubble growth, the evaporation of the more volatile ethanol in the binary liquids governs the bubble growth. As a result, the water concentration around the three-phase contact line, of which the size is defined by the laser spot, is relatively higher than the bulk binary liquid. At the triple line, the rapidly increasing bubble volume tends to expand the bubble and thus moves the triple line outwards. At the same time, the higher water concentration around the triple-line (due to the ethanol evaporation) leads to a locally increased surface tension, resulting in an increased receding contact angle [149, 150]. This helps to make the triple line stay pinned. The two effects compete. When the increased surface tension dominates, the triple-line remains pinned. Because of the continuous evaporation of the surrounding liquids, the bubble keeps growing. Finally, the contact angle (liquid side) reaches its receding value and the contact line begins to depin. During this process, the contact line is first partially depinned. Finally, once the water around the laser spot region is completely evaporated, complete depinning takes place, exhibiting a rapid decrease of the contact angle (gas side).

After depinning of the three-phase contact line, the region of the laser spot on the sample substrate is isolated by the bubble from the liquid. Owing to this effect, the light-vapor conversion efficiency significantly reduces and part of the vapor inside the bubble condenses, resulting in a sudden shrinkage of the bubble (Fig. 5.1b (I)). A numerical calculation (Fig. 5.5 in the Appendix) shows that the sample substrate remains non-isothermal in the vicinity of the triple-line when the rapid shrinkage takes place. This means that once the bubble depins, the temperature will drop at the triple-line, resulting in vapor condensation and hence rapid bubble shrinkage. The phenomenon resembles similar jumps in the contact angle occurring for evaporating [151–155] or dissolving binary droplets [156]. After the shrinkage, the bubble enters a steady growth phase again, but now with a lower optothermal conversion efficiency, during which there is no visible shrinkage happening again.

Note that the bubble shrinkage due to the pinning effect only appears in the binary liquids with intermediate ethanol ratios $67.5\% \lesssim f_e \lesssim 80\%$. In general, considering that the pinning force depends on the wettability and the roughness of the surface, the three-phase contact line motion must be expected to move in the 'stick-slip' mode [10, 157–160], made up of one or 'more' stick phases, in which the contact line is pinned. However, in contrast to this expectation, the bubble growth and the contact angle in pure ethanol and pure

water seem to exhibit monotonous growth in our experiments, as seen in Fig. 5.1c. We interpret this finding that for the bubbles in the pure liquids, the pinning effect is only minor and not visible, and the 'stick' phase duration is so short that with our temporal resolution of 1000 fps, it is invisible in the measured dynamical process.

We now further verify the mechanism of bubble shrinkage by varying the laser power P_l and the laser spot size. Figure 5.3a shows the bubble radius versus time at different laser powers for 5× and 10× objectives for laser focusing implying two different laser spot sizes (See Fig. 5.7a and b for reproducible results of $R(t)$ in the Appendix). In Fig. 5.3b the delay time t_s is plotted versus the laser power. For a fixed laser power, the delay time of the 5× objective is substantially longer than that of the 10× objective due to the weaker focusing of the laser beam, resulting in a larger laser spot and lower power density.

The differences in the observed start moment of shrinkage t_s can be understood by capturing the dynamics of the three-phase contact lines for the 5× and 10× objectives, see Fig. 5.3c and 5.3d (see also Fig. 5.8 for contact line L as a function of radius R in the Appendix). After a slight monotonous increase of the footprint diameter of the bubble, it exhibits a sudden jump and eventually gradually increases again. The sudden jump in the footprint diameter coincides with the depinning and shrinkage of the bubble. For the 5× and 10× objectives the jump in the footprint diameter occurs at about 50 μm and 30 μm, respectively. These values agree well with the laser spot diameters $D_l = 46\ \mu m$ and 27 μm for the 5× and 10× objectives, respectively, as shown in the insets of Fig. 5.3c and 5.3d. This also confirms that the triple-lines are initially pinned by the laser spot and shrinkage occurs because of complete depinning. The laser spot size increases with increasing laser power. As a result, the heated region and therefore the pinning radius increases. Thus, the delay period is longer for higher laser powers as more liquid needs to be evaporated to exceed the pinned region.

Finally, we have investigated the dependence of the bubble shrinkage dynamics on the ethanol concentration. As shown in Fig. 5.4a, the bubble shrinkage is observed for ethanol concentrations varying from 70% to 80% (See Fig. 5.7c and d of the Appendix for the reproducible results with different f_e at laser powers of 60 mW and 100 mW, demonstrating that this behavior is robust and reproducible.). Figure 5.4b shows the footprint diameter versus time. As we have kept the laser power and laser spot size constant, the footprint diameter at which the sudden shrinkage occurs is almost the same for all ethanol

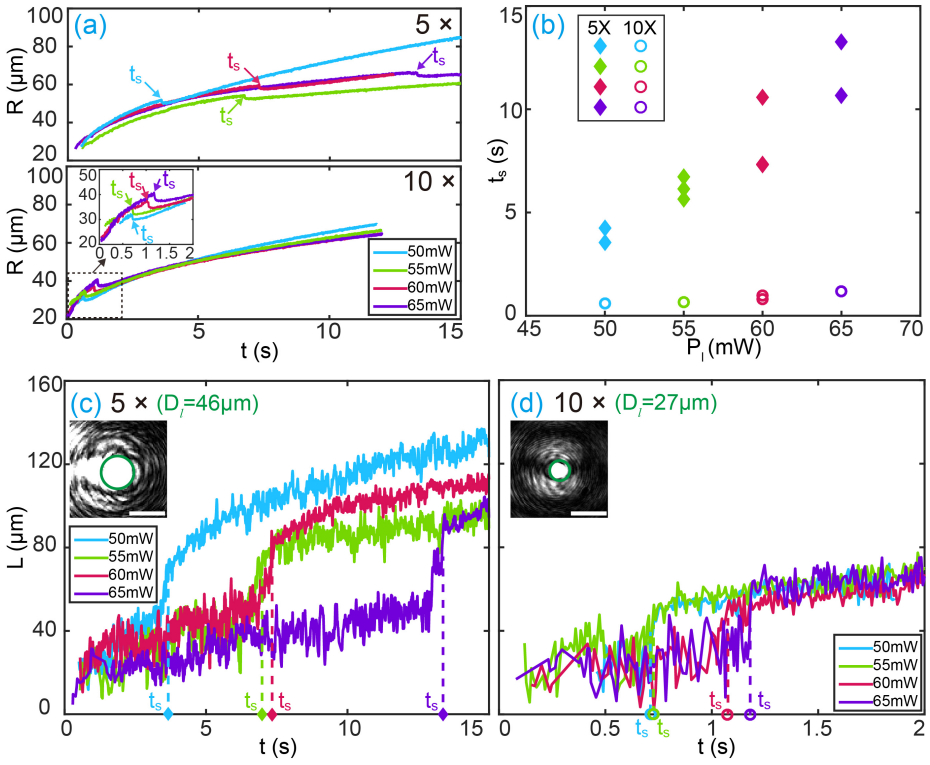

Figure 5.3: Dependence of the bubble shrinkage dynamics on laser power P_l and laser spot size D_l at $f_e = 70\%$. (a) Bubble dynamics for different laser powers P_l at 5× and 10× objectives for laser focusing. (b) Delay time, t_s, as function of laser power. (c, d) Footprint diameter of the bubble versus time for 5× (c) and 10× (d) objectives. The insets show the laser spots. Scale bars: 50 μm.

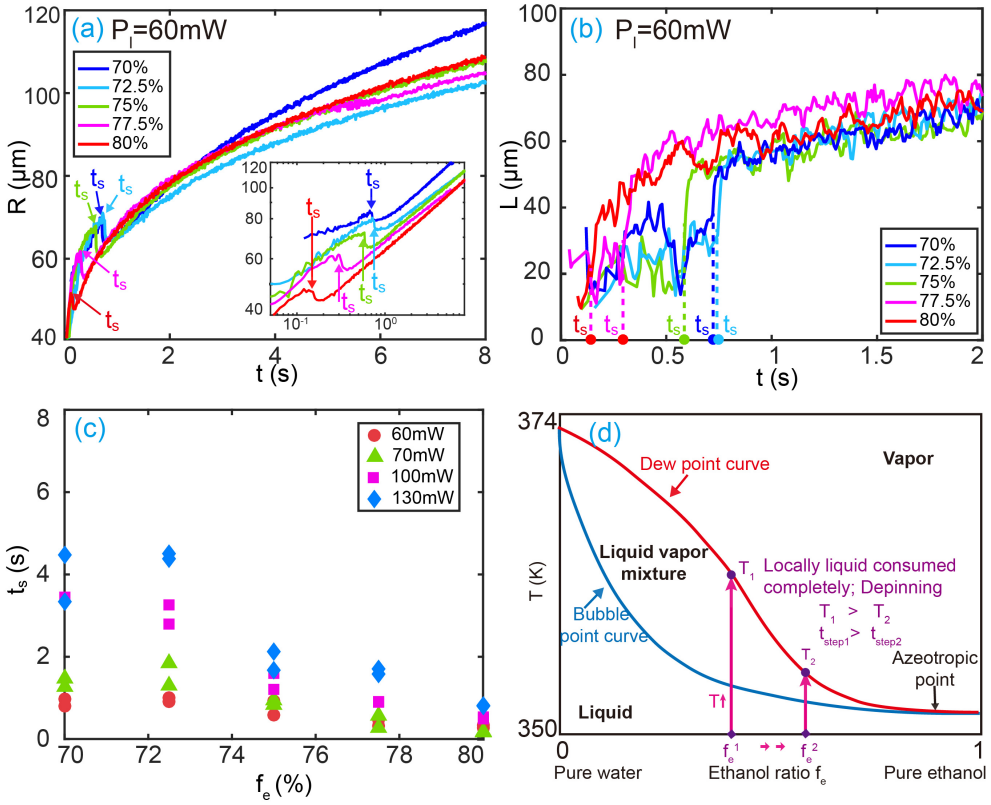

Figure 5.4: Bubble shrinkage dynamics for various ethanol concentrations in the stable bubble regime $67.5\% \lesssim f_e \lesssim 80\%$. (a) Radius $R(t)$ and (b) footprint width $L(t)$ at a laser power of 60 mW. (c) The delay time t_s of bubble shrinkage versus ethanol ratio f_e for laser powers of 60 mW, 70 mW, 100 mW, and 130 mW. (d) Schematic diagram of the bubble point and dew point of ethanol-water mixtures, at ambient pressure.

concentrations. Interestingly, the time t_s of shrinkage steadily decreases with increasing ethanol concentrations (Fig. 5.4c).
The decrease of t_s with increasing ethanol concentration is attributed to the fact that the dew point of the ethanol-water mixture decreases with increasing ethanol concentration, see Fig. 5.4d [161, 162]. From the phase diagram it is immediately clear that at a higher ethanol concentration the ethanol can be evaporated at lower temperatures. Since the laser power and laser spot size are kept constant in this series of experiments, we can safely assume that the heating efficiency remains constant. Therefore, less energy and thus less time is required to evaporate ethanol for a binary liquid with a higher ethanol concentration as compared to a binary liquid with a lower ethanol concentration. The phase diagram also shows that the water/ethanol mixture becomes azeotropic at ethanol concentration higher than 90%, implying that the binary liquid starts to behave as a pure liquid. This perfectly agrees with our experimental findings shown in Fig. 5.1c, as beyond $f_e \approx 90\%$ the plasmonic bubble behaves as in pure ethanol.

5.4 Conclusions

In summary, we have shown that the growth dynamics of plasmonic microbubbles in water-ethanol binary liquids strongly depends on the ethanol concentration. At ethanol concentrations below 67.5% bubbles nucleate and subsequently detach from the substrate due to the downward Marangoni flow. For ethanol concentrations in the range from 67.5% to 80%, the bubbles first wiggle. A sudden bubble shrinkage takes place after a delay time t_s, originating from the complete depinning of the wiggling bubble from the laser spot area on the sample surfaces. Prior to that event the bubble was pinned or partially pinned on the laser spot. When the liquid around the pinned region is completely evaporated, the instantaneous expansion of the three-phase contact line as well as the sudden shrinkage takes place. Finally, when $f_e \gtrsim 80\%$, the binary solutions become azeotropic, leading to a similar behavior as in pure liquids, and bubbles steadily grow. The knowledge of the sensitive dependence of the plasmonic bubble dynamics on the liquid compositions obtained in this paper may help in exploiting the relevant applications of these bubbles in multiple-component liquids. E.g., when a good local mixing of the binary liquids is preferable, operating in the first regime $f_e \lesssim 67.5\%$, in which the bubble is wiggling, may be preferable. Having understood features is also a prerequisite to exploit them in optimizing the energy conversion efficiency of

plasmonic bubble generation.

5.5 Appendix

5.5.1 Temperature field of a silica substrate with a gold nanoparticle array

A numerical calculation was performed to study the effect of the heat conductivity of the substrate (fused silica: 1.4 - 1.5 W/m · K for 293K-373K) on the temperature field in the vicinity of the three-phase contact line (triple-line) of the bubbles. Details of the method can be found in our recent publication [25]. Using this method, the spatial-temporal evolution of the substrate temperature can be obtained. Since the surrounding fluid (either vapor or water) has an influence on the temperature field of the substrate, we have considered two critical cases. In case 1 the surrounding fluid is vapor, whereas in case 2 the surrounding fluid is water. The temperature fields after 10s are shown in Fig. 5.5a and 5.5b, respectively. In both cases there is a substantial temperature gradient at the location of the laser spot. This means that the substrate is not isothermal during the first 10 s. Consequently, once the bubble depins, the temperature will drop at its triple-line, resulting in vapor condensation and hence shrinkage of the bubble.

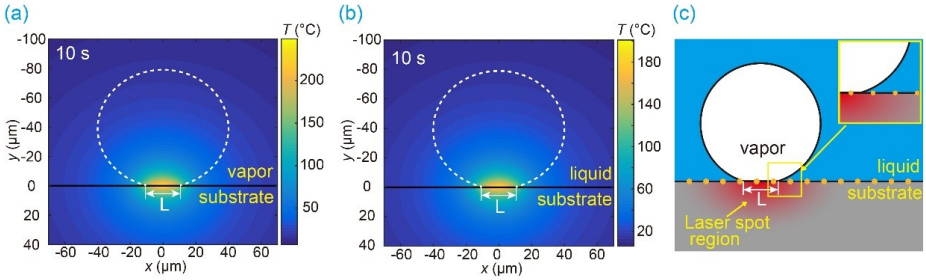

Figure 5.5: Numerical calculated temperature field of the substrate exposed to vapor (a) and immersed in liquid (b) under continuous laser irradiation for 10s. (c) Schematics of the temperature field.

In the actual experiments, obviously the substrate was neither completely immersed in water, nor fully exposed to vapor. As shown in Fig. 5.5c, the substrate within the triple-line region is in contact with the vapor, whereas the rest of the substrate is in contact with water. Due to the large difference in the heat conductivity of vapor and water, the temperature gradient of the substrate around the triple-line is even more pronounced than shown in Fig. 5.5a and 5.5b.

5.5.2 Surface tension of ethanol and water mixtures

Figure 5.6 shows the surface tensions of the ethanol-water binary liquid with ethanol weight ratio fe from 0 to 1 at 20 °C, at 50 °C, and at boiling temperature (which depends on f_e). For each of the three curves, the surface tension σ of the binary liquid decreases with the ethanol ratio f_e. It is also seen that σ changes rapidly for small ethanol fractions and more slowly for larger ethanol fractions. The surface tensions for $f_e = 67.5\%$ and $f_e = 80\%$ are shown in Table 5.1.

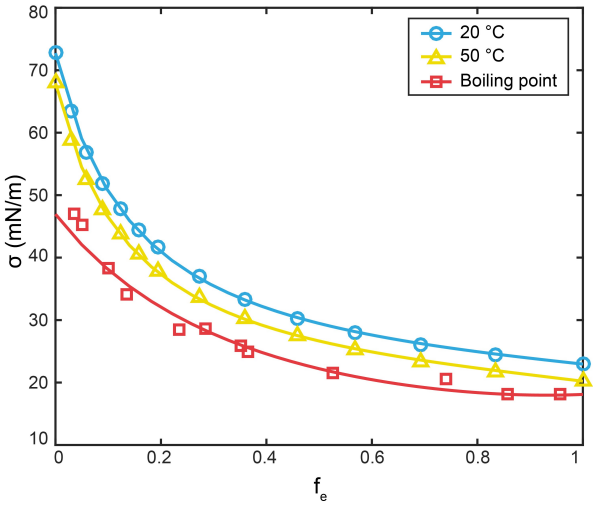

Figure 5.6: Surface tension of ethanol-water binary mixtures as a function of fe at 20 °C, at 50 °C, and at the respective boiling temperature of the mixture (which depends on f_e).

Table 5.1: Surface tension of binary liquids with ethanol ratio $f_e = 67.5\%$ and $f_e = 80\%$

Temperature	$\sigma(f_e = 67.5\%)$, mN/m	$\sigma(f_e = 80\%)$, mN/m
20 °C	26.46	24.94
50 °C	23.8	22.31
Boiling point	19.46	18.39

5.5.3 Robustness and reproducibility of the bubble shrinkage measurements

Figures 5.7a and 5.7b show repeated experimental results with the 5× (Fig. 5.7a (I)) and 10× (Fig. 5.7a (II)) objectives at an ethanol concentration $f_e = 70\%$ and at different ethanol concentrations for fixed laser powers of 60 mW (Fig. 5.7b (I)) and 100 mW (Fig. 5.7b (II)), respectively. Clearly, the dynamics of the bubble shrinkage at different laser powers and ethanol concentrations is robust and highly reproducible (see also Fig. 5.3b and 5.4c in the paper).

5.5.4 Dynamics of three-phase contact line and bubble radius

The dynamics of the three-phase contact line (triple-line) during bubble growth is shown in Fig. 5.8. For both the 5× and 10× magnification objective of laser focusing, the triple-line first slightly increases with the increasing bubble radius. The triple-lines jump at about 50 μm and 30 μm for the 5× and 10× objectives, respectively, as shown in Fig. 5.8. Thus, right after the jump, the radii of bubbles are slightly smaller than before. After that, the bubbles enter the steadily growing phase and the triple-line gradually moves outwards along with bubble growth.

5.5.5 Comparison of the bubble shrinkage dynamics on a substrate with a gold layer and gold nanoparticle decorated substrate

To confirm that the observed bubble shrinkage is not sample specific, we repeated the experiments on a substrate with a smooth gold layer immersed in a binary liquid with ethanol fraction $f_e = 70\%$. As shown in Fig. 5.9a and 5.9b, the contact angle of the water droplet on the bare gold substrate is 57.6°, which is much larger than the contact angle of water droplet on the gold nanoparticle

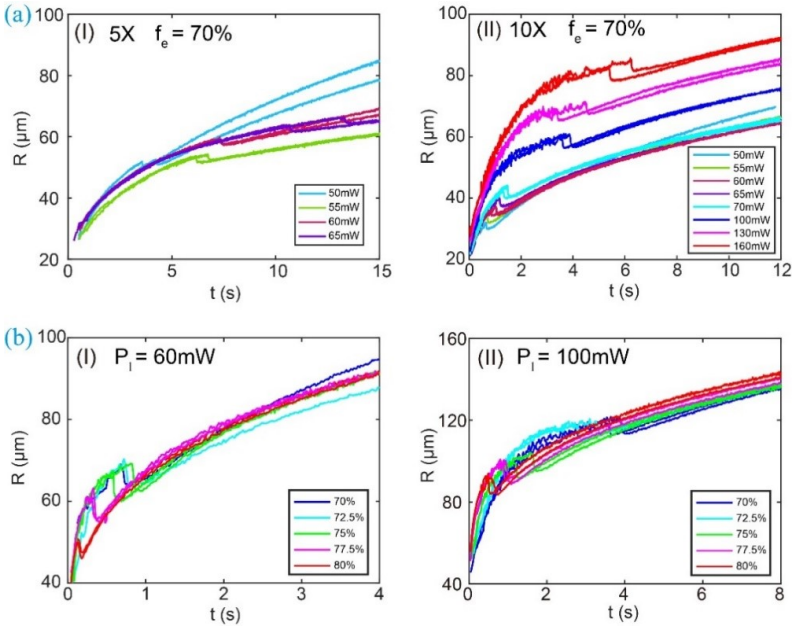

Figure 5.7: Repeated experimental results of the bubble shrinkage dynamics. (a) The bubble shrinkage dynamics for different laser powers using the 5× objective (I) and the 10× objective (II) at an ethanol concentration of f_e = 70%. (b) Bubble shrinkage dynamics for various ethanol concentrations in the regime of $67.5\% \lesssim f_e \lesssim 80\%$ at laser powers of 60 mW and 100 mW, respectively.

decorated fused silica substrate. We also measured the roughness of the two surfaces through an atomic force microscope. Atomic force microscope (AFM) height images for the two samples are shown in Fig. 5.9a (II) and 5.9b (II). The measured roughness values are 34.2 nm and 1.4 nm for the nanoparticles decorated substrate and the one with the gold layer, respectively. The comparison of the bubble growth dynamics on the gold layer substrate and gold nanoparticle decorated substrate is shown in Fig. 5.9c. Despite the large difference in surface roughness, the same sudden decrease in the bubble radius is observed. This means that the sudden bubble shrinkage process is a robust result and not sample-specific.

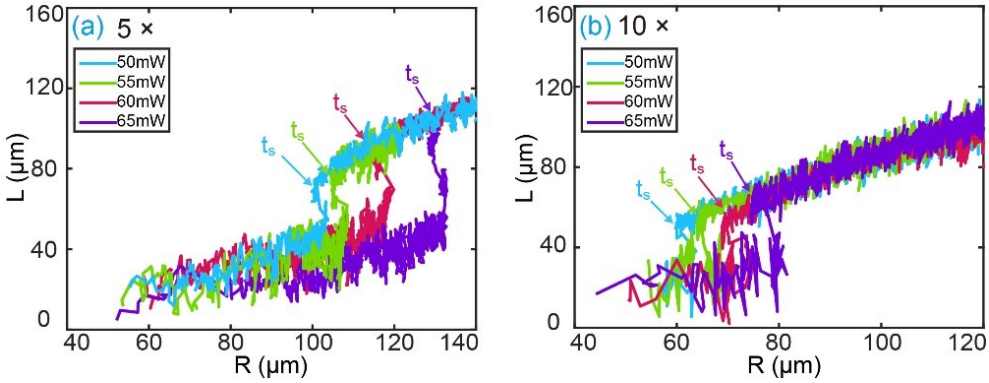

Figure 5.8: The footprint diameter L of the bubbles versus bubble radius R with different laser power values under 5× objective (a) and 10× objective (b), respectively.

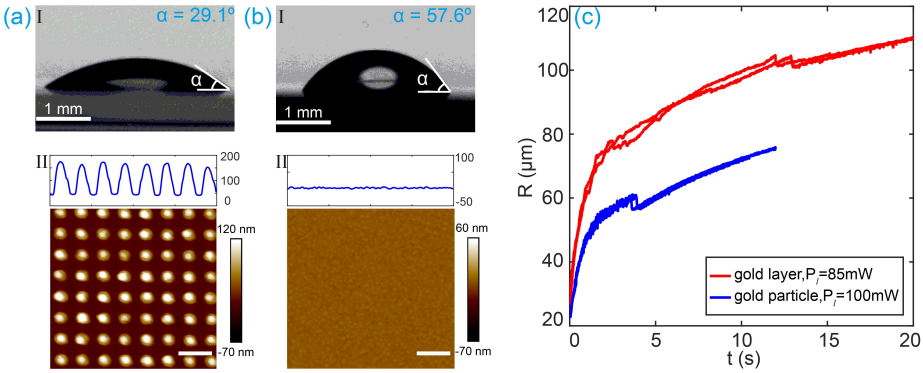

Figure 5.9: Contact angle of a water droplet and roughness measurement (via AFM height image measurement) for substrates with gold nanoparticle array (a) and a gold layer (b). (scale bars in AFM height images: 200 nm) The static contact angles of the water droplets on the two substrates are 29.1° and 57.6°, respectively. (c) The bubble growth dynamics on the gold nanoparticle decorated substrate at $P_l = 100$ mW and on the gold layer covered substrate at $P_l = 85$ mW in a binary liquid with $f_e = 70\%$.

Chapter 6

Droplet plume emission during plasmonic bubble growth in ternary liquids[1]

Plasmonic bubbles are of great relevance in numerous applications, including catalytic reactions, micro/nanomanipulation of molecules or particles dispersed in liquids, and cancer therapeutics. So far, studies have been focused on bubble nucleation in pure liquids. Here we investigate plasmonic bubble nucleation in ternary liquids consisting of ethanol, water, and trans-anethole oil which can show the so-called ouzo-effect. We find that oil (trans-anethole) droplet plumes are produced around the growing plasmonic bubbles. The nucleation of the microdroplets and their organization in droplet plumes is due to the symmetry breaking of the ethanol concentration field during the selective evaporation of ethanol from the surrounding ternary liquids into the growing plasmonic bubbles. Numerical simulations show the existence of a critical Marangoni number Ma (the ratio between solutal advection rate and the diffusion rate), above which the symmetry breaking of the ethanol concentration field occurs, leading to the emission of the droplet plumes. The numerical results agree with the experimental observation that more plumes are emitted with increasing ethanol-water relative weight ratios and hence Ma. Our findings on the droplet plume formation reveal the rich phenomena

[1]Published as: **Xiaolai Li**, Yibo Chen, Yuliang Wang, Kai Leong Chong, Roberto Verzicco, Harold J. W. Zandvliet, and Detlef Lohse, *Droplet plume emission during plasmonic bubble growth in ternary liquids*, Phys. Rev. E **104**, 025101 (2021). Experiments are done by Li, simulations are done by Chen.

of plasmonic bubble nucleation in multicomponent liquids and help to pave the way to achieve enhanced mixing in multicomponent liquids in chemical, pharmaceutical, and cosmetic industries.

6.1 Introduction

Plasmonic microbubbles are produced by immersed metal nanoparticles under laser irradiation due to plasmonic heating. They have received considerable attention, owing to their potential for numerous applications, such as biomedical diagnosis, cancer therapy [27–30, 163], micromanipulation of molecules or particles dispersed in solutions [31–33] and locally enhanced chemical reactions [21, 34]. A proper understanding of the dynamics of these plasmonic bubbles is therefore not only of fundamental interest, but also essential from a technological viewpoint as it might provide routes to tailor the formation and growth of the plasmonic bubbles.

During the last decade, numerous studies have been performed to explore the nucleation mechanism and growth dynamics of plasmonic bubbles [25, 35–38, 131, 164], as well as the effects of dissolved gas [24, 123, 139, 141, 165] and liquid types [39] on bubble growth dynamics. To date, these studies have nearly exclusively focused on plasmonic bubble formation in pure liquids. However, in many applications plasmonic bubbles nucleate in binary, ternary or even multicomponent liquids. This introduces new and rich physics and chemistry. E.g., due to selective evaporation, concentration gradients may occur, resulting in Marangoni forces and other rich physicochemical hydrodynamics [142, 166], which we want to further explore in this paper.

We have recently started this line of research and investigated plasmonic bubble nucleation in *binary* liquids of ethanol and water, and found that the solutal Marangoni flow, caused by the preferential vaporization of ethanol, results in the detachment of the bubbles from the substrate at low ethanol ratios ($< 67.5\%$) [167]. In binary liquids with ethanol ratios exceeding 67.5%, on the contrary, bubbles remain attached to the substrate and first steadily grow until they suddenly shrink. The shrinkage is induced by the depinning of the three phase contact line from the laser spot region, which is due to the decreased opto-thermal efficiency. For plasmonic bubbles in ternary liquids, the phase equilibrium is continuously altered by liquid vaporization and mass and thermal diffusion, resulting in a much richer and more complex behavior than in pure liquids.

To gain insight into the dynamics of plasmonic bubbles in ternary and multicomponent liquids, we study here the bubble formation in a controlled specific category of ternary liquids. Namely, we have selected a ternary liquid which shows the so-called ouzo effect [142, 168, 169], namely a solution consisting of ethanol, water, and trans-anethole. The ouzo effect describes the

spontaneous emulsification that occurs when water is added to dilute the solution, thus lowering its oil-solubility. The initially transparent solution then becomes milky because of the nucleation of oil microdroplets due to the reduced solubility of the oil in liquid mixtures with lower ethanol concentration [168, 170]. The emulsification can also occur if the amount of ethanol is reduced in different ways, for instance, through preferential evaporation or dissolution [169, 171, 172].

In this work, we present experimental and numerical studies on plasmonic bubble formation in the ternary liquids of ethanol, water , and trans-anethole. Interestingly, for certain ternary liquid ratios, we observe the emission of droplet plumes from the growing plasmonic bubbles, carrying the nucleated oil microdroplets away from the bubble. We will show that the key parameter governing the pattern and number of these emitted plumes is the Marangoni number, which is the dimensionless number that compares the solutal advection rate with the diffusion rate. By considering the experiments, numerical simulation and theory, we can provide a detailed understanding of the physicochemical processes that occur during plasmonic bubble growth in these multicomponent liquids.

Note that the formation of trans-anethole droplets out of an oversaturated ternary solution is an interesting nucleation problem in itself. It could be addressed from the viewpoint of classcial nucleation theory (CNT) [173–175], but this is not the subject of the present paper. If one were to do so, one would choose a much simpler geometry, say, by injecting water into an ouzo solution of well-defined properties. We do not have this here, due to partial evaporation of the binary liquid and thermal effects. So here it would be impossible to determine the values of the material parameters required in classical nucleation theory. In addition, it is nearly impossible to identify the size of individual droplets or their numbers in the droplet plumes, due to the limited image resolution of the high-speed imaging system, as well as the cloudy nature of the plumes. In a nutshell, the cloud of nucleated microdroplets is used as a convenient indicator to signal flow regions of relatively high water concentration or equivalently low ethanol concentration. In fact, we will show that the plume formation also works around plasmonic bubble in binary liquids, and can optically be visualized for large enough density contrast of the two involved liquids.

The paper is organized as follows: In section 6.2, we describe the experimental setup and procedure. Section 6.3.1 reports the experimental results for the plume formation around the growing plasmonic bubble in a ternary liquid and

section 6.3.2 compares them with those in a binary liquid. In section 6.3.3, we present our corresponding numerical results, which, in section 6.3.4, are quantitatively compared with the experimental ones. The paper ends with conclusions and an outlook (section 6.4).

6.2 Experimental setup and procedure

The preparation of sample with gold nanoparticle, and the experimental setup for plasmonic microbubbles imaging are shown in Fig. 4.1b and c in Chapter 4.2. In this study, plasmonic bubbles were monitored with two high-speed cameras: Photron SA7 for bottom-view imaging, and Photron SAZ for side-view imaging. Both cameras were operated at frame rate of 5 kfps.

6.2.1 Ternary liquid preparation

The ternary liquids used in our experiments are composed of ethanol (Sigma-Aldrich; $\geq 99.8\%$), deionized (DI) water (Milli-Q Advantage A10 System, Germany), and trans-anethole oil (Sigma-Aldrich; trans-anethole, $\geq$99.8). The ethanol and water were air saturated by exposure to air for 8 hours. Subsequently, they were mixed with trans-anethole oil to prepare seven different ternary liquids, as shown in Table 6.1. After mixing, the ternary liquids were immediately transferred into a sealed cuvette with a size of 10mm $\times$ 10mm $\times$ 50mm for experiments. During experiments, the cuvette was fully filled with the ternary liquid.

6.2.2 Experimental procedure

Plasmonic bubble generation experiments were performed in equilibrated ethanol-water-anethole mixtures. As depicted in the ternary diagram (Fig. 6.1), ternary liquids with seven different weight ratios, labelled from 1 to 7, were selected on the binodal curve (phase separation curve) for our experiments. The phase separation curve is based on the study by Tan *et al* [169]. In the ternary mixtures, the weight ratios of ethanol, water, and anethole oil are y_e, y_w, and y_a, respectively. Table 6.1 summarizes the detailed weight ratios of each component in the ternary liquid mixtures. Note that the absolute ethanol concentration y_e non-monotonically changes along the binodal curve. The seven ternary liquids were actually labelled with increasing ethanol-water relative weight ratio of $r_{e/(e+w)} = y_e/(y_e + y_w)$, which hereafter is used for analysis. At low ethanol concentrations, the plasmonic bubbles depin and

detach due to the strong upward Marangoni force, which has been systematically investigated in our previous study [167]. In contrast, bubbles can steadily attach to the substrate at high ethanol fractions.

Table 6.1: Weight ratios of y_e, y_w, y_a for ethanol, water, and anethole oil in different ternary mixtures used for plasmonic bubble formation. The liquids were labelled with increasing ethanol-water relative weight ratio $r_{e/(e+w)}$.

Label	$y_e(wt\%)$	$y_w(wt\%)$	$y_a(wt\%)$	$r_{e/(e+w)} = y_e/(y_e + y_w)$
1	62.58	33.71	3.71	65.0%
2	66.31	28.42	5.27	70.0%
3	68.09	22.70	9.21	75.0%
4	68.56	19.90	11.54	77.5%
5	68.67	18.25	13.07	79.0%
6	68.66	17.17	14.17	80.0%
7	64.15	11.32	24.52	85.0%

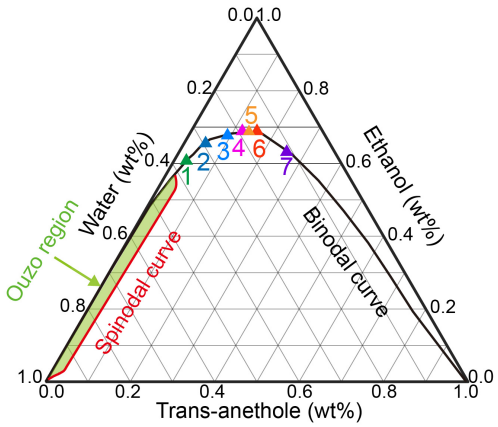

Figure 6.1: Ternary diagram of ethanol-water-anethole mixtures. The black solid line is the measured phase separation line [171]. The filled triangles (points 1-7) along the phase separation curve represent the initial compositions of the ternary liquids that we have used in this study.

6.3 Results and discussion

6.3.1 Plume formation around the growing plasmonic bubble in a ternary liquid

We first report our finding for the second regime, *i.e.*, the regime with high ethanol fractions. Figure 6.2a (I) shows a bottom-view image of a growing plasmonic bubble in a ternary liquid with ethanol-water relative weight ratio $r_{e/(e+w)} = 65.0\%$, corresponding to ethanol $y_e = 62.58\%$, water $y_w = 33.71\%$, and trans-anethole $y_a = 3.71\%$ in weight fractions. Interestingly, a cloudy black region consisting of oil microdroplets is observed starting at 1.68s (Fig. 6.2a II). The emulsification here results from the selective evaporation of ethanol from the ternary liquid [168]. Since ethanol has the lowest boiling temperature of the three components in the ternary liquid, ethanol vaporizes first, leading to an oversaturation of the left-behind liquid with the anethole oil and thus to the nucleation of anethole oil microdroplets. Remarkably, the cloudy region keeps rotating around the bubble. The bubble also displays some lateral movement (Fig. 6.2a III and IV). Hereafter we refer to the localized cloudy microdroplet regions as droplet plumes.

The formation of the droplet plumes is also observed in ternary liquids with the ethanol-water relative weight ratio of $r_{e/(e+w)} = 70.0 - 80.0\%$, as shown in Fig. 6.2b-d. For $r_{e/(e+w)} = 70.0\%$, we observe the emission of two droplet plumes (Fig. 6.2b II). The two plumes are formed at opposite sides of the bubble. Subsequently, they merge into a single droplet plume (Fig. 6.2b III and IV). For $r_{e/(e+w)} = 80.0\%$, there are initially three plumes (Fig. 6.2c II), which evolve later into four plumes (Fig. 6.2c III). Similar to the case of $r_{e/(e+w)} = 70.0\%$, the plumes are first distributed symmetrically around the bubble until eventually the localized plumes merge (Fig. 6.2c IV). However, in the ternary liquids with $r_{e/(e+w)} = 85.0\%$ (Fig. 6.2d), there is no pronounced droplet plume observed, but rather an oil ring is formed around the bubble (Fig. 6.2d II-IV). This can be rationalized by the high oil concentration ($y_a = 24.52\%$) dissolved in the original ternary liquids. Once the ethanol evaporates, the nucleated microdroplets accumulate around the bubble, coalesce and form the oil ring. Note that the bubble formation experiments were performed in a cuvette (10mm × 10mm × 50mm) fully filled with the ternary liquids. Therefore, the thickness of liquid inside the cuvette is about 10 mm, which is nearly 100 times larger than the bubble size (∼100 μm). The influence of the wall and interface on convection is negligible.

To get more insight into the bubble dynamics and the droplet plume formation,

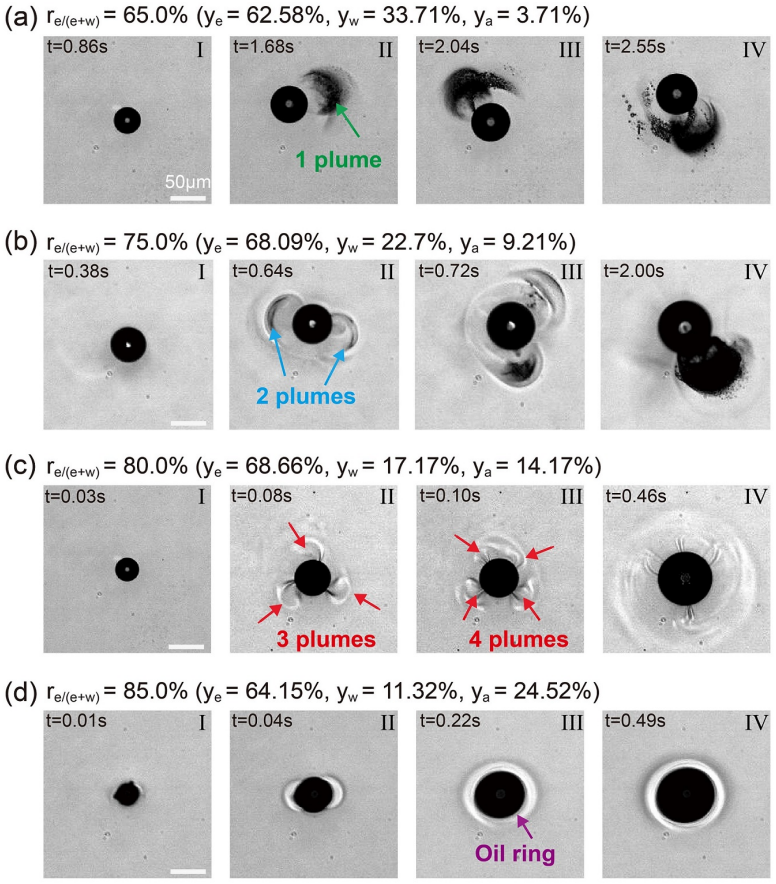

Figure 6.2: Bottom-view images of droplet plumes during plasmonic microbubble growth in ternary liquids. (a), (b), (c) and (d) show the evolution of droplet plumes with ethanol-water relative weight ratio $r_{e/(e+w)} = 65.0\%$, 75.0%, 80.0%, and 85.0%, respectively. With increasing $r_{e/(e+w)}$ from 65.0% to 80.0%, the initially emitted plume number increases from 1 to 3, as seen in Fig. 6.2a II, Fig. 6.2b II, and Fig. 6.2c II. For $r_{e/(e+w)} = 75.0\%$, the two plumes finally merge into a single plume (Fig. 6.2b II-IV). For $r_{e/(e+w)} = 80.0\%$, the initial three plumes (Fig. 6.2c II) evolve into four plumes (Fig. 6.2c III) and finally merge (Fig. 6.2c IV). Fig. 6.2d shows the formation of an oil ring in the ternary liquid with $r_{e/(e+w)} = 85.0\%$, corresponding to a high oil weight fraction $y_a = 24.52\%$.

the bubble volume and maximum plume number for different liquid ratios were extracted from our high-speed images. In Fig. 6.3a and b we plotted the volume of the plasmonic bubble versus time and the maximum number of droplet plumes versus the ethanol ratio $r_{e/(e+w)}$. Not surprisingly, the bubble growth in the ternary liquids here is very comparable to the bubble growth in ethanol-water binary liquids [167]. As shown in Fig. 6.3a, for fixed laser irradiation time, the bubble volume increases with increasing ethanol-water relative weight ratio $r_{e/(e+w)}$ from 65.0% to 80.0%. The anethole oil ratio in our ternary system is very low and anethole oil has a much higher boiling temperature than ethanol and water. As a result, anethole oil has limited influence on the vaporization process and the bubble growth in the ternary liquids. A larger relative ethanol fraction in ethanol-water binary liquids results in a large bubble growth rate [167]. The maximum plume number, N_{max}, was found to increase with increasing $r_{e/(e+w)}$, see Fig. 6.3b.

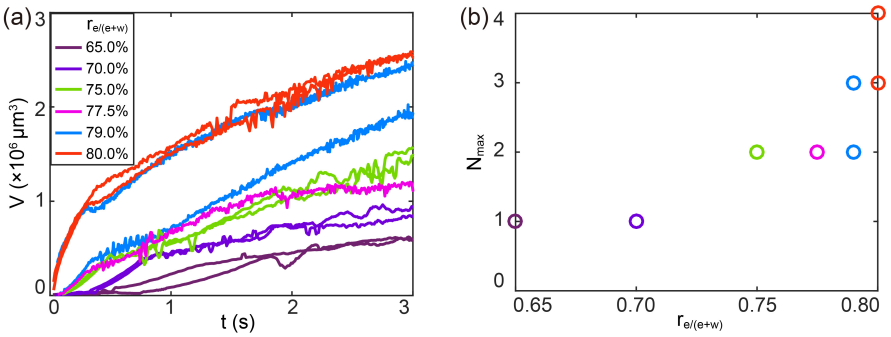

Figure 6.3: (a) Bubble volume V versus time and (b) maximum plume number N_{max} versus ethanol-water relative weight ratio $r_{e/(e+w)}$ in the ternary liquids.

We note that the two curves at $r_{e/(e+w)} = 79.0\%$ deviate from each other in Fig. 6.3a. We believe that this is due to the fact that $r_{e/(e+w)} = 79.0\%$ is close to the critical ethanol fraction (77.5%-80.0%) at which the transition from depinning (at $r_{e/(e+w)} < 77.5\%$) to pinning ($r_{e/(e+w)} \geq 80.0\%$, see Fig. 6.2c) of the plasmonic bubble to the laser spot occurs. For a high ethanol ratio $r_{e/(e+w)} \geq 80.0\%$, the bubble remains pinned to the laser spot region (Fig. 6.2c), the position of which locates at the center of each image in Fig. 6.2. As a result, one can barely see the lateral movement of the bubbles for $r_{e/(e+w)} \geq 80.0\%$. However, for a lower ethanol ratio $r_{e/(e+w)} < 77.5\%$, bubbles are not pinned at the laser spot (see Fig. 6.2a and b). They could move away from the laser spot region. The laser spot has a Gaussian power

density distribution, so the further the bubbles are located away from the laser spot center, the weaker the heating efficiency as well as the vaporization rate. As a result, apart from the dependence on the ethanol ratio $r_{e/(e+w)}$, the growth rate of those bubbles that are depinned from the laser region is even smaller.

The mechanism of the droplet nucleation in experiments can be explained as follows. Under continuous laser heating the volatile ethanol in ternary liquids vaporizes into the bubble. Consequently, the liquid in the region near the bubble interface becomes ethanol depleted, and an ethanol concentration gradient emerges. The reduction of ethanol in the initially equilibrated ternary liquid leads to the oversaturation of the left-behind liquid with the anethole oil, and eventually to the nucleation of oil microdroplets (the so-called ouzo effect). However, the reason why the symmetry of oil droplet distribution around the bubble breaks and how the droplet plumes form remains to be explained, and we will do so below.

6.3.2 Comparison of plume formation around growing plasmonic bubbles in binary and in ternary liquids

To demonstrate that the oil droplets do not change the essence of the overall flow dynamics and to provide a comparison of the cases with and without oil microdroplet nucleation, we performed another experiment in a binary liquid of ethanol and trans-anethol oil, which are fully miscible. We observed a similar plume phenomenon, as shown in Fig. 6.4a and b. Ethanol and anethol oil can be mixed in any ratio. During bubble growth under laser heating, it is ethanol which preferably vaporizes, due to the ethanol low boiling point. As a result, a concentration gradient of anethol oil in the vicinity of the laser irradiated area will form and can be visualized because of the different refractive index of ethanol and oil.

Figures 6.4a and b show the plasmonic bubble growth in ethanol anethol mixtures with ethanol ratio $r_e = 70\%$ and 80%, respectively. It can be seen that during bubble growth, plumes are generated in the ethanol anethol oil mixtures, and the maximum plume number increases with increasing ethanol ratio. This verifies that the plumes can be formed regardless of the droplet nucleation.

For the droplet plumes in ternary liquids of ethanol, water and trans-anethol, the hydrodynamics of the plumes is coupled with the droplet nucleation. We note that there are certain quantitative differences between the experiments in ternary liquids (Fig. 6.2) and in binary liquids (Fig. 6.4). This might

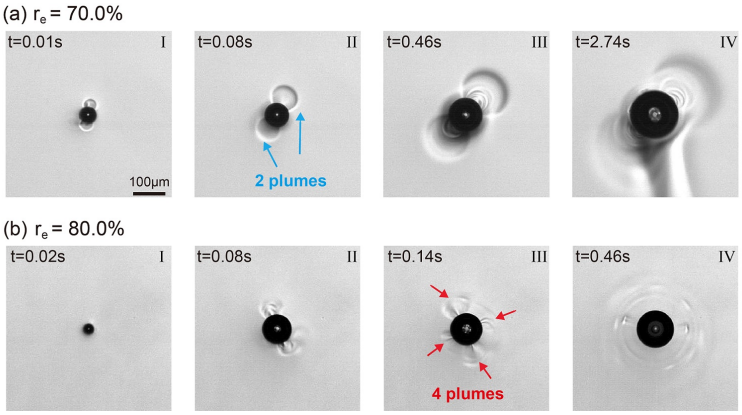

Figure 6.4: Plasmonic bubbles in ethanol and anethol oil mixtures with ethanol ratio $r_e = 70\%$ (a) and $r_e = 80\%$ (b). Plume formation is observed in both cases and the maximum plume number increases with increasing ethanol ratio.

be attributed to the influence of phase nucleation in the ternary liquids, in which an energy barrier must be surmounted to bring the system in visible stable phase transition. Moreover, the phase nucleation process is controlled by thermal fluctuations and affected by the defects of wall or impurities in liquids, leading to the stochastic properties of droplet nucleation with ternary liquids. However, a quantitative analysis of these differences is beyond the scope of this study.

6.3.3 Numerical simulations of the plasmonic bubble in an ethanol-water mixture

Underlying equations and control parameters

To confirm the outlined physical picture, we numerically investigate the vaporization and plume formation during plasmonic bubble growth. Since the ratio of anethole oil in the ternary liquid is very low and the boiling point of anethole oil (234 °C) is much higher than that of water and ethanol, it hardly vaporizes during the experiments. Therefore, to reduce the complexity of the numerical model, we only consider water and ethanol. The physical variables to describe the system are thus the concentration of ethanol $c(\boldsymbol{x}, t)$ and the velocity of the fluid $\boldsymbol{u}(\boldsymbol{x}, t)$. A bubble of radius R immersed in the ethanol-water mixture is fixed near the bottom wall (Fig. 6.5a). Under laser

irradiation, the bubble takes up ethanol vapor with a constant rate α from the fluid at the bubble surface:

$$D\partial_n c = \alpha. \tag{6.1}$$

where D is the diffusion coefficient of ethanol, and $\partial_n c$ is the concentration gradient in normal direction. The ethanol concentration difference along the bubble surface will lead to a surface tension difference, and induce a Marangoni flow. The solutal Marangoni flow is accounted for by balancing the surface tension difference with the viscous force at the interface (Fig. 6.5b) [176]:

$$\partial_c \sigma \partial_\tau c = \eta \partial_n \boldsymbol{u}, \tag{6.2}$$

where σ is the surface tension, $\partial_c \sigma$ represents the derivative of the surface tension with respect to the concentration, $\partial_\tau c$ is the tangential concentration gradient, η is the dynamic viscosity, and $\partial_n \boldsymbol{u}$ is the normal gradient of the velocity.

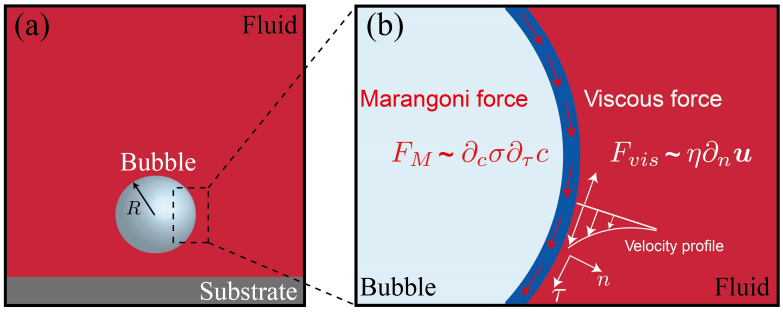

Figure 6.5: (a) Schematics of the numerical model. The domain is filled with the ethanol-water mixture and a bubble of radius R is placed near the bottom wall. (b) A zoom-in display for the area selected by the dashed box at the bubble surface in (a). Concentration differences along the bubble surface lead to a Marangoni force, which is balanced by the viscous force induced by the Marangoni flow.

We non-dimensionalize the velocities, lengths, and concentrations with $\partial_c \sigma \alpha R/\eta D$, R, and $\alpha R/D$, respectively. The time evolution of the concentration field c and the velocity field $\boldsymbol{u}$ are obtained by the Navier-Stokes equation and the advection-diffusion equation:

$$\frac{\partial \boldsymbol{u}}{\partial t} + (\boldsymbol{u} \cdot \nabla)\boldsymbol{u} = -\nabla p + \frac{Sc}{Ma}\nabla^2 \boldsymbol{u}, \nabla \cdot \boldsymbol{u} = 0 \tag{6.3}$$

$$\frac{\partial c}{\partial t} + \boldsymbol{u} \cdot \nabla c = \frac{1}{Ma}\nabla^2 c, \tag{6.4}$$

where Sc and Ma are Schmidt number and Marangoni number, respectively. The Schmidt number is the ratio between the kinematic viscosity ν to the diffusion coefficient D,

$$Sc = \frac{\nu}{D}, \tag{6.5}$$

The Marangoni number is the ratio between Marangoni flow induced advection and diffusion, reflecting the strength of the Marangoni force:

$$Ma = \frac{\alpha R^2 \partial_c \sigma}{\eta D^2}. \tag{6.6}$$

In the numerical simulation, we solve the non-dimensional form of the governing Eqs. (6.3) and (6.4) and boundary conditions (Eqs. (6.1) and (6.2)). The kinematic viscosity of ethanol-water mixture is $\nu = 2.7 \times 10^{-6}$ m^2/s and the diffusion coefficient of ethanol in water is $D = 1.23\times 10^{-9}$ m^2/s [169,177]. Accordingly, the Schmidt number Sc is taken as 2220 in the simulation. Ma was varied from 5×10^3 to 5×10^5. For details regarding the numerical simulations we refer to the Appendix 6.5.1.

Numerical results

The simulation results for the ethanol water system with different values of Ma are shown in Fig. 6.6. It is found that the ethanol concentration field remains perfectly symmetric for $Ma \leq 5 \times 10^3$ (Fig. 6.6a I-III). For $Ma = 5 \times 10^4$, the symmetry of the ethanol concentration breaks and a single plume of ethanol poor liquid is emitted (Fig. 6.6b). For $Ma \geq 7.5 \times 10^4$, multiple plumes are emitted (Fig. 6.6c II, d II and e II). The maximum number of the emitted plumes increases with increasing Ma. Moreover, multiple plumes subsequently merge (Fig. 6.6c III, d III and e III), which is consistent with our experimental observations.

The numerical results clearly show that the formation of plumes is directly related to the Marangoni number Ma. At low Marangoni number Ma, the diffusion process dominates and thus any sharp concentration gradient can be smoothed out by the diffusive process. Therefore, the ethanol concentration field remains symmetric. For Ma above a certain value, the symmetry of ethanol concentration spontaneously breaks and concentration plumes are formed.

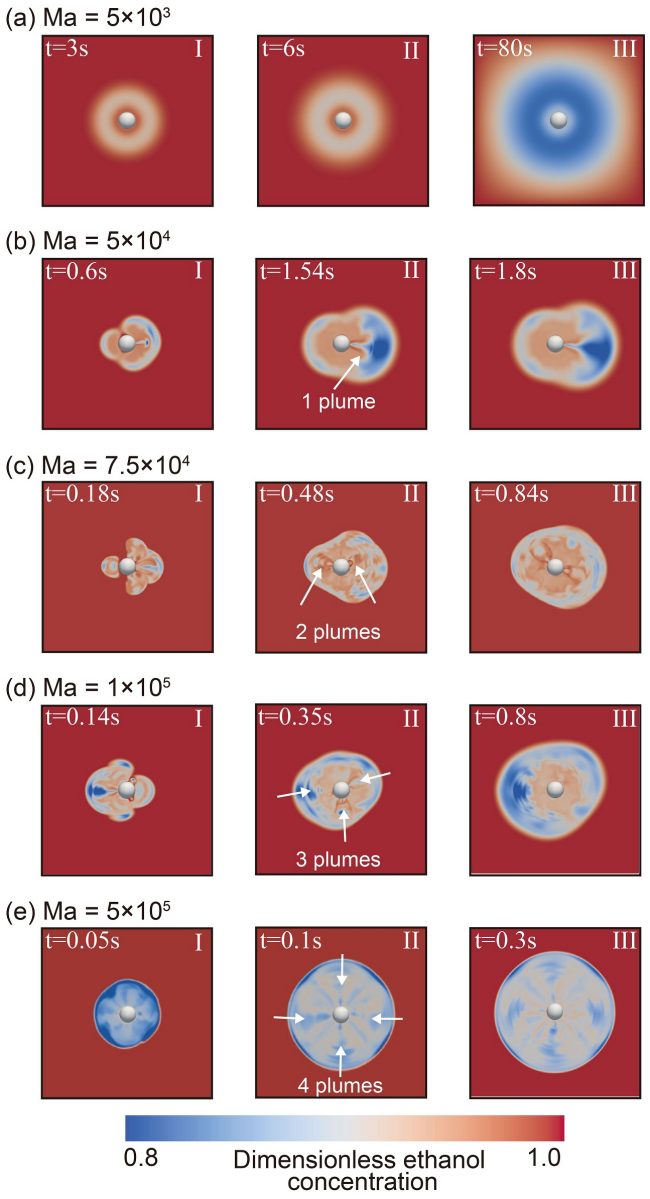

Figure 6.6: Snapshots (top-view) of the ethanol concentration field near a plasmonic bubble from the simulation in the ethanol water mixtures during the vaporization process. The symmetry of the concentration field breaks for Marangoni numbers $Ma \geq 5 \times 10^4$. With further increasing Ma, the number of plumes increases from 1 to 4. In (c)-(e), neighbouring plumes can merge.

A similar phenomenon of symmetry breaking is observed in the case of catalytic particles with diffusio-phoretic effects. Michelin et al. [178] demonstrates that when the Péclet number (characterizes the ratio between advection led by diffusio-phoresis and mass diffusion) is above a certain value, the particle will break the symmetry spontaneously. Chen et al. [179] further explored catalytic particles at high Péclet number. They found that multiple plumes are generated at the surface of the particle and the number of plumes increase with increasing Péclet number. The system studied here share similarities with the diffusio-phoretic problem in their symmetry-breaking mechanism and the plume emission at the surface. However, the two systems are different, namely in refs. [178,179] it is the diffusio-phoretic flow at the surface which drives the particle, whereas here it is the Marangoni flow due to the gradient in surface tension.

6.3.4 Quantitative comparison between numerical and experimental results

To more quantitatively compare our numerical results with the experimental data, we estimated the Marangoni number Ma in our experiments with the definition of Eq. (6.6). In the experiments, the bubble radii kept changing with time. In order to compare with the numerical results, we take the radius of the bubble at the moment when pronounced plume formation in the experiments is observed to calculate Ma. As mentioned earlier, we ignored the presence of trans-anethole oil as its relative concentration is very low. The term $\partial_c \sigma$ is estimated to be 1.7×10^{-5} N $\cdot$ m^2/kg from the surface tension curves (5.6 in Chapter 5). To estimate the mass transfer rate α, we assume that the bubble growth is dominated by ethanol evaporation. α is defined as $\alpha = K_e(t)/S_b$, where $K_e(t)$ is the consumption rate of ethanol and S_b is the area of bubble surface where the mass transfer takes place. The consumption rate $K_e(t) = \mathrm{d}(M_e n_e)/\mathrm{d}t$, where $M_e = 46$ kg/mol is the mole weight of ethanol, $n_e = P_0 V/R_0 T$ is the amount of ethanol molecules in mole, the temperature $T \approx 353$ K (boiling temperature), P_0 the ambient pressure and R_0 the ideal gas constant. The consumption rate $K_e(t)$ can be obtained by extracting the bubble volume growth rate, *i.e.* $\mathrm{d}V/\mathrm{d}t$, from the curves shown in Fig. 6.3a.

As depicted in Fig. 6.7a, under laser irradiation, only the liquid in the vicinity of the three-phase contact line is heated up to the boiling temperature, resulting in the vaporization of ethanol. Therefore, here we take $S_b = 2\pi RH$ as the

bubble surface area for mass transfer. In order to obtain the height H, we determine the width of the thermal boundary layer. As shown in Fig. 6.7a, there is a downward solutal Marangoni flow along the bubble interface and therefore an outward flow along the substrate due to the selective vaporization of ethanol. This flow can be observed from side view images and the flow velocity $u_0 \approx 0.1$ m/s is obtained by particle image velocity measurement. The thermal boundary layer (the blue curve of the zoom in image in Fig. 6.7a) is given by $\delta_T = \delta_v Pr^{-1/3}$ [180]. In this expression, the velocity boundary layer is given by $\delta_v \approx 5R/Re^{1/2}$, the Reynolds number $Re = u_0 x/\nu$, the kinematic viscosity $\nu \approx 2.7 \times 10^{-6}$ m^2/s and x is the lateral position. The Prandtl number $Pr = c_p \mu/\lambda$, in which the thermal conductivity $\lambda = 0.6$ W/mK. The heat capacity of the liquid $c_p = 4179.6$ J $\cdot$ kg^{-1} $\cdot$ K^{-1}.

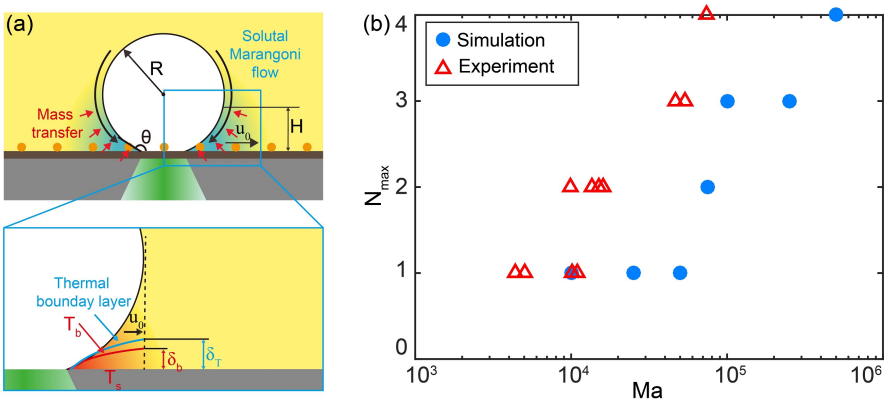

Figure 6.7: (a) Schematic illustration of the solutal Marangoni flow along the bubble interface caused by selective evaporation of ethanol. Ethanol vaporization occurs in a local area near the bubble bottom. R and H are the bubble radius and the height of the bubble where mass transfer into the bubble can occur, respectively. u_0 denotes the flow velocity along the substrate. The zoom-in image shows the thickness δ_T of the thermal boundary layer. The liquid in the region above the blue curve is at room temperature. The region of thickness δ_b (below the red curve) has liquid with a temperature above the boiling temperature T_b. It can be obtained by assuming a linear temperature decrease from the substrate to the blue curve. (b) Maximum plume number N_{max} as function of the Marangoni number Ma. Theory *vs* experiment.

Room temperature (20 °C) is taken as T_0 for the region outside the thermal boundary layer δ_T (the blue curve in Fig. 6.7a). The substrate temperature

T_s is estimated by our numerical simulation by assuming that the substrate is completely covered by vapor. The heat conductivity of the fused silica substrate was taken as 1.4 W/m · K (0-20 °C). The details of the numerical simulation method can be found in our recent publication [25]. Using this method, the spatial-temporal evolution of the substrate temperature can be obtained. The temperature field after 2 s of laser irradiation is shown in Fig. 6.10 of (Appendix 6.5.2). The temperature of the substrate at the three phase contact line L is used to determine the thickness of the thermal boundary layer. From the simulation results we obtain a substrate temperature $T_s \approx$ 96 °C. By assuming that temperature linearly decreases from the substrate to the blue curve (Fig. 6.7a), the liquid region (δ_b) having a temperature above the saturation temperature of ethanol water mixture (about 80 °C) can be obtained. Our calculation reveals that δ_b is about 10 μm at $x = R = 50$ μm.

The number of plumes as a function of Ma extracted from the experimental data and the numerical simulations is shown in Fig. 6.7b. The numerical and experimental results have the same trend and agree qualitatively well, albeit for a fixed number of plumes the Marangoni number in the simulations is slightly larger than that in the experiments. We believe that this is due to underestimating $\partial_c\sigma$ and the mass transfer rate α in the experimental estimation of Ma. Our arguments for this are twofold: First, the surface tension gradient $\partial_c\sigma$ was calculated for the initial ethanol concentration. However, the actual ethanol concentration in the boundary layer is much lower than the initial value because of the selective vaporization of ethanol. Since the surface tension of the ethanol-water mixtures changes more rapidly at lower ethanol concentrations than at larger one, the actual value of $\partial_c\sigma$ is larger than that of the initial value. Second, the ethanol consumption rate α was obtained assuming that the substrate is completely covered by vapor. Under this assumption, the substrate temperature, as well as the thermal boundary layer is determined. However, as depicted in the sketch of Fig. 6.7a, part of the substrate is in contact with the liquid outside the pinned bubble footprint area. As the liquid has a higher heat conductivity than vapor, the actual temperature of the substrate must be lower than what we have used in our numerical simulation. The overestimation of the substrate temperature leads to a larger boundary layer and therefore a smaller α. These two effects both contribute to the underestimation of the Marangoni numbers from experiments. Nonetheless, it is clear that the numerical results qualitatively agree well with the experimental ones.

6.4 Conclusions

To summarize, we have experimentally presented the emulsification of oil droplets induced by plasmonic bubble nucleation in ternary liquids of ethanol-water-anethole. It has been shown that anethole oil microdroplets nucleate around the bubble due to the selective vaporization of ethanol. The oil microdroplets then form droplet plumes. When the ethanol-water relative weight ratio $r_{e/(e+w)}$ increases from 65.0% to 80.0% in the ternary liquids, plasmonic bubbles grow faster and more droplet plumes are emitted. A quantitative understanding on the plume formation is achieved by a numerical study, which shows that the ethanol concentration field can only remain symmetric for a Marangoni number $Ma < 5 \times 10^4$ (diffusion dominated). Above a critical value of $Ma = 5 \times 10^4$, a symmetry breaking of the ethanol concentration field takes place, leading to the formation of droplet plumes. The revealed Ma dependence of the maximum plume numbers in the numerical results agrees with that in experiments.

This work has given insight into the rich phenomena of plasmonic bubble induced oil microdroplet nucleation (ouzo effect) in ternary liquids and the self-organization of these microdroplets. The quantitative understanding on plume formation offers valuable information for tuning and optimizing the flow field of multiple component liquids in various physicochemical processes. E.g., systems with a high Marangoni number can lead to breaking of the symmetry of the concentration field, and the emerging convection flow may have the advantage of enhanced mixing of ternary liquids in chemical, pharmaceutical, and cosmetic industries.

6.5 Appendix

6.5.1 Details on the numerical model

The simulation was conducted in a three dimensional domain $L_x \times L_y \times L_z = 20R \times 20R \times 20R$ with $201 \times 201 \times 201$ grids. A bubble with a radius R is fixed at a distance $h = 1.2R$ above the middle of the bottom wall (Fig. 6.8).

In non-dimensional form the boundary conditions (Eqs. (6.1) and (6.2)) read:

$$\partial_{\tilde{n}}\tilde{c} = 1, \quad \partial_{\tilde{\tau}}\tilde{c} = \partial_{\tilde{n}}\tilde{\boldsymbol{u}} \tag{6.7}$$

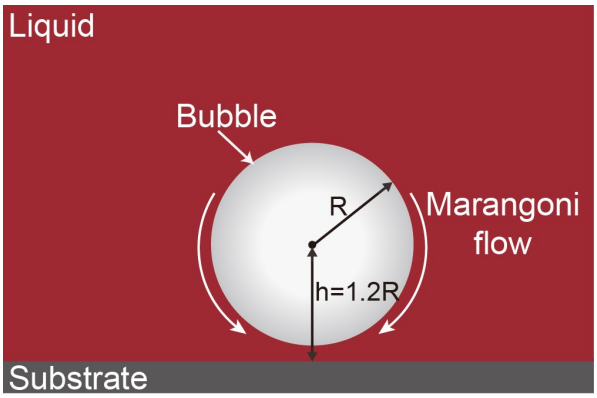

Figure 6.8: The numerical setup for a bubble with a constant radius R fixed at $h = 1.2R$ above the bottom wall. There is a constant normal concentration gradient at the bubble surface due to the evaporation of ethanol in the surrounding ethanol water mixture. Marangoni flow is induced by the ethanol concentration difference along the bubble surface. Note that the simulation is conducted in a three dimensional domain although the sketch is two dimensional.

The governing equations of the flow field were the Navier-Stokes and diffusion-convection equations Eqs. (6.1) and (6.2). The equations were spatially discretized using the central second-order finite difference scheme. Along both horizontal and vertical directions, homogenous staggered grids were used. The equations were integrated by a fractional-step method with the non-linear terms computed explicitly by a low-storage third-order Runge-Kutta scheme and the viscous terms computed implicitly by a Crank-Nicolson scheme [181]. To satisfy the concentration and velocity boundary conditions at the bubble surface, we applied the moving least square (MLS) based immersed boundary (IB) method, where the particle interface was represented by a triangulated Lagrangian mesh. The details of our MLS-based IB method are documented in Spandan *et al* [182]. Schematic of Fig. 6.9 illustrates the immersed boundary method with staggered grids. For clarity, we use two-dimensional grids in Figure 6.9 although the simulation is done in three dimensions. The Lagrangian points are denoted as red circle at the boundary (red curve), and the Eulerian points by the squares. A staggered mesh was applied to increase the accuracy. Therefore, the velocity points and concentration/pressure points are at different locations denoted by squares of different colors.

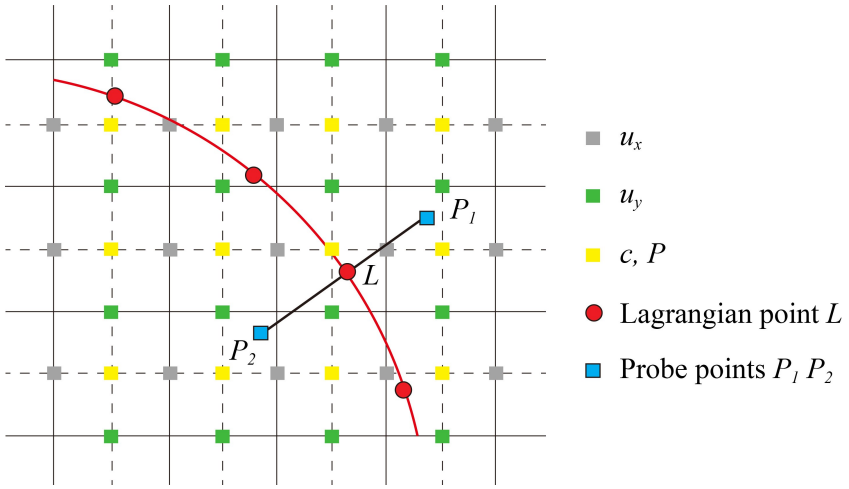

Figure 6.9: Schematic illustration of the immersed boundary method with staggered grids: Eulerian grids of velocity points and concentration points are denoted by different color, and the Lagrangian points at the boundary is denoted by red circle. The governing equations are solved on the Eulerian grids and the boundary conditions are satisfied at L point based on the interpolated value at the probes P_1 and P_2 points.

In the simulation, the concentration boundary condition (Eq. (6.7)a) is satisfied by enforcing the concentration at the inner probe point (point P_2 in Fig. 6.9) based on concentration interpolated at the probe located at a short distance (1 grid size h) from the surface of the particle (point P_1 in Fig. 6.9):

$$\frac{c_R - c_{P_2}}{2h} = 1 \tag{6.8}$$

The surface gradient of the concentration in the velocity boundary condition (Eq. (6.7)b) was calculated by the nearby Lagrangian concentration. The velocity boundary condition at the surface of the particle (point L in Fig. 6.9) was then enforced based on the velocity interpolated at the probe located at a short distance (1 grid size) from the surface of the particle (point P_1 in Fig. 6.9):

$$\frac{u_R - u_L}{h} = \nabla_s c_L \tag{6.9}$$

6.5.2 Numerical calculated temperature field of the substrate

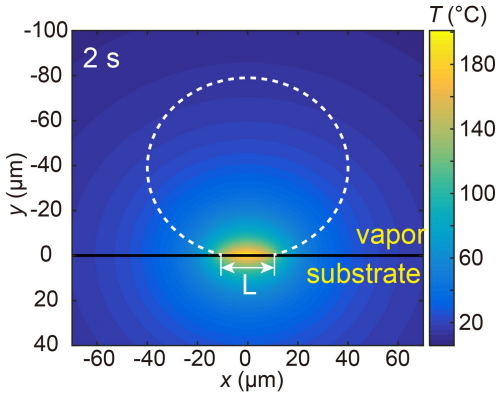

Figure 6.10: Numerical calculated temperature field of the substrate immersed in vapor upon laser irradiation for 2 s.

Chapter 7

Conclusions and outlook

In this thesis we have focused on two categories of bubbles: (i) Surface micro/nanobubbles on structured surfaces. We show that the pinning effect of surface structures contributes to surface nanobubble nucleation and stability. (ii) Plasmonic microbubbles. We studied the gas effect on plasmonic bubble dynamics and bubble formation in binary and ternary liquid system.

In Chapter 2, we investigated the spontaneous nucleation of nanobubbles (NBs) on nanostructured surfaces. We observed three categories of air entrapment, namely protruding NBs at nanopits with widths in between 50-100 nm, planar NBs at nanopits with widths of 100-150 nm, and no air entrapment at nanopits with diameter larger than 150 nm. The size and contact angle of the protruding NBs linearly increase with nanopit width. Based on the crevice nucleation theory, the formation of NBs on surface nanocavities is speculated as follows: First gas present in surface cavities. After immersion of the surface, gas dissolved in the locally over-saturated liquid diffuses into the air pockets. Then the air pockets grow out of the cavities, determining the final morphology of the NBs. The differences of the protruding NBs on small nanopits and planar NBs on medium nanopits can be explained by the diffusion process. On the one hand, the planar NBs could be not in diffusive equilibrium yet. The diffusive timescale is $\tau_D \sim L^2\rho/Dc_s\zeta$, *i.e.*, $\propto L^2$, *i.e.*, for larger pits it takes much longer to equilibrate. On the other hand, bubbles on these medium sized nanopits have larger footprint diameters, and requires more oversaturated air to make the gas-liquid interfaces grow out of the nanopits and depletion effects may occur. Moreover, we observed entrapped NBs on irregular nanopores ex-

hibiting non-spherical-cap-shapes, which further verifies the pinning effect of the surface nanostructures.

In Chapter 3, we further increase the surface structure size to micrometers and explore the temporal evolution of entrapped bubbles in microwells. We find that the microwells on hydrophobic surfaces are able to trap gas and form microbubbles. Right after immersion, the microwells were initially fully covered by the entrapped microbubbles. Subsequently, the three phase contact line pinned on the microwell edges partially detaches and the microbubbles rapidly shrink to a smaller size. The size of the initial trapped microbubbles is proportional to the microwell size. During shrinkage process, the square of footprint area of the microbubbles decreases linearly with time, which indicates a constant contact angle dissolution mode and agree with experimental observations. In addition, we applied different flow rates and undersaturations during bubble entrapment. It is found that the flow rates have no influence on the dynamics of microbubble entrapment and dissolution, and a higher undersaturation enhances microbubble dissolution.

In Chapter 4, we start the studies on plasmonic bubbles, and first investigate the effect of the dissolved gas on the dynamics of plasmonic bubble nucleation and dynamics. We performed experiments with different gas concentrations of $c_\infty/c_s = 0.10$, 0.80 and 1.20 for the initial giant bubbles in early phase, and $c_\infty/c_s = 0.55$, 0.65, 0.75, 0.85, 0.96, and 1.20 for the long-term bubble growth. In the early phase, lower gas concentrations lead to a longer delay times τ_d, larger maximum volume, and higher nucleation temperature, which indicates that the dissolved gas facilitates bubble nucleation. Besides, the maximum volume of the initial giant bubbles linearly depends on the input energy, and the prefactor of this linear relation is the same for all gas concentrations. This suggests that the initial giant bubbles are vapor bubbles. For the long-term ($> 0.2s$) growth, It is found that the growth rate κ of the bubble volume monotonically increases with gas concentration c_∞/c_s and laser power P_l. Moreover, the experimental results show a linear dependence of $\kappa = k_{P_l} P_l$, where k_{P_l} linearly increases with c_∞/c_s. The radius $R(t)$ of the plasmonic bubbles follows the power law dependence $R(t) \propto t^\alpha$. For all laser powers, the effective exponent α for all laser powers is approximately 1/3 when c_∞/c_s is larger than 0.85. However, for lower c_∞/c_s values, the effective exponent is smaller than 1/3 and monotonously decreases with decreasing P_l and c_∞/c_s. The smaller exponent α with lower c_∞/c_s is because that the input energy is first consumed to heat up the degassed water to a temperature where it

becomes super-saturated and gas can be expelled.

In Chapter 5, we explored the growth dynamics of plasmonic microbubbles in water-ethanol binary liquids. We find that the growth dynamics of plasmonic microbubbles in water-ethanol mixtures strongly depends on the ethanol concentration. We observed that the bubbles detach from the substrate at ethanol concentrations below 67.5%, which results from a strong downward Marangoni flow induced by selective vaporization. For ethanol concentrations in the range from 67.5% to 80%, we observed stable bubble growth at the surface, while a sudden bubble shrinkage takes place after a delay time t_s. We reveal that the sudden shrinkage originates from the complete depinning of the wiggling bubble from the laser spot area on the sample surfaces. Prior to the shrinkage occurrence, the bubble was pinned or partially pinned on the laser spot. When the liquid around the pinned region is completely evaporated, the instantaneous expansion of the three-phase contact line as well as the sudden shrinkage takes place. When $f_e \gtrsim 80\%$, the bubbles exhibit steady growth without sudden shrinkage. This attributes to that the binary solutions with high ethanol ratios becoming azeotropic, leading to a similar behavior as in pure liquids.

In Chapter 6, we studied plasmonic bubble nucleation in ternary liquids of ethanol-water-anethole. We observed that during bubble growth anethole oil microdroplets nucleate around the bubble, and form droplet plumes. When the ethanol-water relative weight ratio $r_{e/(e+w)}$ increases from 65.0% to 80.0% in the ternary liquids, plasmonic bubbles grow faster and more droplet plumes are emitted around the bubbles. To quantify the plume formation, we performed a numerical simulation on the selective vaporization process of ethanol-water system, providing that oil plays a minor role in vaporization because of its high boiling point and low ratio in the ternary system. The numerical results show that there exists a critical Marangoni number $Ma = 5 \times 10^4$, above which the symmetry of the ethanol concentration field breaks, leading to the formation of droplet plumes. The mechanism is that at low Marangoni number Ma, the diffusion process dominates and thus any sharp concentration gradient can be smoothed out by the diffusive process. Therefore, the ethanol concentration field remains symmetric. For Ma above a certain value, the symmetry of ethanol concentration spontaneously breaks and concentration plumes are formed. In addition, we also revealed Ma dependence of the maximum plume numbers in the numerical results, which agrees well with that in experiments.

In general, Chapter 2 and 3 show that the surface structures lead to gas en-

trapment and can act as pinning sites for surface nanobubblees. This not only helps the understanding in the nucleation mechanism and surprising stability of surface nanobubbles, but also provides an effective way for surface nanobubble formation with controllable position, size and shape. Though there have been a lot of efforts on nucleation origin and properties of surface nanobubble, a comprehensive validation and open questions remain. Future interests might be (i) What is the entrapment dynamics in oversaturated condition. (ii) A quantitative comparison of entrapped bubbles in controlled saturation levels with theoretical prediction. (iii) Collective behaviors of the entrapped bubbles. (iv) Bubble formation on uncircular structures.

For the plasmonic bubbles, our studies (Chapter 4-6) gain insights into the rich phenomena of plasmonic bubbles in binary and ternary liquids, which offers valuable information for tuning and optimizing the flow field of multiple component liquids in various physicochemical processes. Further interesting studies for the future development of this promising field include interactions of multiple plasmonic bubbles, experimental validation of plasmonic nanobubbles, and the possible transition from nanobubble to microbubbles, controlled size and components for applications in microfluidics and many others.

References

[1] W. C. Evans, "Knowledge of the fount and the cause of disaster", Nature **379**, 21–22 (1996).

[2] A. Robock, "Volcanic eruptions and climate", Rev. Geophys. **38**, 191–219 (2000).

[3] A. Rosa and J. Rubio, "On the role of nanobubbles in particle–bubble adhesion for the flotation of quartz and apatitic minerals", Miner. Eng. **127**, 178–184 (2018).

[4] A. Azevedo, R. Etchepare, S. Calgaroto, and J. Rubio, "Aqueous dispersions of nanobubbles: Generation, properties and features", Miner. Eng. **94**, 29–37 (2016).

[5] R. J. Price, D. M. Skyba, S. Kaul, and T. C. Skalak, "Delivery of colloidal particles and red blood cells to tissue through microvessel ruptures created by targeted microbubble destruction with ultrasound", Circulation **98**, 1264–1267 (1998).

[6] R. Schlief, "Ultrasound contrast agents", Curr. Opin. Radiol. **3**, 198–207 (1991).

[7] K. Ferrara, R. Pollard, and M. Borden, "Ultrasound microbubble contrast agents: fundamentals and application to gene and drug delivery", Annu. Rev. Biomed. Eng. **9**, 415–447 (2007).

[8] J. L. Parker, P. M. Claesson, and P. Attard, "Bubbles, cavities and the long-ranged attraction between hydrophobic surfaces", J. Phys. Chem. **98**, 8468–8480 (1994).

[9] S.-T. Lou, Z.-Q. Ouyang, Y. Zhang, X.-J. Li, J. Hu, M.-Q. Li, and F.-J. Yang, "Nanobubbles on solid surface imaged by atomic force microscopy", J. Vac. Sci. Technol. B **18**, 2573–2575 (2000).

[10] D. Lohse and X. Zhang, "Surface nanobubble and surface nanodroplets", Rev. Mod. Phys. **87**, 981–1035 (2015).

[11] B. H. Tan, H. An, and C.-D. Ohl, "Stability of surface and bulk nanobubbles", Curr. Opin. Colloid Interface Sci. 101428 (2021).

[12] P. E. Theodorakis and Z. Che, "Surface nanobubbles: Theory, simulation, and experiment. a review", Adv. Colloid Interface Sci. **272**, 101995 (2019).

[13] P. Attard, "The stability of nanobubbles", Europ. Phys. J. Spec. Topics 1–22 (2013).

[14] P. S. Epstein and M. S. Plesset, "On the stability of gas bubbles in liquid-gas solutions", J. Chem. Phys. **18**, 1505–1509 (1950).

[15] X. H. Zhang, G. Li, N. Maeda, and J. Hu, "Removal of induced nanobubbles from water/graphite interfaces by partial degassing", Langmuir **22**, 9238–9243 (2006).

[16] E. N. Harvey, D. K. Barnes, W. D. McElroy, A. H. Whiteley, D. C. Pease, and K. W. Cooper, "Bubble formation in animals. i. physical factors", J. Cell. Comp. Physio. **24**, 1–22 (1944).

[17] A. Agrawal, J. Park, D. Y. Ryu, P. T. Hammond, T. P. Russell, and G. H. McKinley, "Controlling the location and spatial extent of nanobubbles using hydrophobically nanopatterned surfaces", Nano Lett. **5**, 1751–1756 (2005).

[18] A. Checco, T. Hofmann, E. DiMasi, C. T. Black, and B. M. Otto, "Morphology of air nanobubbles trapped at hydrophobic nanopatterned surfaces", Nano Lett. **10**, 1354–1358 (2010).

[19] D. Lohse and X. Zhang, "Pinning and gas oversaturation imply stable single surface nanobubble", Phys. Rev. E **91**, 031003(R) (2015).

[20] Y. O. Popov, "Evaporative deposition patterns: Spatial dimensions of the deposit", Phys. Rev. E **71**, 036313 (2005).

[21] G. Baffou and R. Quidant, "Nanoplasmonics for chemistry", Chem. Soc. Rev. **43**, 3898–3907 (2014).

[22] S. Baral, A. J. Green, M. Y. Livshits, A. O. Govorov, and H. H. Richardson, "Comparison of vapor formation of water at the solid/water interface to colloidal solutions using optically excited gold nanostructures", ACS Nano **8**, 1439–1448 (2014).

[23] M. T. Carlson, A. J. Green, and H. H. Richardson, "Superheating water by cw excitation of gold nanodots", Nano Lett. **12**, 1534–1537 (2012).

[24] G. Baffou, J. Polleux, H. Rigneault, and S. Monneret, "Super-heating and micro-bubble generation around plasmonic nanoparticles under cw illumination", J. Phys. Chem. C **118**, 4890–4898 (2014).

[25] Y. Wang, M. E. Zaytsev, G. Lajoinie, H. L. The, J. C. T. Eijkel, A. van den Berg, M. Versluis, B. M. Weckhuysen, X. Zhang, H. J. W. Zandvliet, and et al., "Giant and explosive plasmonic bubbles by delayed nucleation", Proc. Natl. Acad. Sci. U.S.A. **115**, 7676–7681 (2018).

[26] H.-L. Liu, C.-H. Fan, C.-Y. Ting, and C.-K. Yeh, "Combining microbubbles and ultrasound for drug delivery to brain tumors: Current progress and overview", Theranostics **4**, 432–444 (2014).

[27] Q. Fan, W. Hu, and A. T. Ohta, "Laser-induced microbubble poration of localized single cells", Lab Chip **14**, 1572–1578 (2014).

[28] J. Shao, M. Xuan, L. Dai, T. Si, J. Li, and Q. He, "Near-infrared-activated nanocalorifiers in microcapsules: Vapor bubble generation for *In Vivo* enhanced cancer therapy", Angew. Chem. Int. Ed. **54**, 12782–12787 (2015).

[29] S. Y. Emelianov, P.-C. Li, and M. O'Donnell, "Photoacoustics for molecular imaging and therapy", Phys. Today **62**, 34–39 (2009).

[30] D. Lapotko, "Plasmonic nanoparticle-generated photothermal bubbles and their biomedical applications", Nanomedicine **4**, 813–845 (2009).

[31] C. Zhao, Y. Xie, Z. Mao, Y. Zhao, J. Rufo, S. Yang, F. Guo, J. D. Mai, and T. J. Huang, "Theory and experiment on particle trapping and manipulation via optothermally generated bubbles", Lab Chip **14**, 384–391 (2014).

[32] Y. Xie and C. Zhao, "An optothermally generated surface bubble and its applications", Nanoscale **9**, 6622–6631 (2017).

[33] F. Tantussi, G. C. Messina, R. Capozza, M. Dipalo, L. Lovato, and F. A. De, "Long-range capture and delivery of water-dispersed nano-objects by microbubbles generated on 3d plasmonic surfaces.", Acs Nano **12**, 4116–4122 (2018).

[34] J. R. Adleman, D. A. Boyd, D. G. Goodwin, and D. Psaltis, "Heterogenous catalysis mediated by plasmon heating", Nano Lett. **9**, 4417–4423 (2009).

[35] J. Lombard, T. Biben, and S. Merabia, "Kinetics of nanobubble generation around overheated nanoparticles", Phys. Rev. Lett. **112**, 105701 (2014).

[36] J. Lombard, T. Biben, and S. Merabia, "Nanobubbles around plasmonic nanoparticles: Thermodynamic analysis", Phys. Rev. E **91**, 043007 (2015).

[37] S. Maheshwari, M. van der Hoef, A. Prosperetti, and D. Lohse, "Dynamics of formation of a vapor nanobubble around a heated nanoparticle", J. Phys. Chem. C **122**, 20571–20580 (2018).

[38] J. Lombard, T. Biben, and S. Merabia, "Ballistic heat transport in laser generated nano-bubbles", Nanoscale **8**, 14870–14876 (2016).

[39] M. E. Zaytsev, G. Lajoinie, Y. Wang, D. Lohse, H. J. W. Zandvliet, and X. Zhang, "Plasmonic bubbles in n-alkanes", J. Phys. Chem. C **122**, 28375–28381 (2018).

[40] M. Detert, B. Zeng, Y. Wang, H. L. The, H. J. W. Zandvliet, and D. Lohse, "Plasmonic bubble nucleation in binary liquids", J. Phys. Chem. C **124**, 2591–2597 (2020).

[41] Z. Xing, J. Wang, H. Ke, B. Zhao, X. Yue, Z. Dai, and J. Liu, "The fabrication of novel nanobubble ultrasound contrast agent for potential tumor imaging.", Nanotechnology **21**, 145607 (2010).

[42] S. Liu, J. Duvigneau, and G. J. Vancso, "Nanocellular polymer foams as promising high performance thermal insulation materials", Eur. Polym. J. **65**, 33 – 45 (2015).

[43] Y. Wang, B. Bhushan, and X. Zhao, "Nanoindents produced by nanobubbles on ultrathin polystyrene films in water", Nanotechnology **20**, 045301 (2009).

[44] C. Huang, J. Jiang, M. Lu, L. Sun, E. I. Meletis, and Y. Hao, "Capturing Electrochemically Evolved Nanobubbles by Electroless Deposition. A Facile Route to the Synthesis of Hollow Nanoparticles", Nano Lett. **9**, 4297–4301 (2009).

[45] L. Gao, G.-X. Ni, Y. Liu, B. Liu, A. H. Castro Neto, and K. P. Loh, "Face-to-face transfer of wafer-scale graphene films", Nature **505**, 190–194 (2014).

[46] R. P. Berkelaar, E. Dietrich, G. A. M. Kip, E. S. Kooij, H. J. W. Zandvliet, and D. Lohse, "Exposing nanobubble-like objects to a degassed environment", Soft Matter **10**, 4947–4955 (2014).

[47] J. Yang, J. Duan, D. Fornasiero, and J. Ralston, "Very small bubble formation at the solid-water interface", J. Phys. Chem. B **107**, 6139–6147 (2003).

[48] X. H. Zhang, A. Quinn, and W. A. Ducker, "Nanobubbles at the interface between water and a hydrophobic solid", Langmuir **24**, 4756–4764 (2008).

[49] X. Zhang, D. Y. C. Chan, D. Wang, and N. Maeda, "Stability of Interfacial Nanobubbles", Langmuir **29**, 1017–1023 (2013).

[50] Y. Liu and X. Zhang, "A unified mechanism for the stability of surface nanobubbles: Contact line pinning and supersaturation", J. Chem. Phys. **141**, 134702 (2014).

[51] J. H. Weijs and D. Lohse, "Why Surface Nanobubbles Live for Hours", Phys. Rev. Lett. **110**, 054501 (2013).

[52] A. A. Atchley and A. Prosperetti, "The crevice model of bubble nucleation", J. Acoust. Soc. Am. **86**, 1065–1084 (1989).

[53] B. M. Borkent, S. Gekle, A. Prosperetti, and D. Lohse, "Nucleation threshold and deactivation mechanisms of nanoscopic cavitation nuclei", Phys. Fluids **21**, 102003 (2009).

[54] N. Bremond, M. Arora, C. D. Ohl, and D. Lohse, "Controlled multibubble surface cavitation", Phys. Rev. Lett. **96**, 224501 (2006).

[55] F. Caupin and E. Herbert, "Cavitation in water: a review", C. R. Phys. **7**, 1000–1017 (2006).

[56] E. Herbert, S. b. Balibar, and F. Caupin, "Cavitation pressure in water", Phys. Rev. E **74**, 041603 (2006).

[57] X. Zhang, H. Lhuissier, O. R. Enriquez, C. Sun, and D. Lohse, "Deactivation of Microbubble Nucleation Sites by Alcohol-Water Exchange", Langmuir **29**, 9979–9984 (2013).

[58] O. R. Enriquez, C. Sun, D. Lohse, A. Prosperetti, and D. van der Meer, "The quasi-static growth of CO_2 bubbles", J. Fluid Mech. **741**, R1 (2014).

[59] S. R. German, X. Wu, H. An, V. S. J. Craig, T. L. Mega, and X. Zhang, "Interfacial nanobubbles are leaky: Permeability of the gas/water interface", ACS Nano **8**, 6193–6201 (2014).

[60] N. Ishida, T. Inoue, M. Miyahara, and K. Higashitani, "Nano bubbles on a hydrophobic surface in water observed by tapping-mode atomic force microscopy", Langmuir **16**, 6377–6380 (2000).

[61] R. P. Berkelaar, J. R. T. Seddon, H. J. W. Zandvliet, and D. Lohse, "Temperature dependence of surface nanobubbles", Chem. Phys. Chem. **13**, 2213–2217 (2012).

[62] X. Cui, C. Shi, L. Xie, J. Liu, and H. Zeng, "Probing interactions between air bubble and hydrophobic polymer surface: Impact of solution salinity and interfacial nanobubbles", Langmuir **32**, 11236–11244 (2016).

[63] C. Xu, S. Peng, G. G. Qiao, V. Gutowski, D. Lohse, and X. Zhang, "Nanobubble formation on a warmer substrate", Soft Matter **10**, 7857–7864 (2014).

[64] L. Bao, Z. Werbiuk, D. Lohse, and Z. Zhang, "Controlling the growth modes of femtoliter sessile droplets nucleating on chemically patterned surfaces", J. Phys. Chem. Lett. **7**, 1055–1059 (2016).

[65] L. Wang, X. Wang, L. Wang, J. Hu, C. L. Wang, B. Zhao, X. Zhang, R. Tai, M. He, and L. Chen, "Formation of surface nanobubbles on nanostructured substrates", Nanoscale **9**, 1078–1086 (2016).

[66] Y. Wang, B. Bhushan, and X. Zhao, "Improved nanobubble immobility induced by surface structures on hydrophobic surfaces", Langmuir **25**, 9328–9336 (2009).

[67] G. Reiter, "Unstable thin polymer films: rupture and dewetting processes", Langmuir **9**, 1344–1351 (1993).

[68] H. Tarábková and P. Janda, "Nanobubble assisted nanopatterning utilized for ex situ identification of surface nanobubbles", J. Phys.: Condens. Matter **25**, 184001 (2013).

[69] P. Janda, O. Frank, Z. Bastl, M. Klementová, H. Tarábková, and L. Kavan, "Nanobubble-assisted formation of carbon nanostructures on basal plane highly ordered pyrolytic graphite exposed to aqueous media", Nanotechnology **21**, 095707 (2010).

[70] J. H. Weijs, B. Andreotti, and J. H. Snoeijer, "Elasto-capillarity at the nanoscale: on the coupling between elasticity and surface energy in soft solids", Soft Matter **9**, 8494–8503 (2013).

[71] H. R. Brown and T. P. Russell, "Entanglements at polymer surfaces and interfaces", Macromolecules **29**, 798–800 (1996).

[72] H. Meyer, T. Kreer, A. Cavallo, J. Wittmer, and J. Baschnagel, "On the dynamics and disentanglement in thin and two-dimensional polymer films", Eur. Phys. J. Special Topics **141**, 167–172 (2007).

[73] L. Si, M. V. Massa, K. Dalnoki-Veress, H. R. Brown, and R. A. Jones, "Chain entanglement in thin freestanding polymer films", Phys. Rev. Lett. **94**, 127801 (2005).

[74] J.-H. Lee, J. Y. Chung, and C. M. Stafford, "Effect of confinement on stiffness and fracture of thin amorphous polymer films", ACS Macro Lett. **1**, 122–126 (2012).

[75] B. Bhushan, Y. Wang, and A. Maali, "Coalescence and movement of nanobubbles studied with tapping mode AFM and tip-bubble interaction analysis", J. Phys.: Condens. Matt. **20**, 485004 (2008).

[76] Y. Wang, H. Wang, S. Bi, and B. Guo, "Automatic morphological characterization of nanobubbles with a novel image segmentation method and its application in the study of nanobubble coalescence", Beilstein J. Nanotech. **6**, 952–963 (2015).

[77] Y. Wang, H. Wang, S. Bi, and B. Guo, "Nano-wilhelmy investigation of dynamic wetting properties of afm tips through tip-nanobubble interaction:", Sci. Rep. **6**, 30021 (2016).

[78] B. M. Borkent, S. de Beer, F. Mugele, and D. Lohse, "On the shape of surface nanobubbles", Langmuir **26**, 260–268 (2010).

[79] D. Li and X. Zhao, "Micro and nano bubbles on polystyrene film/water interface", Colloids Surf. A **459**, 128–135 (2014).

[80] B. Song, W. Walczyk, and H. Schönherr, "Contact angles of surface nanobubbles on mixed self-assembled monolayers with systematically varied macroscopic wettability by atomic force microscopy", Langmuir **27**, 8223–8232 (2011).

[81] M. Chappell and S. Payne, "A physiological model of the release of gas bubbles from crevices under decompression", Respir. Physiol. Neurobiol **153**, 166–180 (2006).

[82] M. A. Chappell and S. J. Payne, "The effect of cavity geometry on the nucleation of bubbles from cavities", J. Acoust. Soc. Am. **121**, 853–862 (2007).

[83] T. M. Schutzius, S. Jung, T. Maitra, G. Graeber, M. Köhme, and D. Poulikakos, "Spontaneous droplet trampolining on rigid superhydrophobic surfaces", Nature **527**, 82–85 (2015).

[84] F. Geyer, C. Schönecker, H.-J. Butt, and D. Vollmer, "Enhancing co2 capture using robust superomniphobic membranes", Adv. Mater **29**, 1603524 (2017).

[85] P. Papadopoulos, D. Vollmer, and H.-J. Butt, "Long-term repellency of liquids by superoleophobic surfaces", Phys. Rev. Lett. **117**, 046102 (2016).

[86] F. Schellenberger, N. Encinas, D. Vollmer, and H.-J. Butt, "How water advances on superhydrophobic surfaces", Phys. Rev. Lett. **116**, 096101 (2016).

[87] I. Devic, G. Soligno, M. Dijkstra, R. v. Roij, X. Zhang, and D. Lohse, "Sessile nanodroplets on elliptical patches of enhanced lyophilicity", Langmuir **33**, 2744–2749 (2017).

[88] B. H. Tan, H. An, and C. D. Ohl, "Resolving the pinning force of nanobubbles with optical microscopy.", Phys. Rev. Lett **118**, 054501 (2017).

[89] R. P. Berkelaar, P. Bampoulis, E. Dietrich, H. P. Jansen, X. Zhang, E. S. Kooij, D. Lohse, and H. J. W. Zandvliet, "Water-induced blister formation in a thin film polymer", Langmuir **31**, 1017–1025 (2015).

[90] T. Lee, E. Charrault, and C. Neto, "Interfacial slip on rough, patterned and soft surfaces: A review of experiments and simulations", Adv. Colloid Interface Sci. **210**, 21 – 38 (2014).

[91] Y. Su, B. Ji, K. Zhang, H. Gao, Y. Huang, and K. Hwang, "Nano to micro structural hierarchy is crucial for stable superhydrophobic and water-repellent surfaces", Langmuir **26**, 4984–4989 (2010).

[92] J. Zakzeski, P. C. A. Bruijnincx, A. L. Jongerius, and B. M. Weckhuysen, "The Catalytic Valorization of Lignin for the Production of Renewable Chemicals", Chem. Rev. **110**, 3552–3599 (2010).

[93] J. Luo, J.-H. Im, M. T. Mayer, M. Schreier, M. K. Nazeeruddin, N.-G. Park, S. D. Tilley, H. J. Fan, and M. Grätzel, "Water photolysis at 12.3% efficiency via perovskite photovoltaics and earth-abundant catalysts", Science **345**, 1593–1596 (2014).

[94] S. Maheshwari, M. Hoef, R. R. Javier, and D. Lohse, "Leakiness of pinned neighboring surface nanobubbles induced by strong gas surface interaction", Acs Nano **12**, 2603–2609 (2018).

[95] L. Zhang, Y. Zhang, X. Zhang, Z. Li, G. Shen, M. Ye, C. Fan, H. Fang, and J. Hu, "Electrochemically controlled formation and growth of hydrogen nanobubbles", Langmuir **22**, 8109–8113 (2006).

[96] H. E. Newton, W. D. Mcelroy, A. H. Whiteley, G. H. Warren, and D. C. Pease, "Bubble formation in animals. iii. an analysis of gas tension and hydrostatic pressure in cats", J. Cell. Comp. Physiol. **24**, 117–132 (1944).

[97] A. A. Atchley and A. Prosperetti, "Nucleation of acoustic cavitation from a gasfilled crevice", J. Acoust. Soc. Am. **79**, S46–S46 (1986).

[98] S. Peng, T. L. Mega, and X. Zhang, "Collective effects in microbubble growth by solvent exchange.", Langmuir **32**, 11265–11272 (2016).

[99] Y. Wang, X. Li, S. Ren, A. H. Tedros, L. Yang, and D. Lohse, "Entrapment of interfacial nanobubbles on nano-structured surfaces.", Soft Matter **13**, 5381–5388 (2017).

[100] K. Langley, E. Li, I. Vakarelski, and S. Thoroddsen, "The air entrapment under a drop impacting on a nanorough surface", Soft Matter **14**, 7586–7596 (2018).

[101] Y. Zhang, C. Liu, and D. C. Whalley, "The impact of substrate temperature on the size and aspect ratio of inkjet-dissolved via holes in thin poly(4-vinyl phenol) dielectric layers", Appl. Phys. Lett. **102**, 103303 (2013).

[102] E. Bonaccurso, H. J. Butt, B. Hankeln, and B. Niesenhaus, "Fabrication of microvessels and microlenses from polymers by solvent droplets", Appl. Phys. Lett **86**, 124101 (2005).

[103] F. Li, Z. Wang, S. Huang, Y. Pan, and X. Zhao, "Flexible, durable, and unconditioned superoleophobic/superhydrophilic surfaces for controllable transport and oil-water separation", Adv. Funct. Mater. **28**, 1706867 (2018).

[104] C. W. Danelle Beattie, Kok Hou Wong, "Honeycomb structured porous films from polypyrrole containing block copolymers prepared via raft polymerization as a scaffold for cell growth", Biomacromolecules **7**, 1072–1082 (2006).

[105] C. Liu, J. Liu, D. Gao, M. Ding, and J. M. Lin, "Fabrication of microwell arrays based on two-dimensional ordered polystyrene microspheres for high-throughput single-cell analysis", Anal. Chem. **82**, 9418–9424 (2010).

[106] F. Chen, S. Mao, H. Zeng, S. Xue, J. Yang, H. Nakajima, J. M. Lin, K. Uchiyama, and A. Chem, "Inkjet nanoinjection for high-thoughput chemiluminescence immunoassay on multicapillary glass plate.", Anal. Chem. **85**, 7413–7418 (2013).

[107] C. I. Aguirre, E. Reguera, and A. Stein, "Tunable colors in opals and inverse opal photonic crystals", Adv. Funct. Mater. **21**, 2565–2578 (2010).

[108] Y. Vasquez, M. Kolle, L. Mishchenko, B. D. Hatton, and J. Aizenberg, "Three phase co assembly in situ incorporation of nanoparticles into tunable, highly ordered, porous silica films", ACS Photonics **1**, 53–60 (2014).

[109] S. F. Jones, G. M. Evans, and K. P. Galvin, "Bubble nucleation from gas cavities: a review", Adv. Colloid Interface Sci **80**, 27 – 50 (1999).

[110] X. Zhang, J. Wang, L. Bao, E. Dietrich, R. C. A. van der Veen, S. Peng, J. Friend, H. J. W. Zandvliet, L. Yeo, and D. Lohse, "Mixed mode of dissolving immersed microdroplets at a solid-water interface", Soft Matter **11**, 1889–1900 (2015).

[111] L. Bao, V. Spandan, Y. Yang, B. Dyett, R. Verzicco, D. Lohse, and X. Zhang, "Flow-induced dissolution of femtoliter surface droplet arrays.", Lab Chip **18**, 1066–1074 (2018).

[112] X. Zhu, R. Verzicco, X. Zhang, and D. Lohse, "Diffusive interaction of multiple surface nanobubbles: shrinkage, growth, and coarsening", Soft Matter **14**, 2006–2014 (2018).

[113] S. Michelin, E. Guerin, and E. Lauga, "Collective dissolution of microbubbles", Phys. Rev. Fluid **3**, 043601 (2018).

[114] K. Yasui, T. Tuziuti, W. Kanematsu, and K. Kato, "Dynamic equilibrium model for a bulk nanobubble and a microbubble partly covered with hydrophobic material", Langmuir **32**, 11101–11110 (2016).

[115] M. Hoorfar, M. A. Kurz, Z. Policova, M. L. Hair, and A. W. Neumann, "Do polysaccharides such as dextran and their monomers really increase the surface tension of water?", Langmuir **22**, 52–56 (2006).

[116] X. Liu, L. Bao, M. Dipalo, F. De Angelis, and X. Zhang, "Formation and dissolution of microbubbles on highly-ordered plasmonic nanopillar arrays", Sci. Rep. **5**, 18515 (2015).

[117] G. Baffou and R. Quidant, "Thermo-plasmonics: Using metallic nanostructures as nano-sources of heat", Laser Photonics Rev. **7**, 171–187 (2013).

[118] S. Boriskina, H. Ghasemi, and G. Chen, "Plasmonic materials for energy: From physics to applications", Mater. Today **16**, 375–386 (2013).

[119] H. Ghasemi, G. Ni, A. M. Marconnet, J. Loomis, S. Yerci, N. Miljkovic, and G. Chen, "Solar steam generation by heat localization", Nat. Commun. **5**, 2041–1723 (2014).

[120] A. Guo, Y. Fu, G. Wang, and X. Wang, "Diameter effect of gold nanoparticles on photothermal conversion for solar steam generation", RSC Adv. **7**, 4815–4824 (2017).

[121] M. Krishnan, J. Park, and D. Erickson, "Optothermorheological Flow Manipulation", Opt. Lett. **34**, 1976–1978 (2009).

[122] K. Zhang, A. Jian, X. Zhang, Y. Wang, Z. Li, and H. Y. Tam, "Laser-induced thermal bubbles for microfluidic applications", Lab Chip **11**, 1389–1395 (2011).

[123] Y. Wang, M. E. Zaytsev, H. L. The, J. C. T. Eijkel, H. J. W. Zandvliet, X. Zhang, and D. Lohse, "Vapor and gas-bubble growth dynamics around laser-irradiated, water-immersed plasmonic nanoparticles", ACS Nano **11**, 2045–2051 (2017).

[124] S.-C. Yang, W.-J. Fischer, and T.-L. Yang, "Size-Controllable Micro-Bubble Generation Using a Nanoimprinted Plasmonic Nanopillar Array Absorber in the Near-Infrared Region", Appl. Phys. Lett. **108**, 183105 (2016).

[125] X. Li, Y. Wang, B. Zeng, Y. Li, H. Tan, H. J. W. Zandvliet, X. Zhang, and D. Lohse, "Entrapment and Dissolution of Microbubbles Inside Microwells", Langmuir **34**, 10659–10667 (2018).

[126] A. Prosperetti, "Vapor bubbles", Ann. Rev. Fluid Mech. **49**, 221–248 (2017).

[127] O. Neumann, A. S. Urban, J. Day, S. Lal, P. Nordlander, and N. J. Halas, "Solar vapor generation enabled by nanoparticles", ACS Nano **7**, 42–49 (2013).

[128] Z. Fang, Y. R. Zhen, O. Neumann, A. Polman, F. J. Garcia de Abajo, P. Nordlander, and N. J. Halas, "Evolution of light-induced vapor generation at a liquid-immersed metallic nanoparticle", Nano Lett. **13**, 1736–1742 (2013).

[129] A. Polman, "Solar Steam Nanobubbles", ACS Nano **7**, 15–18 (2013).

[130] E. Lukianova-Hleb, Y. Hu, L. Latterini, L. Tarpani, S. Lee, R. A. Drezek, J. H. Hafner, and D. O. Lapotko, "Plasmonic nanobubbles as transient vapor nanobubbles generated around plasmonic nanoparticles", ACS Nano **4**, 2109–2123 (2010).

[131] L. Hou, M. Yorulmaz, N. R. Verhart, and M. Orrit, "Explosive formation and dynamics of vapor nanobubbles around a continuously heated gold nanosphere", New J. Phys. **17**, 013050 (2015).

[132] J. Lombard, T. Biben, and S. Merabia, "Threshold for vapor nanobubble generation around plasmonic nanoparticles", J. Phys. Chem. C **121**, 15402–15415 (2017).

[133] H. Le-The, E. Berenschot, R. M. Tiggelaar, N. R. Tas, A. van den Berg, and J. C. T. Eijkel, "Shrinkage control of photoresist for large-area fabrication of sub-30 nm periodic nanocolumns", Adv. Mater. Technol. **2**, 1600238 (2017).

[134] Y. Wang, Z. Zhang, H. Wang, and S. Bi, "Segmentation of the clustered cells with optimized boundary detection in negative phase contrast images", Plos One **10**, e0130178 (2015).

[135] Y. Wang, T. Lu, X. Li, and H. Wang, "Automated image segmentation-assisted flattening of atomic force microscopy images", Beilstein J. Nanotech. **9**, 975–985 (2018).

[136] V. P. Skripov and P. A. Pavlov, "Explosive boiling of liquids and fluctuation nucleus formation", High Temp. **8**, 833–839 (1970).

[137] M. Blander and J. L. Katz, "Bubble nucleation in liquids", AIChE J. **21**, 833–848 (1975).

[138] S. E. Puchinskis and P. V. Skripov, "The attainable superheat: From simple to polymeric liquids", Int. J. Thermophys. **22**, 1755–1768 (2001).

[139] X. Li, Y. Wang, M. E. Zaytsev, G. Lajoinie, H. L. The, J. G. Bomer, J. C. T. Eijkel, H. J. W. Zandvliet, X. Zhang, and D. Lohse, "Plasmonic bubble nucleation and growth in water: effect of dissolved air", J. Phys. Chem. C **123**, 23586–23593 (2019).

[140] B. P. Dyett, M. Li, H. Zhao, and X. Zhang, "Plasmonic nanobubbles in "armored" surface nanodroplets", J. Phys. Chem. C **123**, 29866–29874 (2019).

[141] M. E. Zaytsev, Y. Wang, Y. Zhang, G. Lajoinie, X. Zhang, A. Prosperetti, H. J. W. Zandvliet, and D. Lohse, "Gas-vapor interplay in plasmonic bubble shrinkage", J. Phys. Chem. C **124**, 5861–5869 (2020).

[142] D. Lohse and X. Zhang, "Physicochemical hydrodynamics of droplets out of equilibrium", Nat. Rev. Phys. **2**, 426–443 (2020).

[143] Y. Li, C. Diddens, A. Prosperetti, K. L. Chong, X. Zhang, and D. Lohse, "Bouncing oil droplet in a sratified liquid and its sudden death", Phys. Rev. Lett. **122**, 154502 (2019).

[144] W. L. Tong, M. K. Tan, J. K. Chin, K. S. Ong, and Y. M. Hung, "Coupled effects of hydrophobic layer and vibration on thermal efficiency of two-phase closed thermosyphons", RSC Adv. **5**, 10332–10340 (2015).

[145] H. Oguz and A. Prosperetti, "Dynamics of bubble-growth and detachment from a needle", J. Fluid Mech. **257**, 111–145 (1993).

[146] P. Lv, H. Le The, J. Eijkel, A. Van den Berg, X. Zhang, and D. Lohse, "Growth and detachment of oxygen bubbles induced by gold-catalyzed decomposition of hydrogen peroxide", J. Phys. Chem. C **121**, 20769–20776 (2017).

[147] M. A. Kalbassi and M. W. Biddulph, "Surface tension of mixtures at their boiling points", J. Chem. Eng. Data **33**, 473–476 (1988).

[148] G. Vazquez, E. Alvarez, and J. M. Navaza, "Surface tension of alcohol water + water from 20 degrees to 50 degrees", J. Chem. Eng. Data **40**, 611–614 (1995).

[149] Y. Yonemoto, S. Suzuki, S. Uenomachi, and T. Kunugi, "Sliding behaviour of water-ethanol mixture droplets on inclined low-surface-energy solid", Int. J. Heat Mass Transfer **120**, 1315–1324 (2018).

[150] C. Liu, E. Bonaccurso, and H.-J. Butt, "Evaporation of sessile water/ethanol drops in a controlled environment", Phys. Chem. Chem. Phys. **10**, 7150–7157 (2008).

[151] A. K. H. Cheng, D. M. Soolaman, and H.-Z. Yu, "Evaporation of microdroplets of ethanol-water mixtures on gold surfaces modified with self-assembled monolayers", J. Phys. Chem. B **110**, 11267–11271 (2006).

[152] C. H. Ooi, E. Bormashenko, A. V. Nguyen, G. M. Evans, D. V. Dao, and N.-T. Nguyen, "Evaporation of ethanol-water binary mixture sessile liquid marbles", Langmuir **32**, 6097–6104 (2016).

[153] K. Sefiane, L. Tadrist, and M. Douglas, "Experimental study of evaporating water-ethanol mixture sessile drop: influence of concentration", Int. J. Heat Mass Transf. **46**, 4527–4534 (2003).

[154] Z. Wang, X.-F. Peng, A. S. Mujumdar, A. Su, and D.-J. Lee, "Evaporation of ethanol-water mixture drop on horizontal substrate", Dry. Technol. **26**, 806–810 (2008).

[155] Y. Yonemoto and T. Kunugi, "Experimental and theoretical investigation of contact-angle variation for water-ethanol mixture droplets on a low-surface-energy solid", Int. J. Heat Mass Transf. **96**, 614–626 (2016).

[156] E. Dietrich, M. Rump, P. Lv, E. S. Kooij, H. J. W. Zandvliet, and D. Lohse, "Segregation in dissolving binary-component sessile droplets", J. Fluid Mech. **812**, 349–369 (2017).

[157] M. E. R. Shanahan, "Simple theory of stick-slip wetting hysteresis", Langmuir **11**, 1041–1043 (1995).

[158] J. M. Stauber, S. K. Wilson, B. R. Duffy, and K. Sefiane, "On the lifetimes of evaporating droplets", J. Fluid Mech. **744**, R2 (2014).

[159] J. M. E. Escobar, E. Dietrich, S. Arscott, H. J. W. Zandvliet, X. Zhang, and D. Lohse, "Zipping-depinning: dissolution of droplets on micropatterned concentric rings", Langmuir **34**, 5396–5402 (2018).

[160] J. M. E. Escobar, D. Garcia-Gonzalez, I. Devic, X. Zhang, and D. Lohse, "Morphology of evaporating sessile microdroplets on lyophilic elliptical patches", Langmuir **35**, 2099–2105 (2019).

[161] F. Barr-David and B. F. Dodge, "Vapor-liquid equilibrium at high pressures. the systems ethanol-water and 2-propanol-water.", J. Chem. Eng. Data **4**, 107–121 (1959).

[162] B. E. Wyslouzil and J. Woelk, "Overview: Homogeneous nucleation from the vapor phase-The experimental science", J. Chem. Phys. **145**, 26–31 (2016).

[163] Y. Liu and S. J. Dillon, "In situ observation of electrolytic h_2 evolution adjacent to gold cathodes", Chem. Comm. **50**, 1761–1763 (2014).

[164] T. Jollans and M. Orrit, "Explosive, oscillatory, and leidenfrost boiling at the nanoscale", Phys. Rev. E **99**, 063110 (2019).

[165] B. Zeng, Y. Wang, M. E. Zaytsev, C. Xia, H. J. Zandvliet, and D. Lohse, "Giant plasmonic bubbles nucleation under different ambient pressures", Phys. Rev. E **102**, 063109 (2020).

[166] V. G. Levich, *Physicochemical hydrodynamics* (Prentice Hall, Englewood Cliffs) (1962).

[167] X. Li, Y. Wang, B. Zeng, M. Detert, A. Prosperetti, H. J. W. Zandvliet, and D. Lohse, "Plasmonic microbubble dynamics in binary liquids", J. Phys. Chem. Lett. **11**, 8631–8637 (2020).

[168] S. Vitale and J. Katz, "Liquid droplet dispersions formed by homogeneous liquid-liquid nucleation: "the ouzo effect"", Langmuir **19**, 4105–4110 (2003).

[169] H. Tan, C. Diddens, P. Lv, J. G. M. Kuerten, X. Zhang, and D. Lohse, "Evaporation-triggered microdroplet nucleation and the four life phases of an evaporating ouzo drop", Proc. Natl. Acad. Sci. U. S. A. **113**, 8642–8647 (2016).

[170] F. Ganachaud and J. Katz, "Nanoparticles and nanocapsules created using the Ouzo effect: spontaneous emulsification as an alternative to ultrasonic and high-shear devices", Chem. Phys. Chem **6**, 209–216 (2005).

[171] H. Tan, C. Diddens, M. Versluis, H.-J. Butt, D. Lohse, and X. Zhang, "Self-wrapping of an ouzo drop induced by evaporation on a superamphiphobic surface", Soft Matter **13**, 2749–2759 (2017).

[172] H. Tan, C. Diddens, A. A. Mohammed, J. Li, M. Versluis, X. Zhang, and D. Lohse, "Microdroplet nucleation by dissolution of a multicomponent drop in a host liquid", J. Fluid Mech. **870**, 217–246 (2019).

[173] D. Kashchiev, *Nucleation* (Elsevier, Oxford) (2000).

[174] S. Ayuba, D. Suh, K. Nomura, T. Ebisuzaki, and K. Yasuoka, "Kinetic analysis of homogeneous droplet nucleation using large-scale molecular dynamics simulations", J. Chem. Phys. **149**, 044504 (2018).

[175] H. Vehkamäki, *Classical nucleation theory in multicomponent systems* (Springer, Heidelberg) (2006).

[176] C. Sternling and L. Scriven, "Interfacial turbulence: hydrodynamic instability and the marangoni effect", AIChE J. **5**, 514–523 (1959).

[177] E. E. Hills, M. H. Abraham, A. Hersey, and C. D. Bevan, "Diffusion coefficients in ethanol and in water at 298 k: Linear free energy relationships", Fluid Phase Equilib. **303**, 45–55 (2011).

[178] S. Michelin, E. Lauga, and D. Bartolo, "Spontaneous autophoretic motion of isotropic particles", Phys. Fluids **25**, 061701 (2013).

[179] Y. Chen, K. L. Chong, L. Liu, R. Verzicco, and D. Lohse, "Instabilities driven by diffusio-phoretic flow on catalytic surfaces", J. Fluid Mech. **in press** (2021).

[180] H. Schlichting and J. Kestin, *Boundary layer theory*, volume 121 (Springer, New York: McGraw-Hill) (1961).

[181] R. Verzicco and P. Orlandi, "A finite-difference scheme for three-dimensional incompressible flows in cylindrical coordinates", J. Comput. Phys. **123**, 402–414 (1996).

[182] V. Spandan, V. Meschini, R. Ostilla-Mónico, D. Lohse, G. Querzoli, M. D. de Tullio, and R. Verzicco, "A parallel interaction potential approach coupled with the immersed boundary method for fully resolved simulations of deformable interfaces and membranes", J. Comput. Phys. **348**, 567–590 (2017).

Summary

Bubbles are widely present in many natural and industrial processes. Understanding the nucleation mechanism and dynamics of the bubbles is essential for exploiting relevant applications in material engineering, microfluidics, catalysis and electrolysis and many others. In this thesis we focused on surface micro/nanobubbles on structured surfaces, and plasmonic bubbles in water with various gas saturations, binary liquids and ternary liquids.

In Chapter 2, we start with the spontaneous nucleation of nanobubbles (NBs) on nanostructured surfaces. Through in-situ AFM measurements, we find three categories of air entrapment, namely protruding NBs at nanopits with widths in between 50-100 nm, planar NBs at nanopits with widths of 100-150 nm, and no air entrapment at nanopits with a diameter larger than 150 nm. The size and contact angle of the protruding NBs linearly increases with increasing nanopit width. We reveal that NB formation on surface nanocavities follows the crevice theory that entrapped gas pockets grow into bubbles along with the diffusion of dissolved gas from the liquid to cavities. The dependence of entrapped NBs' size and shape on that of nanopits highlights the pinning effect of the surface structures. This work provides direct evidence that surface NB nucleation originates from gas entrapment at crevices. However, the bubble entrapment dynamics remains unclear due to the limited temporal resolution of AFM.

In Chapter 3, we explore the bubble entrapment dynamics using larger surface microwells, which allows visualization with confocal microscopy with a high temporal resolution. We observed that after immersion, the microwells were initially fully covered by the entrapped microbubbles. Subsequently the entrapped microbubbles partially detach from the microwell edges and rapidly shrink to a smaller size in a constant contact angle dissolution mode. Moreover, we quantified how the flow rates and undersaturation level influence

the bubble dissolution dynamics. Results show that the flow rates have no influence on the dynamics of microbubble entrapment and dissolution, and a higher undersaturation enhances microbubble dissolution. We believe that the knowledge acquired in Chapters 2 and 3 facilitates the understanding of surface NB properties, and the controllable production of surface NBs.

In Chapter 4, we studied plasmonic microbubbles formed from vaporization of liquids due to plasmonic effects. We first investigated the effect of the dissolved gas on the early-phase giant bubble and the bubble growth in long-term. We find that lower gas concentrations leads to longer delay times τ_d, larger maximum volumes, and higher nucleation temperatures of initial giant bubbles, *i.e.* the dissolved gas facilitates bubble nucleation. Besides, the maximum volume of the initial giant bubbles linearly depends on the input energy, which suggests that the initial giant bubbles are vapor bubbles. Moreover, the diffusion-dominated long-term bubble growth is governed by the gas concentration. The radius of the bubbles grows as $R(t) \propto t^{1/3}$ for air equilibrated and air-oversaturated water.

In Chapter 5, we explored the growth dynamics of plasmonic bubbles in water-ethanol binary liquids. We find that the bubbles detach from the substrate at ethanol concentrations below 67.5%, which results from a strong downward Marangoni flow induced by selective vaporization. For ethanol concentrations in the range from 67.5% to 80%, the bubbles remain stable on the substrate but exhibit a sudden shrinkage after a delay time t_s. We reveal that the sudden shrinkage originates from the complete depinning of the bubble from the laser spot area on the sample surfaces. When $f_e \gtrsim 80\%$, the binary liquid becomes azeotropic. The bubbles exhibit a steady growth, which is similar to the behavior of a pure liquid.

In Chapter 6, we further studied plasmonic bubble nucleation in ternary liquids of ethanol-water-anethole (ouzo solution). We observed that during bubble growth anethole oil microdroplets nucleated around the bubble, and formed droplet plumes. When the ethanol-water relative weight ratio $r_{e/(e+w)}$ increases from 65.0% to 80.0% in the ternary liquids, plasmonic bubbles grow faster and more droplet plumes are emitted around the bubbles. We perform a numerical simulation to quantify the plume formation. The numerical results show that there exists a critical Marangoni number $Ma = 5 \times 10^4$, above which the symmetry of the ethanol concentration field is broken, leading to the formation of droplet plumes. The revealed Ma dependence of the maximum plume numbers in the numerical results is consistent with that in experiments.

Samenvatting

Bellen zijn alom aanwezig in veel natuurlijke en industriële processen. Inzicht in de nucleatie mechanismen en de dynamica van de bellen is essentieel voor toepassingen in onder anderen materiaalengineering, microfluïdica, katalyse en elektrolyse. In dit proefschrift hebben we ons gericht op oppervlakte micro- en nanobellen op gestructureerde oppervlakken, en plamonische bellen in water met verschillende gasconconcentraties, alsmede binaire vloeistoffen en ternaire vloeistoffen.

In hoofdstuk 2 beginnen we met de spontane nucleatie van nanobellen (NBs) op nano-gestructureerde oppervlakken. Door middel van in-situ atomic force microscopie (AFM) metingen vinden we drie categorieën van bellen, namelijk uitstekende NBs bij nanoputjes met breedtes tussen 50-100 nm, vlakke NBs bij nanoputjes met breedtes van 100-150 nm, en luchtinsluiting-loze nucleatiecentra bij nanoputjes met een diameter groter dan 150 nm. De grootte en de contacthoek van de uitstekende NBs nemen lineair toe met toenemende nanoput breedte. We tonen aan dat NB-formatie op nanoputjes aan het oppervlak de spleet-theorie volgt, waarbij ingesloten gaspockets uitgroeien tot bellen o.a. door de diffusie van opgelost gas uit de vloeistof naar de gaspockets. De afhankelijkheid van de grootte en vorm van ingesloten NB's van die van nanoputjes benadrukt het "pinning" effect van de oppervlaktestructuren. Dit werk levert direct bewijs dat NB-kiemvorming aan het oppervlak ontstaat door gasinsluiting in spleten. Echter, de dynamica van de gasbel blijft onduidelijk vanwege de beperkte tijdsresolutie van AFM.

In hoofdstuk 3, onderzoeken we de dynamiek van het vangen van luchtbellen met behulp van oppervlakte "microwells", die de visualisatie met confocale microscopie met een hoge tijdsresolutie mogelijk maakt. We zagen dat na onderdompeling, de microwells in eerste instantie volledig werden bedekt door de ingesloten microbellen. Vervolgens komen de ingesloten microbellen gedeel-

telijk los van de randen van de microwells en krimpen snel naar een kleinere afmeting in de constante-contacthoek oplossingsmodus. Bovendien hebben we gekwantificeerd hoe de stroomsnelheden en het onderverzadigingsniveau de dynamica van het oplossen van de bellen beïnvloeden. De resultaten tonen aan dat de stroomsnelheden geen invloed hebben op de dynamiek van de microbelletjes en het oplossen, een hogere onderverzadiging versnelt de oplossing van de microbelletjes. Wij zijn ervan overtuigd dat de kennis die is opgedaan in hoofdstuk 2 en 3 het begrip van oppervlakte NB eigenschappen, en de controleerbare productie van oppervlakte NBs vergemakkelijkt.

In hoofdstuk 4, bestudeerden we plasmonische microbellen gevormd door verdamping van vloeistoffen als gevolg van plasmonische effecten. We onderzochten eerst het effect van het opgeloste gas op de reuzenbel in de vroege fase en de belgroei op langere termijn. We vonden dat lagere gasconcentraties leiden tot langere vertragingstijden τ_d, grotere maximale volumes, en hogere nucleatie temperaturen van initiële reuzenbellen, d.w.z. het opgeloste gas vergemakkelijkt de kiemvorming van de bel. Bovendien hangt het maximale volume van de initiële reuzenbellen lineair af van de energie, wat suggereert dat de initiële reuzenbellen dampbellen zijn. Bovendien wordt de diffusiegedomineerde bellengroei op lange termijn beheerst door de gasconcentratie. De straal van de bellen groeit als $R(t) \propto t^{1/3}$ voor in lucht verzadigd en oververzadigd water.

In hoofdstuk 5 hebben we de groeidynamica van plasmonische bellen in binaire vloeistoffen van water en ethanol onderzocht. We vonden dat de bellen loskomen van het substraat bij ethanolconcentraties lager dan 67.5%, wat het gevolg is van een sterke neerwaartse Marangoni stroming geïnduceerd door selectieve verdamping. Voor ethanolconcentraties tussen 67.5% tot 80% blijven de bellen stabiel op het substraat, maar vertonen ze een plotselinge krimp na een vertragingstijd t_s. We ontdekten dat de plotselinge krimp veroorzaakt wordt door de volledige "depinning" van de bel uit het laserspot gebied op het sample oppervlak. Wanneer $f_e \gtrsim 80\%$, wordt de binaire vloeistof azeotropisch. De bellen vertonen een gestage groei, die vergelijkbaar is met het gedrag van een zuivere vloeistof.

In hoofdstuk 6 bestudeerden we verder plasmonische kiemvorming van bellen in ternaire vloeistoffen van ethanol-water-anethol (Ouzo oplossing). We zagen dat tijdens de groei van de bel anethol-olie microdruppels ontstonden rond de bel en dat er zich druppelpluimen vormden. Wanneer de relatieve gewichtsverhouding ethanol-water $r_e/(e + w)$ toeneemt van 65.0% tot 80.0% in de ter-

naire vloeistoffen, groeien plasmonische bellen sneller en worden er meer druppelpluimen rondom de bellen uitgestoten. We hebben een numerieke simulatie uitgevoerd om de pluimvorming van de bellen te kwantificeren. De numerieke resultaten tonen aan dat er een kritisch Marangoni getal ($Ma = 5 \times 10^4$) bestaat, waarboven de symmetrie van het ethanolconcentratieveld wordt verbroken, dit leidt tot de vorming van druppelpluimen. De bepaalde Ma afhankelijkheid van het maximum aantal pluimen in de numerieke resultaten is consistent met die in de experimenten.

Acknowledgements

Five years ago when I got the acceptance letter of my doctoral application, I was more nervous than excited about the coming long journey. Now looking back to the past years, I feel so lucky to have many people around turning this journey into beautiful memories. I would greatly thank you everyone for your numerous help and supports.

Dear *Detlef*, thank you for providing me the opportunity to study in PoF. I still remember the first time when I came to PoF for the three-months' visit in 2018. You were always patient in my influent English, immature results, and weak background in physics of fluid. In the end of the three-months' stay, you accepted me to continue researches in PoF via the double Ph.D degree programm. No words can describe how tremendous the encouragement from a great scientist is for me at that time. During my study in PoF, I learn a lot not only from your numerous comments, suggestions for scientific research, but also from your spirits of science: be precise, curious, critical and 'never too late to learn'. Your passion and concentration for science keep inspiring me, and I feel humbled and guilty that there is still much room for me to improve. Besides, I would also thank you for your motivation and good example of keeping exercise, though I am still far from catching up with you in running. I am proud of being your student, and will keep what you taught in mind in my future career all the time.

Dear *Harold*, it is my good luck to have you as my supervisor. You are always open to discussions and allow me talk about many immature opinions. I benefit a lot from your comments, discussions in our physical and online meetings. I learn how to write articles concisely when you help me to polish my papers. I am also grateful to have learned AFM in PIN and made nice measurement results there. I truly appreciate that whenever I need help, you are always there to support me. You help me so much in arrangements of

annual interview, and dealing with complex documents of TGS. If it was not you, my double Ph.D degree programm could not go smoothly as now. Great thanks to you for your continuous supports. I really enjoy the nice time with you and all my time in Netherlands.

Dear *Yuliang*, many thanks to you. How much you change my life is more than I can say. It has been seven years since the first time I visited you for my bachelor project in Jan. of 2014. I started research from '0' with you. You taught me from optical microscope/AFM operation, software programming to making presentations, writing English papers, asking scientific questions, improving sense of science and many others. I am not a very talented person, but you are a very good promoter. When I was stuck you are always there to give me courage. You always motivate me to challenge higher level and improve further. I also admire your ability to build a twenty persons' group and well-equipped labs alone in these years. Thank you for your numerous hours and days and all you did for me. The past years studying with you are the most valuable memory in my life.

Dear *Xuehua*, I am grateful for your fruitful discussions, comments and ideas. Your scientific visions and ideas are always very helpful.

Dear *Andrea*, I admire your passion and enthusiasm for science so much. Many thanks to you for all the helpful discussions and ideas.

Dear *Guillaume*, thank you for your help in teaching me DHM and other devices when I joined the group. I also truly appreciate your numerous help in our plasmonic bubble project.

Dear *Roberto*, thank you so much for your support in our joint paper on droplet plumes.

Dear *Joanita*, you are always efficient when I ask for help. Thank you so much for all your help with many paperworks and arrangements, and also your always kindness. Dear *Gert-Wim*, you can solve any problem that we had in experimental equipments. Also thanks a lot for your friendness. Dear *Bas*, thank you for all your help in ordering materials for experiments and solving computer problems. You are always friendly and patient for helping us. Dear *Martin*, thanks for your help with computer problems and always friendness. Dear *Dennis*, you are always available whenever we look for your help. Thank you so much for making our labs safe, clean and well organized.

Main collaborators:

Yanshen, thank you for teaching me experiments with confocal microscopy and many other equipments. I learned a lot from the fruitful discussions with you over the past years. I also admire your outstanding ability of learning and preciseness in research very much.

Mikhail, thank you for teaching me experiments with the high speed cameras. You are always friendly and efficient when I need help.

Huanshu, thank you for helping me around in labs, teaching me latex when I joined PoF. I learned a lot from the helpful discussions on ouzo project. Also I admire your sense of art and like the nice figures made by you very much.

Yibo, I am grateful to you for your great help on numerical simulation for our joint paper. You are always optimistic and friendly to everyone of us. All the best to you.

Steven, thanks a lot for your insightful suggestions on our droplet plume work and careful revisions of our joint paper. You have strong physical insight and are always patient and friendly to teach and help everyone. I was inspired a lot from the fruitful discussions with you.

Hai, thank you for helping make samples for plamonic bubble work. I am grateful to all your support in our plasmonic bubble project.

Marvin, you are always friendly and enthusiastic to everyone. Thanks a lot for all your help around labs and helpful discussions. Wish you all the best.

Labmates: *Ricardo, Lijun, Srinath*, thank you for helping keep our lab well organized and all nice interactions. Particularly during the partial lockdown, you are always patient and friendly to adjust the schedule for experiments. All the best to all of you.

Moreover, my special thanks to *Yaxing, Shuai, Youseff, Nayoung, Pallav, Diana, Jelle, Ellis*.

Yaxing, thank you for helping me make silicon samples and teaching me experimental devices in biolab. You are always helpful and considerate to everyone. I like your optimistic attitude towards life and work very much, and thanks a lot for all your encouragement when I was depressed in difficulties.

Shuai, I leaned a lot from your discussions, comments on cavitation bubbles. Thanks a lot for all your help.

Youseff, thank you very much for your kind and helpful discussions on tem-

perature field simulation of gold nanoparticles.

Nayoung, it is lucky to have you around during my study in PoF. You are always very considerate to me, which reminds me the enjoyable time with my sisters. I like talking with you about my researches, and any happiness or unhappiness of my life. Also thank you very much for many snacks and Korean food from you.

Pallav, thank you for helping me in labs and many helpful discussions. I am grateful to your always friendness and kindness.

Jelle, many thanks to you for the nice interactions around group, and helping me translate the summary in Dutch. Dank je wel!

Diana, you are so friendly and considerate to integrate every PoFers. I appreciate the nice interactions and enjoy talking with you very much.

Ellis, I enjoyed the time playing with you very much and thank you for helping train my badminton skills. Wish you all the best.

Chinese folks:

Luoqin, thank you for the helpful discussions when we worked in the same office. I was inspired a lot by your concentration in science. I admire your outstanding abilities in mathematics and physics, and saw the great spirit of a scientist from you.

Haoran, you are always friendly to us. We had several nice discussions on contact line dynamics. Thank you for the helpful comments and suggestions.

Jiaming, I enjoyed the conversations with you on microfluidics and bubbles. Thank you so much for the discussions and comments.

Guiquan, you are really a friendly person. Talking with you was of great fun.

Qi, thank you for your help with my computer problems. Your hard working motivates me a lot.

Rui, thanks a lot for your always patience and friendness when I ask for help. All the best to you! I also owe my great thanks to the former folks *Pengyu, Mengqi, Xiaoyan.*

I would also like to thank all former and current PoFers and PINers for a wonderful atmosphere and various activities: *Pierre, Carola, Nathan, Michiel Cayan, Jessica, Ali, Hadi, Vatsal, Farzen, Yogesh, Minkush, Chong Shen,*

Peter, Youan...My apologies if I forget to mention someone.

I would like to extend my sincere thanks to colleagues from my Chinese group: *Lihua, Shuai, Zaicheng, Lin, Chunqi, Yahya, Teddy, Max, Zhaoxin, Tongda, Chenliang, Ji, Buyun, Chengjia.*

Last but definitely not least, I express my profound gratitude to my family: my parents, my sisters and Binglin. Thank you for your endless love and support all the time.

Scientific output

Publications

- **Xiaolai Li**, Yibo Chen, Yuliang Wang, Kai Leong Chong, Harold J. W. Zandvliet, and Detlef Lohse,
  Droplet plume emission during plasmonic bubble growth in ternary liquids,
  Phys. Rev. E, 104, 025101 (2021)

- **Xiaolai Li**, Yuliang Wang, Binglin Zeng, Marvin Detert, Andrea Prosperetti, Harold J.W. Zandvliet, and Detlef Lohse,
  Plasmonic microbubble dynamics in binary liquids,
  J. Phys. Chem. Lett., 11, 8631-8637 (2020)

- **Xiaolai Li**, Yuliang Wang, Mikhail E. Zaytsev, Guillaume Lajoinie, Hai Le The, Johan G. Bomer, Jan C. T. Eijkel, Harold J. W. Zandvliet, Xuehua Zhang, and Detlef Lohse,
  Plasmonic bubble nucleation and growth in water: the effect of dissolved air,
  J. Phys. Chem. C, 123, 23586-23593 (2019)

- **Xiaolai Li**, Yuliang Wang, Binglin Zeng, Yanshen Li, Huanshu Tan, Harold J. W. Zandvliet, Xuehua Zhang, Detlef Lohse,
  Entrapment and dissolution of microbubbles inside microwells,
  Langmuir, 2018, 34, 10659-10667, 2018 (Cover story)

- Yuliang Wang, **Xiaolai Li**, Shuai Ren, Tedros A. H., Lijun Yang, Detlef Lohse,
  Entrapment of interfacial nanobubbles on nano-structured surfaces,
  Soft Matter, 13, 5381-5388, 2017 (Cover story)

- Yuliang Wang, **Xiaolai Li**, Shusheng Bi, Xiaofeng Zhu, Jinhua Liu,

3D micro-particle image modeling and its application in measurement resolution investigation for visual sensing based axial localization in an optical microscope,
Meas. Sci. Technol., 28, 015402 (2017)

- Yahya Elkarkri, **Xiaolai Li**, Binglin Zeng, Zhaoxin Lian, Ji Zhou, Yuliang Wang,
Laser photonic nanojets triggered thermoplasmonic micro/nanofabrication of polymer materials for enhanced resolution,
Nanotechnology, 32, 145301 (2021)

- Yuliang Wang, Binglin Zeng, **Xiaolai Li**, and Xuehua Zhang,
Sequential evaporation-induced formation of polymeric surface microdents via ouzo effect,
Adv. Mater. Interfaces, 6, 1900002 (2019)

- Yuliang Wang, Tongda Lu, **Xiaolai Li**, Huimin Wang,
Automated image segmentation-assisted flattening of atomic force microscopy images,
Beilstein journal of nanotechnology, 9, 975-985 (2018)

- Yuliang Wang, Tongda Lu, **Xiaolai Li**, Shuai Ren, Shusheng Bi,
Robust nanobubble and nanodroplet segmentation in atomic force microscope images using the spherical Hough transform,
Beilstein journal of nanotechnology, 8, 2572-2582 (2017)

- Binglin Zeng, Kai Leong Chong, Yuliang Wang, Christian Diddens, **Xiaolai Li**, Marvin Detert, Harold J. W. Zandvliet, Detlef Lohse,
Periodic bouncing of a plasmonic bubble in a binary liquid by competing solutal and thermal Marangoni forces,
Proc. Natl. Acad. Sci. U.S.A., 118, e2103215118 (2021)

- Yuliang Wang, Zhaoxin Lian, Xiaomeng Cui, Buyun Chen, **Xiaolai Li**, Mao Li, Binglin Zeng, Shusheng Bi,
Visual sensing based ultrahigh precision motion control with compensated mechanical drift across different stages,
IEEE/ASME Transactions on Mechatronics, 25, 1422-1431 (2020)